NTNU – Trondheim
Norwegian University of
Science and Technology

Finite element implementation of lower-order strain gradient plasticity in Abaqus

Teodor Lunaas Heggelund

Master of Science in Engineering and ICT
Submission date: June 2015
Supervisor: Odd Sture Hopperstad, KT
Co-supervisor: David Morin, KT

Norwegian University of Science and Technology
Department of Structural Engineering

Department of Structural Engineering
FACULTY OF ENGINEERING SCIENCE AND TECHNOLOGY
NTNU – Norwegian University of Science and Technology

MASTER'S THESIS 2015

for

Teodor Lunaas Heggelund

Finite element implementation of lower-order strain gradient plasticity in Abaqus

1. INTRODUCTION

Centre for Advanced Structural Analysis (CASA) is the new Centre for Research-based Innovation hosted by SIMLab/ Department of Structural Engineering at NTNU. The research within CASA is aimed at creating a platform for credible numerical simulations of structures for innovation and value creation in industry through multi-scale testing, modelling and simulation. Thus, the coupling of physical phenomena at the micro-scale (e.g., grain or particle size) and the macro-scale (specimen or component size) is an important part of the research in CASA and the background for this research project. It has been observed in several experiments that the plastic behaviour of materials may exhibit size dependence: the smaller the size, the stronger the resistance of the material. There are several examples: the indentation hardness of a metal typically increases as the indenter size decreases; the particle strengthening of alloys is stronger for small particles than for large when the volume fraction of hard particles remains the same; a metal gets stronger as the grain size is reduced. The size effect becomes significant as the indenter size, particle spacing or grain size is below about 10 μm. To describe this size effect, it is necessary to include a length scale into the elastic-plastic material models. Based on physical considerations, this is achieved by making the flow stress dependent of the plastic strain gradient; i.e., the higher the plastic strain gradients the higher the strength. The plasticity theory thus obtained is denoted strain gradient plasticity.

2. OBJECTIVES

The research project has three main objectives: (1) to implement selected strain gradient plasticity models in the nonlinear finite element code ABAQUS; (2) to verify and validate the implementation against analytical results from the literature; (3) to apply the strain gradient plasticity models in simulations of various problems such as particle strengthening and void growth.

3. A SHORT DESCRIPTION OF THE RESEARCH PROJECT

The main topics in the research project will be as follows;

1. Literature review on the experimental background for strain gradient plasticity, the physical mechanisms responsible for gradient effects and the various mathematical formulations of strain gradient plasticity.
2. Solution of analytical problems using strain gradient plasticity.
3. Implementation of lower-order strain gradient plasticity in ABAQUS.
4. Verification and validation of the strain gradient plasticity implementation using the analytical solutions from 2).
5. Numerical study of selected problems (particle strengthening and void growth) where gradient effects are assumed of importance.

Supervisors: Odd Sture Hopperstad, David Morin (NTNU)

The thesis must be written according to current requirements and submitted to Department of Structural Engineering, NTNU, no later than June 10th, 2015.

NTNU, January 14th, 2015

Odd Sture Hopperstad
Professor

Department of Structural Engineering
Faculty of Engineering Science and Technology
NTNU- Norwegian University of Science and Technology

ACCESSIBILITY

OPEN

MASTER THESIS 2015

SUBJECT AREA:	DATE:	NO. OF PAGES: 152
Computational mechanics	June 10	26 + 94 + 32

TITLE:

Finite element implementation of lower-order strain gradient plasticity in Abaqus

BY:

Teodor Lunaas Heggelund

SUMMARY:

A finite element method implementation of lower-order strain gradient plasticity is developed. Its validity is checked against known analytical solutions. The implementation gives expected trends when applied to particle strengthening and void growth.

During implementation, stability issues are encountered. The instability is denoted the tower/canyon defect, and traced back to nodal averaging as a basis for strain gradient computation. A conservative stability criterion for stability is developed, and within the stability limit given by the criterion, no tested models are unstable. Instabilities are shown to appear under a combination of (a) large plastic strains, (b) small length scale and (c) fine element mesh. Nodal averaging underestimates the strain gradient at boundaries.

An alternative to nodal averaging is developed, denoted \emph{nodal contributions}. Nodal contributions has not been implemented for use in finite element simulations, but analytical verification indicates that nodal contributions is resilient to previously encountered stability issues. Nodal contributions is shown to represent strain gradients exactly for linear strain fields, even at boundaries.

The exact, mathematical solution to the applied lower-order strain gradient plasticity theory is shown to be singular given a prescribed stress field. Iterative solutions based on load incrementation choose one of the possible resulting strain distributions. Nodal averaging is biased towards small strain gradients at boundaries.

RESPONSIBLE TEACHER:	Professor Odd Sture Hopperstad.
SUPERVISOR(S):	Professor Odd Sture Hopperstad and Researcher David Morin.
CARRIED OUT AT:	SIMLab, The Department of Structural Engineering, NTNU.

Institutt for konstruksjonsteknikk
Fakultet for ingeniørvitenskap og teknologi
NTNU- Norges teknisk- naturvitenskapelige universitet

TILGJENGELIGHET

ÅPEN

MASTEROPPGAVE 2015

FAGOMRÅDE:	DATO:	ANTALL SIDER: 152
Beregningsmekanikk	10. juni	26 + 94 + 32

TITTEL:

Elementmetodeimplementasjon av lavere ordens tøyningsgradientplastisitet i Abaqus

UTFØRT AV:

Teodor Lunaas Heggelund

SAMMENDRAG:

En elementmetodeimplementasjon av lavere ordens tøyningsgradientplastisitet har blitt utviklet. Validitet er sjekket mot kjente analytiske løsninger på enkle problemer. Implementasjonen gir forventede resultater når anvendt på partikkelforsterkning og sporevekst.

Under implementasjonen ble stabilitetsproblematikk avdekket. Instabiliteten, kalt tårn/juv-defekten, ble sporet tilbake til nodeglatting av det plastiske tøyningsfeltet for utregning av gradienten av plastiske tøyninger. Et konservativt stabilitetskriterium har blitt utviklet, og ingen ustabile resultater er blitt observert så lenge stabilitetskriteriet er overholdt. Instabiliteter er vist til å forekomme under en kombinasjon av (a) store plastiske tøyninger, (b) liten lengdeskala og (c) fint elementnett. Nodeglatting underestimerer tøyningsgradienten i grensesjikt.

Et alternativ til nodeglatting er blitt utviklet, kalt nodebidrag. Nodebidrag har ikke blitt implementert til bruk i elementmetode, men analytisk verifikasjon tilsier at at nodebidrag ikke er utsatt for instabiliteter. Nodebidrag er vist å gjengi tøyningsgradienten eksakt for lineære tøyningsfelt, inkludert i grensesjikt.

Den eksakte, matematiske løsningen til den anvendte lavere ordens tøyningsgradentplastisitetsteorien er vist å være singulær gitt spenningsfelt. Iterative løsninger basert på spenningsinkrementer velger ett av gyldige tøyningsfelt. Nodeglatting tenderer mot løsninger med små tøyningsgradienter i grensesjikt.

FAGLÆRER:	Professor Odd Sture Hopperstad.
VEILEDER(E):	Professor Odd Sture Hopperstad og Forsker David Morin.
UTFØRT VED:	SIMLab, Institutt for konstruksjonsteknikk, NTNU.

Til Zeppelin.

Abstract

A finite element method implementation of lower-order strain gradient plasticity is developed. Its validity is checked against known analytical solutions. The implementation gives expected trends when applied to particle strengthening and void growth.

During implementation, stability issues are encountered. The instability is denoted the tower/canyon defect, and traced back to nodal averaging as a basis for strain gradient computation. A conservative stability criterion for stability is developed, and within the stability limit given by the criterion, no tested models are unstable. Instabilities are shown to appear under a combination of (a) large plastic strains, (b) small length scale and (c) fine element mesh. Nodal averaging underestimates the strain gradient at boundaries.

An alternative to nodal averaging is developed, denoted *nodal contributions*. Nodal contributions has not been implemented for use in finite element simulations, but analytical verification indicates that nodal contributions is resilient to previously encountered stability issues. Nodal contributions is shown to represent strain gradients exactly for linear strain fields, even at boundaries.

The exact, mathematical solution to the applied lower-order strain gradient plasticity theory is shown to be singular given a prescribed stress field. Iterative solutions based on load incrementation choose one of the possible resulting strain distributions. Nodal averaging is biased towards small strain gradients at boundaries.

Acknowledgements

First, I would like to thank my supervisors Odd Sture Hopperstad and David Morin. Odd Sture, with his academic interest and excitement in the field of strain gradient theory, has been instrumental in the choice of task. His structure has been a good counter balance to my natural tendency to dash around in every direction, and has helped focus on actually relevant questions. David Morin is the architect behind the finite element strain gradient plasticity implementation. When finite element analyses have given the most incomprehensible error messages, he has lead the way.

Additional thanks go to Ole Vestum and Frans Erstad, who have both given feedback on the more abstract parts of this thesis; Kjell Magne Mathisen and Kolbein Bell, who as instructors in finite element courses laid the groundwork of my understanding of the finite element method in structural analysis; and Torodd Berstad for his expertise in Linux administration.

Contents

List of Figures

List of Tables

Preface

This thesis is based on a well defined task description with well defined tasks. These define the narrative of the thesis. Through work with these tasks, however, other topics arose, starting out with the stability limitation. The stability limitation was found fairly early in the verification of the finite element implementation, and has thus been integrated well into the thesis. It fits the narrative.

During the final weeks of work, foundation for the content of the appendices was found. These findings bear resemblance to non-directional research, and fit badly within the narrative of this thesis, where claims are backed by data from numerical analysis. This is why they are organized into appendices, and not as main parts of this master's thesis. It is *not* because I believe they are less important—but because their foundations are analytical arguments, and not finite element simulations.

On a personal note, ideas have been conceived on the weirdest of places. In the shower (nodal contribtions), during failed attempts to sleep (the tower/canyon defect) and after a day's distance from the material (ambiguity of lower-order theories) are examples. As Nassim Taleb repeatedly recommends in "Antifragile"; long, slow walks are good for the brain.

Finally—this material is at times rather abstract. Please take your time. I have.

Teodor Lunaas Heggelund
June 10, 2015

Chapter 1

Introduction

1.1 Background and motivation

Conventional continuum theories of plasticity have no intrinsic length scale. The material behaviour depends on geometric shape, but hardening is independent of size. This coincides well with experiments for significant length scales down to approximately 100 µm. At 10 µm there is clear evidence that the material hardens as the length scale decreases, for cases of non-constant plastic strain distribution, such as bending of thin beams [21] and torsion of thin wires [9]. To explain these effects, micro-scale models of plasticity are examined.

The source of conventional isotropic hardening in plasticity is random imperfections. The crystal lattice of the material contains defects, and when the material is strained, the defects move. When they randomly (statistically) block each other, they give rise to material hardening. These dislocations are denoted **statistically stored dislocations**.

Another source of dislocation of the crystal lattice is special strain conditions that *require* dislocations. An example is plastic bending of a beam, where new crystal planes must be "inserted" into the lattice on the side in tension, and "removed" on the side in compression. These dislocations are denoted **geometrically necessary dislocations**, and appear when there is a change of plastic strain; a non-zero plastic strain gradient.

When accounting for these effects, two possible approaches have been discussed extensively in literature. The first was used by Fleck et al. in 1994 [9]. They create an augmented equivalent plastic strain measure depending on both

regular equivalent strain and equivalent plastic strain gradient. The equivalent plastic strain gradient is expressed from the curvature tensor, which depends linearly on the plastic strain gradient. An augmented strain tensor is defined consisting both of strains and strain derivatives. The augmented stress tensor is work-conjugate to the augmented strain tensor, and must contain higher order stresses work conjugate to the stain derivatives. Equilibrium equations are obtained requiring the virtual work from augmented strain and augmented stresses to be zero. The resulting higher-order strain gradient theory requires additional boundary conditions, and in a finite element implementation, additional degrees of freedom. This may be achieved by implementation of a user element [16]. Theories based on augmented stresses and strains requiring higher order stresses and boundary conditions are denoted **higher-order theories**.

An alternative approach is to instead augment the hardening function, so that the hardening depends on the plastic strain and the plastic strain gradient. The alternative approach does not modify equilibrium equations. Plastic strain gradient hardening may taken into account by modification of the flow stress. The modified flow stress depends on both the plastic strain and the plastic strain gradient. Theories that only modify the material hardening and do not introduce higher-order boundary conditions or higher-order strains are denoted **lower-order theories**. Lower order theories may be derived from higher-order theories aiming to give the same incremental moduli as higher order theories [2] or through direct consideration of dislocations as a source for material hardening [13].

1.2 Objectives and scope

First, the correctness of the current lower-order strain gradient plasticity model must be verified. This is done by comparing response predicted by the finite element implementation to known analytical solutions. The finite element strain gradient plasticity implementation uses a different measure of the equivalent plastic strain gradient η^p, defined in Section 3.2, than has been used in previous literature, and whether the current measure is sufficient must be investigated. Predicted response for two cases will then be discussed, first particle strengthening, then void growth. Both produce non-uniform equivalent plastic strain fields $\varepsilon^p(x, y)$, and accounting for strain gradient effects is expected to add hardening.

Chosen theories are not sensitive to load rate, hence there is no time dependence, and analyses are static or quasi-static. Hence, viscoplastic effects are outside the scope of this thesis. Analytical solutions are produced with small

deformation theory. The finite element implementation, however, is valid for large deformations, case studies are done without small deformation and small strain limitations.

1.3 Terminology

Mathematical modelling of strain gradient plasticity is done using higher- or lower-order theories. Each model gives a precise mathematical formulation, similar to that there is only *one* solution to a meshed, linear finite element problem with sufficient boundary conditions. This thesis examines three overall procedures to solving the problem lower-order formulations. First, **analytical solutions** are examined. This is meant as calculating the stress or strain field form the formulation. Discretization is then done over time and space. Spatial discretization allows for numerical computation of the plastic strain gradient, and loading or displacement is incremented over time. Then, **finite element solutions** are presented. These are found by extending Abaqus with a user subroutine for material behaviour sensitive to strain gradient hardening. Finally, an exact **mathematical solution** is presented in Appendix C. This solution does not discretize, neither in space nor in time. A continuous plastic strain field that satisfies the lower-order strain gradient plasticity model is found directly through the solving of a differential equation. No time steps are needed.

Chapter 2

Theory

This chapter will introduce the theoretical background for strain gradient plasticity. For a thorough explanation, see textbooks by François et al. [10], on material behaviour, specifically chapter 3 on plasticity; and by Hull and Bacon [14], on dislocation theory. The latter is recommended for excellent use of figures; dislocations are inherently three dimensional, and good three-dimensional figures are essential for a spatial understanding.

2.1 Motivation for plasticity theory

The early 20th century saw advances in the theoretical explanation to plasticity. In 1926 the Russian physicist Yakov Frenkel (Яков Френкель) calculated the theoretical critical shear stress τ_c based on material crystal structure. Assume that the structure is perfect, and two layers of atoms lie on top of each, illus-

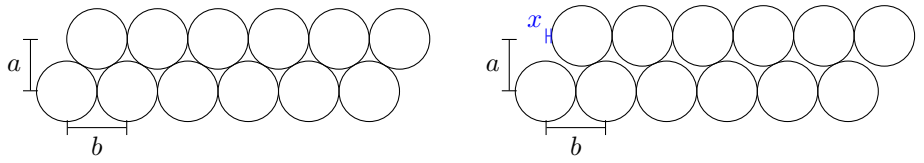

Figure 2.1: Shear on a slip plane where the atoms are perfectly aligned. Slip begins on the figure to the right. x is the movement of the top plane with respect to the lower, coloured blue.

trated left in Figure 2.1. To the right in Figure 2.1, the top atom layer is sheared with respect to the bottom atom layer. Assume the energy per volume E to be periodic over length x. When the energy is periodic, so must the shear stress $\tau = \frac{\mathrm{d}E}{\mathrm{d}\gamma}$. The energy is minimal in the default configuration, maximum when $x = b/2$, and again minimal at $x = b$, where x is the movement of the top plane with respect to the lower, and b is defined in Figure 2.1. This gives a periodic function for the shear stress as

$$\tau(x) = \tau_c \sin\left(\frac{2\pi}{b}x\right), \tag{2.1}$$

where τ_c is a constant. Its maximum value is τ_c, and its derivative in the origin is $\frac{\mathrm{d}\tau}{\mathrm{d}x} = \tau_c \frac{2\pi}{b}$. Another way to measure the initial stress is using linear elasticity, so that $\tau = \mu\gamma$, where μ is the shear modulus and shear strain is $\gamma = \tan\frac{x}{a} \approx x/a$ for small deformations.

Equating the two expressions for the derivative of the shear stress in the origin[1], we have $\frac{2\pi}{b}\tau_c = \frac{\mu}{a}$, which solved for the critical shear stress gives

$$\tau_c = \frac{\mu b}{2\pi a}. \tag{2.2}$$

This gives the order of the critical shear stress as $\tau_c \approx \mu/10$, which is far from measured data. Compare this to S355 steel, where the shear modulus is $\mu = 80\,000\,\mathrm{MPa}$ and the yield shear stress is $\tau_y = 205\,\mathrm{MPa} \approx \mu/400$. This discrepancy between theory and data led Sir Geoffrey Ingram Taylor to question the assumed perfect crystalline shape, and in the 1930s develop plasticity theory based on dislocation theory—which did not assume perfectly shaped crystals.

2.2 Dislocation theory

What differentiates elastic and plastic strains at a fundamental level is change of the crystal structure. Whereas elastic deformations leave the crystal lattice structure unchanged after unloading, plastic deformations changes this structure permanently. When a beam is bent plastically so that its top is in tension, additional half-planes of atoms are inserted into the crystal lattice of the top part of the beam. This change in the crystal structure is a dislocation.

[1] This approach is inaccurate, but its inaccuracy negligible is compared to the (order of) error that appears between theory and experimental data.

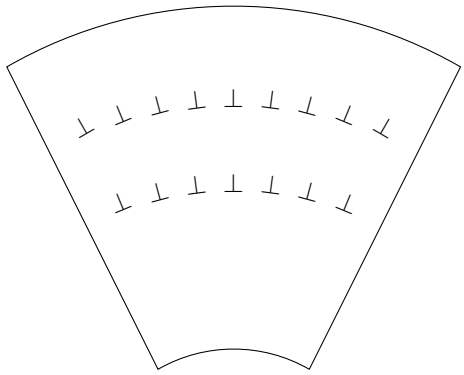

Figure 2.2: Beam in bending. Dislocations are illustrated as $\perp$. The dislocation symbol $\perp$ can be understood as the end of a crystal plane. For each $\perp$ pictured, there is a half-plane of atoms that *ends* in the vertical line. Therefore, in the pictured beam, new planes are introduced from the top.

Dislocations are categorized into *geometrically necessary dislocations* (GNDs) and *statistically stored dislocations* (SSDs). Geometrically necessary dislocations arise from kinematics that *require* dislocations for continuity. The beam in Figure 2.2 is an example. Statistically stored dislocations are distributed randomly through the material.

Taylor's work on dislocations as an explanation for material plasticity is based on the mathematical foundation laid by the Italian mathematician and physicist Vito Volterra in 1905. Volterra's definition of dislocations follows.

Imagine first the beam before bending, illustrated in Figure 2.3. We examine

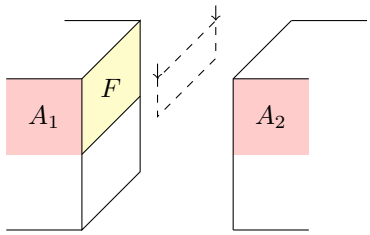

Figure 2.3: Beam before bending. F is the yellow area. A is the red area $A = A_1 \cup A_2$. The dashed line is the new atom layer.

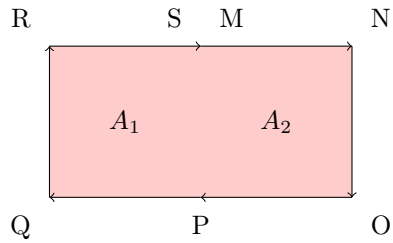

Figure 2.4: Area A before bending.

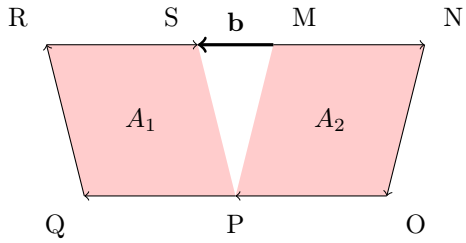

Figure 2.5: Area A after bending.

a cut in the beam. On the cut, we define an area A. When the beam is bent plastically, a new layer of atoms will be inserted on F, separating previously touching areas A_1 and A_2. Figure 2.4 shows the closed loop $l = MNOPQRS$ before bending. Each of the nodes in the loop is an atom in the crystal lattice, and M is connected to S.

After bending, the loop is no longer closed, as shown in Figure 2.5. The Burgers vector $\mathbf{b}$ of length b is defined as the displacement needed to reconnect the now disconnected nodes S and M. Note that the direction of $\mathbf{b}$ depends on order of the nodes in l, as the Burgers vector reconnects the *first* node to the *last*. Positive l *into* the plane, as shown on Figure 2.4; $MNOPQRS$ (right hand rule) gives $\mathbf{b}$ pointing left, reconnecting M to S. Choosing positive l *out of* the plane, not illustrated; $SRQPONM$ gives $\mathbf{b}$ pointing right, reconnecting S to M.

In this example of a beam in bending, the dislocations give a Burgers vector parallel to the curve $\mathbf{b}||l$. This is the case for *edge dislocations*. For a wire exposed to plastic twist, the Burgers vector would be perpendicular to the curve $\mathbf{b}\perp l$; twist induces *screw dislocations*. Twist gives rise to shear strains, and slip

will occur parallel to the wire axis. To "catch" the twist dislocation of the wire, A is chosen as the cross section area, and the slip is normal to the area and its bounding curve l. An example of screw dislocations arising from twisting of a wire is given in the textbook by François et al. [10]. Generally, edge and screw dislocations can occur at the same time.

The distribution of dislocations over a volume is described by the dislocation density ρ_D, which is the total length of dislocations over a volume, divided by the volume V

$$\rho_D = \frac{NL}{V}, \tag{2.3}$$

where N^2 is the number of dislocations and L the average dislocation length. For the two-dimensional case, if a circuit can be chosen so that the dislocation density inside the circuit is equal to the total dislocation density, the dislocation density is

$$\rho_D = \frac{N}{A}, \tag{2.4}$$

where A is the area of the circuit. The dislocation density ρ_D is of unit $\frac{\mathrm{m}}{\mathrm{m}^3} = \frac{1}{\mathrm{m}^2}$.

The dislocation density of the beam in Figure 2.6 is used as an example. An infinitesimal angle is chosen so that the geometry is linear, $\theta \approx 0$. $ABCD$ is chosen as a Brugers circuit, giving the magnitude of the Brugers vector $b = D'D/N$, when there are N dislocations. The area of the circuit is $AB \times BC$ for small deformations. Inserting into Equation 2.4 gives

$$\rho_D = \frac{D'D}{bAB \times BC}. \tag{2.5}$$

Using that $AD = BC = R\theta$ and $AD' = (R + AB)\theta$, the dislocation density simplifies to

$$\rho_D = \frac{(R + AB)\theta - R\theta}{bAB \times R\theta} = \frac{1}{bR}. \tag{2.6}$$

To sum up, the dislocation density increases when the average dislocation size is small, because there must be more dislocations to account for the same deformation. The dislocation density is also proportional to the curvature $\kappa = \frac{1}{R}$, as larger curvatures require more dislocations.

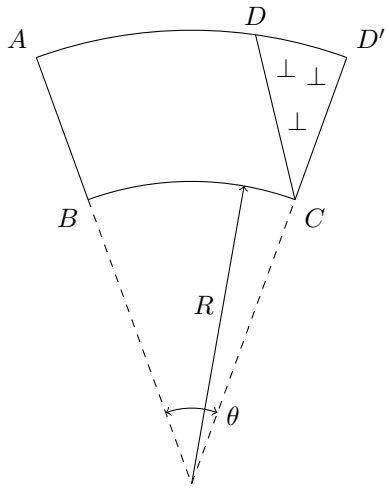

Figure 2.6: Beam in bending gives dislocations. Because of symmetry, only the top part of the beam is considered. The bottom part of the beam has not been drawn here.

2.3 Dislocations in crystals

Aluminium alloys form *face centered cubic* (FCC) crystal structures, illustrated in Figure 2.7. In addition to atoms on the corner nodes, FCC crystals have atoms on the centre of each face, giving the figure in in total 16 atoms. These atoms are shared between two or more crystals, giving each crystal 4 atoms. This can be visualized as the number of nodes added to an element mesh when each new element is added.

A dislocation has been defined as the slip of a lattice plane. The direction of the slip depends on the crystal structure. When two atoms are far apart, the forces between them are low. This causes slips to happen so that the distance between two slip planes is as long as possible. Equivalently, the distance between atoms *in* the slip plane is minimized.

Possible slip planes depend on the crystal structure. Planes are characterized by their normal, and described using Miller indices. Miller indices can in general describe crystal structures irregular in size, so that a crystal has different sizes

[2] N will later be used as an exponent in the material power law. N is used to denote number of dislocations in this chapter *only*.

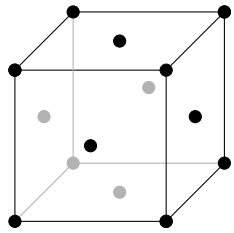

Figure 2.7: Crystal structure for a face-centered cubic crystal. The dots are atoms. Atoms in FCC structure are placed on corners and on the centre of faces.

in x, y and z-directions, even crystal structures with more than three unit axes. This thesis will give a brief introduction to the case where the sides of the crystal are of equal length, and the x, y and z-axes are axes of symmetry.

Miller indices for the yellow plane in Figure 2.8 are calculated as follows.

1. Let the plane of symmetry cross the unit axes in A, B and C
2. Arrange the inverted lengths of the distances along the unit axes as $\left(\frac{a}{OA}, \frac{a}{OB}, \frac{a}{OC}\right) = \left(\frac{a}{2a}, \frac{a}{3a}, \frac{a}{3a}\right)$
3. Multiply with least common multiple, and remove commas to get (322)

Bar above numbers denotes negation: $\left(\frac{a}{-2a}, \frac{a}{3a}, \frac{a}{3a}\right) = (\bar{3}22)$. Using curly braces allows negation to be interchanged, such that $(322), (\bar{3}22), (3\bar{2}2), ... \in \{322\}$.

In FCC crystal structures, $\{111\}$-planes are close packed, and slip is likely to happen along these planes.

2.4 The Taylor dislocation model

As the plastic strain increases, so does the dislocation density, which increases the amount of "obstacles" in the crystal lattice. The textbook *Mechanical Behavior of Materials* [10] describes how this gives an expression for the critical shear stress required for slip as

$$\tau_c = \alpha \mu b \sqrt{\rho_D}, \tag{2.7}$$

where $\alpha \in (1/3, 1/4)$ depending on the crystal structure, μ is the shear modulus and b is the length of the Brugers vector. This procedure is based on Taylor's work in the 1930s.

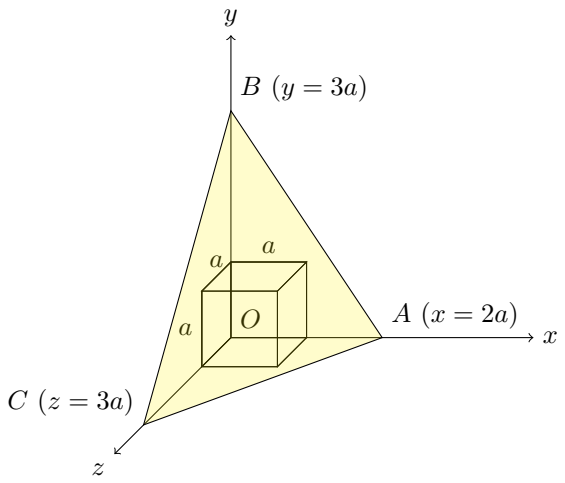

Figure 2.8: Miller indices example.

For small dislocation densities, a good approximation of the the total dislocation density is the sum of statistically stored dislocation and geometrically necessary dislocation densities

$$\rho_D = \rho_{SSD} + \rho_{GND}. \tag{2.8}$$

For calculating the density of geometrically necessary dislocations ρ_{GND}, a more general measure is needed. This density is related to the *spatial change* of plastic strain; the plastic strain gradient. Plastic strain is a 2nd tensor ε^p_{ij}, making its gradient a 3rd order tensor $\varepsilon^p_{ij,k} = \frac{\partial \varepsilon^p_{ij}}{\partial x_k}$. Nye [19] and Ashby [1] related the density of the geometrically necessary dislocations to the *effective* plastic strain gradient η^p

$$\rho_{GND} = \bar{r}\frac{\eta^p}{b}, \tag{2.9}$$

where $\bar{r} \approx 1.9$ for face centred cubic crystals.

Let us compare this to the dislocation density calculated for the beam in Figure 2.6. Neglecting elastic strains, the non-zero component of the plastic strain gradient tensor is $\frac{\mathrm{d}\varepsilon^p_x}{\mathrm{d}y} = \kappa = \frac{1}{R}$. Taking the effective plastic strain gradient η^p as the l^2 norm of the plastic strain gradient tensor, the dislocation density is $\rho_{GND} = \bar{r}\frac{\eta^p}{b} = \bar{r}\frac{1}{bR}$, which differs by a factor of $\bar{r}$. The previous manual calculation did not take crystal structure and lattice orientation into account, and

using the l^2 norm of the plastic strain gradient tensor is an arbitrary measure of the strain gradient. It is concluded that Nye and Ashby's measure is in the correct order of magnitude.

The critical shear stress on a slip is related to the flow stress as

$$\sigma_{flow} = M\tau_c, \tag{2.10}$$

where $M \approx 3.06$ for isotropic FCC crystals [4, 15]. The flow stress is the (hardened) yield limit of the material, and yielding occurs when the equivalent von Mises stress exceeds the flow stress $\sigma_e = \sqrt{\frac{3}{2}\sigma'_{ij}\sigma'_{ij}} > \sigma_{flow}$.

With the foundation in place, insert for $\rho_D = \rho_{SSD} + \rho_{GND}$ into equations 2.10 and 2.7 to get

$$\sigma_{flow} = M\alpha\mu b\sqrt{\rho_{SSD} + \bar{r}\frac{\eta^p}{b}}, \tag{2.11}$$

a hardening function taking into account plastic strain ε^p and plastic strain gradient η^p, used by Huang et al. [13]. The density of statistically stored dislocation can be found from tensile tests without strain gradient. This thesis will adopt a power law, so that the hardened flow stress without strain gradient effects is $\sigma_{flow} = \sigma_y f(\varepsilon^p)$, where σ_y is the yield stress before hardening, and $f(\varepsilon^p)$ an isotropic hardening power-law, function of the equivalent plastic strain $\varepsilon^p = \int_0^t \dot{\varepsilon}^p \,\mathrm{d}t$, where $\dot{\varepsilon}^p = \sqrt{\frac{2}{3}\dot{\varepsilon}^p_{ij}\dot{\varepsilon}^p_{ij}}$. This way, we can determine the density of statistically stored dislocations as $\rho_{SSD} = (\sigma_y f(\varepsilon^p)/M\alpha b)^2$, and the flow stress becomes

$$\begin{aligned}\sigma_{flow} &= M\alpha\mu b\sqrt{\left(\frac{\sigma_y f(\varepsilon^p)}{M\alpha\mu b}\right)^2 + \bar{r}\frac{\eta^p}{b}} \\ &= \sigma_y\sqrt{f(\varepsilon^p)^2 + l\eta^p} \quad \text{where} \quad l = \left(\frac{M\alpha\mu}{\sigma_y}\right)^2 \bar{r}b.\end{aligned} \tag{2.12}$$

l is of unit length and can be found directly from experiments, as done by Stölken and Evans [21]. The length scale is of the order of $1 \times 10^{-6}\,\mathrm{m} = 1\,\mu\mathrm{m}$, and strain gradient effects are notable when there is notable change in plastic strain within this length scale.

Chapter 3

Material model and parameters

This chapter explains the material model used in this thesis. Two alternative formulations are presented. Traditional J_2 plasticity modified to take strain gradient effects into account, described in Section 3.1 is used for the finite element implementation. For the analytical solutions, an alternative approach without a yield surface is used. This approach is described in Section 3.3. Both formulations take strain gradient effects into account. Measures of the effective strain gradient η^p are given in Section 3.2. Material parameters are listed in Section 3.4.

3.1 J_2 yield surface plasticity

The material model implemented in the finite element method is based on standard J_2 plasticity as described in this section. Associated flow rule is adopted. Strain rates are divided into elastic and plastic $\dot{\varepsilon}_{ij} = \dot{\varepsilon}^e_{ij} + \dot{\varepsilon}^p_{ij}$. Elastic and plastic strain rates are expressed from stress rates and equivalent plastic strain

rate as

$$\begin{aligned} \dot{\varepsilon}^e_{ij} &= \underbrace{\frac{1}{2\mu}\dot{\sigma}'_{ij}}_{\text{deviatoric}} + \underbrace{\frac{\dot{\sigma}_{kk}}{9K}\delta_{ij}}_{\text{hydrostatic}} \\ \dot{\varepsilon}^p_{ij} &= \frac{\partial F}{\partial \sigma_{ij}}\dot{\varepsilon}^p = \underbrace{\frac{3\dot{\varepsilon}^p}{2\sigma_e}\sigma'_{ij}}_{\text{plastic}}. \end{aligned} \tag{3.1}$$

ε^e_{ij} is the elastic strain tensor, ε^p_{ij} is the plastic strain tensor, $\dot{\varepsilon}^p = \sqrt{\frac{2}{3}\dot{\varepsilon}^p_{ij}\dot{\varepsilon}^p_{ij}}$ is the effective plastic strain rate, μ the shear modulus and K the bulk modulus. $\sigma'_{ij} = \sigma_{ij} - \frac{1}{3}\sigma_{kk}$ is the deviatoric stress tensor, and the equivalent stress is the von Mises stress given by the deviatoric stress tensor $\sigma_e = \sqrt{\frac{3}{2}\sigma'_{ij}\sigma'_{ij}}$. The Kronecker delta δ_{ij} is

$$\delta_{ij} = \begin{cases} 1 & \text{if } i = j \\ 0 & \text{if } i \neq j \end{cases}. \tag{3.2}$$

The yield function F is given by the equivalent stress and the flow stress

$$F(\sigma_e) = \sigma_e - \sigma_{flow}, \tag{3.3}$$

and is restricted by the Kuhn-Tucker conditions

$$F \leq 0, \quad \dot{\varepsilon}^p \geq 0 \quad \text{and} \quad \dot{\varepsilon}^p F = 0. \tag{3.4}$$

The Kuhn-Tucker conditions imply that there can only be yield ($\dot{\varepsilon}^p > 0$) *on* the yield surface when the yield function is zero $F = 0$. The yield function F gives its partial derivative with respect to strains in Equation 3.1. The flow stress is the hardened yield stress with contributions from the equivalent plastic strain ε^p and the effective plastic strain gradient η^p

$$\sigma_{flow} = \sigma_y\sqrt{f(\varepsilon^p)^2 + l\eta^p} \quad \text{where} \quad f(\varepsilon^p) = \left(1 + \frac{E\varepsilon^p}{\sigma_y}\right)^N. \tag{3.5}$$

Note that F is the yield function, and f is a non-dimensional isotropic power law-based hardening function. E is Young's modulus, which can be expressed from μ and K, and N[1] a non-dimensional material parameter $0 \leq N < 1$. The

[1] N is now used as an exponent in the material power law. This is the case for the rest of the thesis.

effective plastic strain gradient η^p is defined in Section 3.2, and the characteristic material length scale l was defined in Equation 2.12. l is later taken as a material parameter.

3.2 Effective plastic strain gradient

Huang et al. examine two different definitions of the effective plastic strain gradient η^p. This thesis introduces one more. The partial derivatives of the plastic strain tensor are denoted using comma notation as

$$\varepsilon^p_{ij,k} = \frac{\partial \varepsilon^p_{ij}}{\partial x_k}.$$

Huang et al.'s first measure [13] is from work by Fleck and Hutchinson [8], which was determined using three models of geometrically necessary dislocations, and is defined as

$$\eta^{p,A} = \sqrt{\frac{1}{4}\eta^{p,A}_{ijk}\eta^{p,A}_{ijk}} \quad \text{where} \quad \eta^{p,A}_{ijk} = \varepsilon^p_{ki,j} + \varepsilon^p_{jk,i} - \varepsilon^p_{ij,k}. \tag{3.6}$$

Huang et al.'s second measure of the effective strain gradient is based on a tensor of geometrically necessary dislocations expressed from the plastic deformation gradient tensor, based on work by Steinmann [20] and Cermelli and Gurtin [5]. The total deformation gradient can be decomposed into elastic and plastic parts $\mathbf{F} = \mathbf{F}^e \cdot \mathbf{F}^p$. The tensor of geometrically necessary dislocations becomes $\frac{1}{\det \mathbf{F}^p}\mathbf{F}^p \cdot (\nabla \times \mathbf{F}^p)$, which reduces to $-\boldsymbol{\varepsilon}^p \times \nabla$ for infinitesimal deformations, where $\boldsymbol{\varepsilon}^p$ is the plastic strain tensor. Note the difference between the (boldface) plastic strain tensor $\boldsymbol{\varepsilon}^p$ and the effective plastic strain (scalar) ε^p. The l^2-norm of the tensor of geometrically necessary dislocations then becomes

$$\eta^{p,B} = \sqrt{(\boldsymbol{\varepsilon}^p \times \nabla) : (\boldsymbol{\varepsilon}^p \times \nabla)} = \|\boldsymbol{\varepsilon}^p \times \nabla\|. \tag{3.7}$$

In addition, this thesis examines the norm of the gradient of the *equivalent* plastic strain

$$\eta^{p,C} = \sqrt{\frac{\partial \varepsilon^p}{\partial x_i}\frac{\partial \varepsilon^p}{\partial x_i}} = \|\nabla \varepsilon^p\|. \tag{3.8}$$

The new measure of the effective plastic strain gradient $\eta^{p,C}$ has the advantage of depending only on the equivalent plastic strain ε^p, and not on the plastic strain tensor components ε^p_{ij}. This makes finite element implementation straightforward. The new measure $\eta^{p,C}$ is path dependent, in contrast to measures from

literature $\eta^{p,A}$ and $\eta^{p,B}$. $\eta^{p,C}$ is path dependent because it is derived from the equivalent plastic strain $\varepsilon^p = \int_t \dot{\varepsilon}^p \, \mathrm{d}t$ instead of the path-independent plastic strain tensor ε^p_{ij}, as is the case for $\eta^{p,A}$ and $\eta^{p,B}$. A discussion of whether the plastic strain gradient measure should be path independent can be based on dislocation theory, and is outside of the scope of this thesis.

A, B and C have been introduced to differentiate between the different measures of the effective plastic strain gradient, and thereby prevent confusion in equations of which measure of the effective plastic strain gradient η^p is being used.

3.3 An alternative viscoplastic-like formulation

Huang et al. [13] introduced alternative viscoplastic-like formulation to the J_2 yield surface theory in Section 3.1. This alternative formulation does not have a yield surface, and does therefore not need loading/unloading conditions, resulting in simpler analytical solutions.

Equation 3.3 defining the yield surface and Equation 3.4 giving the Kuhn-Tucker conditions are replaced with the alternative plastic flow formulation

$$\dot{\varepsilon}^p = \dot{\varepsilon} \left(\frac{\sigma_e}{\sigma_{flow}} \right)^m . \tag{3.9}$$

The equivalent plastic strain rate is given from the equivalent deviatoric strain rate $\dot{\varepsilon} = \sqrt{\frac{2}{3} \dot{\varepsilon}'_{ij} \dot{\varepsilon}'_{ij}}$, where $\varepsilon'_{ij} = \varepsilon_{ij} - \frac{1}{3}\varepsilon_{kk}$. The flow stress gives the limit between elastic-dominated strains ($\sigma_e < \sigma_{flow}$) and plastic-dominated strains ($\sigma_e > \sigma_{flow}$). m is a high non-dimensional exponent. In the limit of $m \to \infty$, Equation 3.9 is indistinguishable from the yield surface formulation. Lower exponents give good correspondence without numerical instability. The difference in material response when increasing the exponent $m > 20$ is small. This thesis uses $m = 20$ or $m \to \infty$, implying $\sigma_e = \sigma_{flow}$ for analytical solutions.

It is worth noting that if we divide the equivalent deviatoric strain rate into an elastic and a plastic part $\dot{\varepsilon} = \dot{\varepsilon}^e + \dot{\varepsilon}^p$, the plastic strain rate is

$$\dot{\varepsilon}^p = \frac{\left(\frac{\sigma_e}{\sigma_{flow}} \right)^m}{1 - \left(\frac{\sigma_e}{\sigma_{flow}} \right)^m} \dot{\varepsilon}^e . \tag{3.10}$$

An interesting limit of this equation is $\lim_{\sigma_e \to \sigma_{flow}} \dot{\varepsilon}^p = \infty$. This means that the equivalent stress will *never* reach the flow stress, $\sigma_e < \sigma_{flow}$, and puts a

stability limit on solutions based on stress-incrementation, where stresses very close to the yield stress may produce very large plastic strain increments $\Delta\varepsilon^p$. If the stress increment is so large that the equivalent stress exceeds the flow stress $\sigma_e > \sigma_{flow}$, the plastic strain increment becomes (non-physically) negative $\dot{\varepsilon}^p < 0$. An alternative formulation that does not exhibit this behaviour is

$$\dot{\varepsilon}^p = \dot{\varepsilon}^e \left(\frac{\sigma_e}{\sigma_{flow}} \right)^m . \tag{3.11}$$

This formulation does not guarantee $\sigma_e < \sigma_{flow}$. In the analytical solutions, sufficiently small increments are chosen, so that the stability limit is not an issue, and the formulation from Huang et al. [13] in Equation 3.9 is used.

Huang et al.'s viscoplastic-like formulation, Equation 3.9, has another attractive property, namely rate insensitivity. Introducing the equivalent deviatoric strain rate $\dot{\varepsilon}$, the loading speed does not affect the material response. Another effect is that if there is no change in elastic strain, $\dot{\varepsilon}^e_{ij} = 0$; there is no change in plastic strain, $\dot{\varepsilon}^p_{ij} = 0$. In other words, the plastic flow is similar to a viscoplastic formulation, yet does not exhibit rate sensitivity.

3.4 Material parameters

For analytical and finite element solutions in this thesis, the following material parameters are used:

$$\begin{aligned} E &= 210\,\text{GPa} \\ \sigma_y &= 420\,\text{MPa} \\ \nu &= 0.3 \\ N &= 0.2. \end{aligned}$$

These are compatible with the paper by Huang et al. [13], where $\sigma_y/E = 0.2\%$, $\nu = 0.3$ and $N = 0.2$. The flow rule exponent is taken as $m = 20$ for the formulation without a yield surface. In the limit $m \to \infty$, it is indistinguishable from a formulation with a yield surface.

In the case study, different material parameters are used. These are specified in the before the case study, in Chapter 8.

Chapter 4

Analytical solutions

This chapter presents analytical solutions a selection of problems presented by Huang et al. [13]. The problems represent fundamental loading cases. Uniaxial tension is studied in Section 4.1, where the strain gradient effect is induced using a gravitational body force. Second, shear is examined in Section 4.2. The strain gradient effect is induced using a prescribed plastic strain field. This problem is also useful for stability discussion. Thirdly, a thin beam in bending is analysed in Section 4.3, which naturally shows a difference in strain gradient effects in the height direction.

The chosen problems are simple. Changes are one-directional, and analytical solutions of the strain field, except for a final numerical integration to account for load incrementation and strain gradient effects, is straightforward. Straightforward analytical solutions allows for checking the correctness of the FEM implementation, which is done in Chapter 6.

4.1 Bar in uniaxial tension subject to gravity

Perhaps the simplest problem possible that shows strain gradient effects is a bar in linear uniaxial tension. The only non-zero stress is the normal stress in the x_1-direction σ_{11}, which depends only on the x_1 coordinate. For example, the magnitude of the gradient of the equivalent plastic strain is simply the size of its derivative in the x_1-direction, $\eta^{p,C} = ||\nabla \varepsilon^p|| = |\frac{\partial}{\partial x_1} \varepsilon^p|$.

The bar is loaded by gravity and end tension at the bottom ($x_1 = 0$), and constrained from moving at the top ($x_1 = L$), as shown in Figure 4.1. This

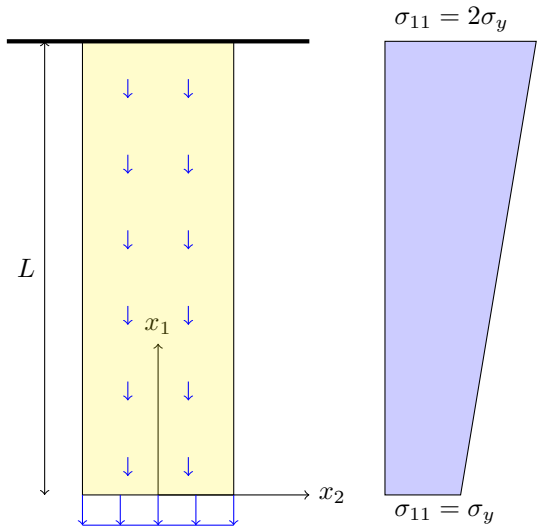

Figure 4.1: Uniaxial tension due to constant body force and end load. Coordinate system, load, boundary conditions and resulting stress field.

loading gives a stress field of $\sigma_{11}(x_1) = gx_1 + \sigma_{bottom}$. Choosing $\sigma_{bottom} = \sigma_y$ and $g = \sigma_y/L$ produces the linear stress field $\sigma_{11}(x_1) = (1 + \frac{x_1}{L})\sigma_y$.

To obtain the range of results we should be seeing, take the hardening function in Equation 3.5 and apply it to the top of the bar. At the top edge of the bar, the stress is double the yield stress $\sigma_{11}(x_1 = L) = 2\sigma_y$, implying $\sigma_{flow} = \sigma_y f(\varepsilon^p) = 2\sigma_y$ and $f(\varepsilon^p) = 2$ when strain gradient effects are neglected. Solved for equivalent plastic strain, $\varepsilon^p = 0.062$ is obtained. This is shown to be accurate in Figure 4.2, where the maximum strain is 0.062 ($l/L = 0$).

4.1.1 Analytical solution

The only non-zero stress is σ_{11}, giving deviatoric stress tensor components $\sigma'_{11} = \frac{2}{3}\sigma_{11}$ and $\sigma'_{22} = \sigma'_{33} = -\frac{1}{3}\sigma_{11}$. The equivalent stress is $\sigma_e = \sigma_{11}$. Inserted into

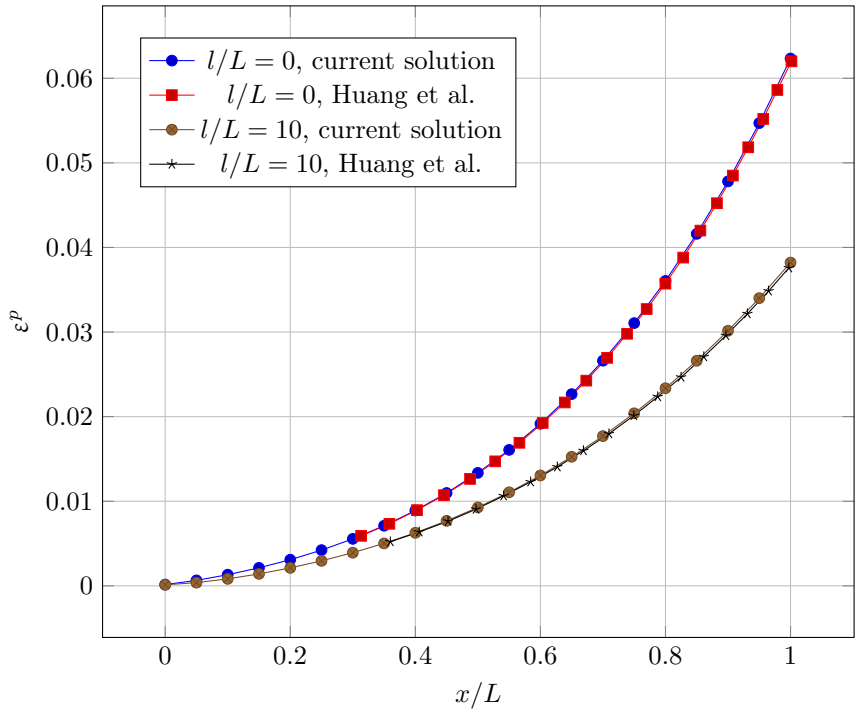

Figure 4.2: Plastic strain distribution in bar. Correspondence with results presented by Huang et al. [13]. $\eta^p = \eta^{p,A}$. Huang's plot is extracted using image recognition from his paper, introducing slight inaccuracy.

the constitutive equation (3.1) gives strain rates

$$\dot{\varepsilon}_{11} = \dot{\varepsilon}^e_{11} + \dot{\varepsilon}^p_{11} = \frac{\dot{\sigma}_{11}}{E} + \dot{\varepsilon}\left(\frac{\sigma_e}{\sigma_{flow}}\right)^m \tag{4.1a}$$

$$\dot{\varepsilon}_{22} = \dot{\varepsilon}_{33} = \dot{\varepsilon}^e_{22} + \dot{\varepsilon}^p_{22} = -\nu\frac{\dot{\sigma}_{11}}{E} - \frac{\dot{\varepsilon}}{2}\left(\frac{\sigma_e}{\sigma_{flow}}\right)^m. \tag{4.1b}$$

Dependence on the equivalent strain rate $\dot{\varepsilon}$ in equations 4.1 is eliminated by inserting for the strains in directions x_2 and x_3. Deviatoric strains $\varepsilon'_{ij} = \varepsilon_{ij} - \varepsilon_{kk}/3$ are $\varepsilon'_{11} = \frac{2}{3}(\varepsilon_{11} - \varepsilon_{22})$ and $\varepsilon'_{22} = \frac{1}{3}(-\varepsilon_{11} + \varepsilon_{22})$, giving the equivalent

strain rate $\dot{\varepsilon} = \sqrt{\frac{3}{2}\dot{\varepsilon}'_{ij}\dot{\varepsilon}'_{ij}} = \frac{2}{3}(\varepsilon_{11} - \varepsilon_{22})$, and the strain rates become

$$\dot{\varepsilon}_{11} = \frac{\dot{\sigma}_{11}}{E} + \frac{2}{3}(\dot{\varepsilon}_{11} - \dot{\varepsilon}_{22}) \left(\frac{\sigma_e}{\sigma_{flow}} \right)^m \tag{4.2a}$$

$$\dot{\varepsilon}_{22} = -\nu \frac{\dot{\sigma}_{11}}{E} - \frac{1}{3}(\dot{\varepsilon}_{11} - \dot{\varepsilon}_{22}) \left(\frac{\sigma_e}{\sigma_{flow}} \right)^m . \tag{4.2b}$$

Eliminating $\dot{\varepsilon}_{22}$ from the two equations, $\dot{\varepsilon}_{11}$ is isolated,

$$\dot{\varepsilon}_{11} = \left[1 + \frac{2}{3}(1+\nu) \frac{\left(\frac{\sigma_e}{\sigma_{flow}} \right)^m}{1 - \left(\frac{\sigma_e}{\sigma_{flow}} \right)^m} \right] \frac{\dot{\sigma}_{11}}{E}. \tag{4.3}$$

Inserting the equivalent strain rate $\dot{\varepsilon} = \frac{2}{3}(\dot{\varepsilon}_{11} - \dot{\varepsilon}_{22})$ into the equation for plastic flow 3.9 gives the plastic strain rate. A less tedious approach is subtracting Equation 3.9 from Equation 4.1a, giving $\dot{\varepsilon}_{11} - \dot{\varepsilon}^p = \frac{\dot{\sigma}_{11}}{E}$. The explicit expression for the plastic strain rate becomes

$$\dot{\varepsilon}^p = \frac{2}{3}(1+\nu) \frac{\left(\frac{\sigma_e}{\sigma_{flow}} \right)^m}{1 - \left(\frac{\sigma_e}{\sigma_{flow}} \right)^m} \frac{\dot{\sigma}_{11}}{E}. \tag{4.4}$$

With change only in the x_1-direction, the strain gradient for each of the cases can be expressed with the effective plastic strain's derivative in the x_1-direction $\frac{\partial \varepsilon^p}{\partial x_1}$. The different measures of the effective strain gradient η^p become

$$\eta^{p,A} = \sqrt{\frac{5}{8}} \left| \frac{\partial \varepsilon^p}{\partial x_1} \right| \approx 0.79 \left| \frac{\partial \varepsilon^p}{\partial x_1} \right| \tag{4.5a}$$

$$\eta^{p,B} = \frac{\sqrt{3}}{2} \left| \frac{\partial \varepsilon^p}{\partial x_1} \right| \approx 0.87 \left| \frac{\partial \varepsilon^p}{\partial x_1} \right| \tag{4.5b}$$

$$\eta^{p,C} = \left| \frac{\partial \varepsilon^p}{\partial x_1} \right| . \tag{4.5c}$$

The differential equation is solved explicitly: the plastic strain of the last step is used to compute hardening, both isotropic and strain gradient related. The change of plastic strain in the x_1-direction is computed using the central difference method for internal elements and using skew differences for the edges

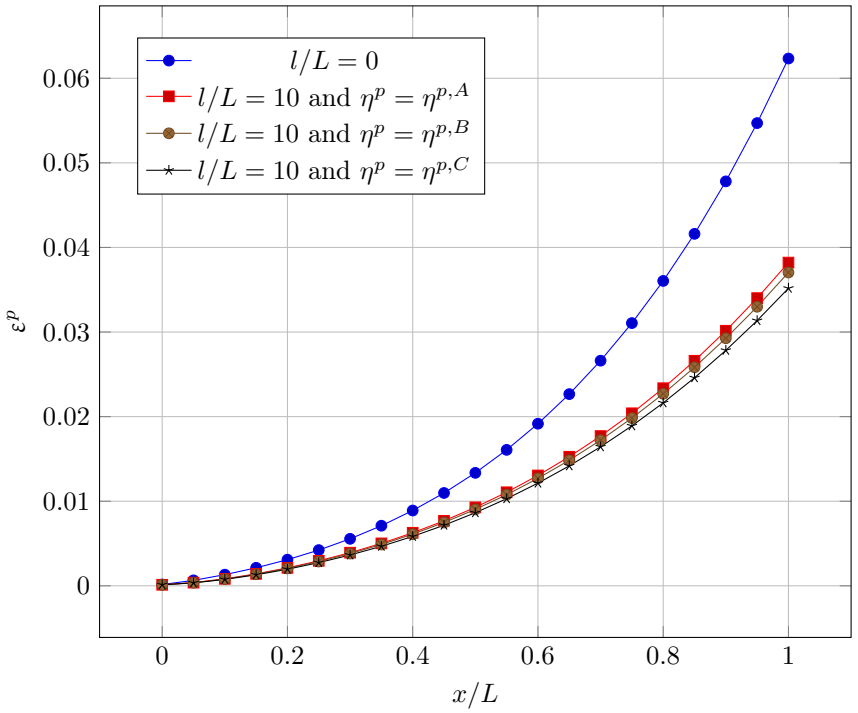

Figure 4.3: Plastic strain distribution in bar; different measures of η^p. As expected, smaller length scale, thereby larger l/L gives stiffer results. Results with different strain gradient measures η^p are similar.

$$\left.\frac{\mathrm{d}\varepsilon^p}{\mathrm{d}x_1}\right|_{x_1=0} = \frac{-\varepsilon^p(2\Delta x_1) + 4\varepsilon^p(\Delta x_1) - 3\varepsilon^p(0)}{2\Delta x_1} \tag{4.6a}$$

$$\left.\frac{\mathrm{d}\varepsilon^p}{\mathrm{d}x_1}\right|_{x_1=L} = \frac{\varepsilon^p(L - 2\Delta x_1) - 4\varepsilon^p(L - \Delta x_1) + 3\varepsilon^p(L)}{2\Delta x_1} \tag{4.6b}$$

$$\left.\frac{\mathrm{d}\varepsilon^p}{\mathrm{d}x_1}\right|_{\text{otherwise}} = \frac{\varepsilon^p(x_1 + \Delta x_1) - \varepsilon^p(x_1 - \Delta x_1)}{2\Delta x_1}. \tag{4.6c}$$

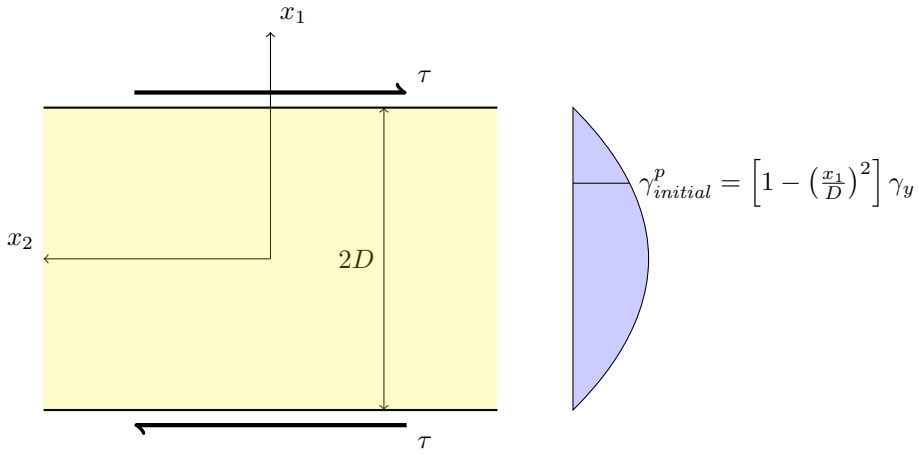

Figure 4.4: Coordinate definition, load and initial plastic strain distribution for the infinite shear layer. Note that the x_1-direction points up. The layer is infinitely long in the x_2-direction, thus there are no bending effects. Strain gradient effects arise solely due to initial plastic strain, and disappears when the strain increases.

4.1.2 Results and discussion

The analytical solution produced for this thesis corresponds well with Huang et al.'s plot, as shown in Figure 4.2. The results of using different measures of the effective plastic strain gradient is shown in Figure 4.3.

Correspondence with Huang et al.'s plots is good. Increasing the material length scale l increases hardening, as is expected.

4.2 Shear of an infinite layer

Testing how the current strain gradient plasticity theory handles shear strain is relevant, and the chosen example problem provides simple geometry. There is change only in the x_1-direction, and the only nonzero stresses and strains are $\sigma_{12} = \sigma_{21}$ and $\varepsilon_{12} = \varepsilon_{21}$. Using a prescribed, non-uniform, smooth residual plastic shear strain introduces strain gradient effects with minimal complications. As stresses increase, the strain distribution should become uniform.

The second problem used for verification is a sheared infinite layer, visualized in Figure 4.4. The infinite length prevents bending effects, and the result is pure

shear.

The initial plastic shear strain is distributed in the layer as the parabola

$$\gamma^p_{initial} = \left[1 - \left(\frac{x_1}{D}\right)^2\right] \gamma_y, \tag{4.7}$$

where γ_y is equal to the elastic engineering shear strain at yielding $\gamma_y = \tau_y/\mu = \sigma_y/(\sqrt{3}\mu)$. This differs from Huang et al.'s paper [13], which is discussed in Section 4.2.2. Only half the layer is analysed because of symmetry. The top and bottom edges are sheared, leading to a uniform stress distribution $\sigma_{12} = \sigma_{21} = \tau$.

4.2.1 Analytical solution

For a stress field where the only non-zero stress is the shear stress $\sigma_{12} = \sigma_{21} = \tau$, the only strain rates will be the shear strain rates

$$\dot{\varepsilon}_{12} = \dot{\varepsilon}_{21} = \frac{1}{2}\dot{\gamma}. \tag{4.8}$$

The constitutive Equation 3.1 for pure shear becomes

$$\dot{\varepsilon}_{12} = \frac{\dot{\sigma}'_{12}}{2\mu} + \frac{3\dot{\varepsilon}^p}{2\sigma_e}\sigma'_{12}. \tag{4.9}$$

The equivalent strain rate is $\dot{\varepsilon} = \sqrt{\frac{2}{3}\dot{\varepsilon}'_{ij}\dot{\varepsilon}'_{ij}} = \frac{1}{\sqrt{3}}\dot{\gamma}$, giving the equivalent plastic strain rate $\dot{\varepsilon}^p = \dot{\varepsilon}(\sigma_e/\sigma_{flow})^m = \frac{\dot{\gamma}}{\sqrt{3}}(\sigma_e/\sigma_{flow})^m$. Using $\sigma_e = \sqrt{3}\tau$, Equation 4.9 can be written

$$\dot{\gamma} = \frac{\dot{\tau}}{\mu} + \left(\frac{\sigma_e}{\sigma_{flow}}\right)^m \dot{\gamma}, \tag{4.10}$$

which solved for $\dot{\gamma}$ gives

$$\dot{\gamma} = \frac{1}{1 - \left(\frac{\sigma_e}{\sigma_{flow}}\right)^m} \frac{\dot{\tau}}{\mu}. \tag{4.11}$$

As for the uniaxial case, Equation 3.9 gives the plastic flow from the equivalent strain rate as

$$\dot{\varepsilon}^p = \frac{1}{\sqrt{3}} \frac{\left(\frac{\sigma_e}{\sigma_{flow}}\right)^m}{1 - \left(\frac{\sigma_e}{\sigma_{flow}}\right)^m} \frac{\dot{\tau}}{\mu}. \tag{4.12}$$

Given that $\gamma^p = \sqrt{3}\varepsilon^p$ and $\tau_y = \frac{1}{\sqrt{3}}\sigma_y$, plotting normalized equivalent plastic strain is equivalent to normalized plastic shear strain $\varepsilon^p/\varepsilon_y = \gamma^p/\gamma_y$.

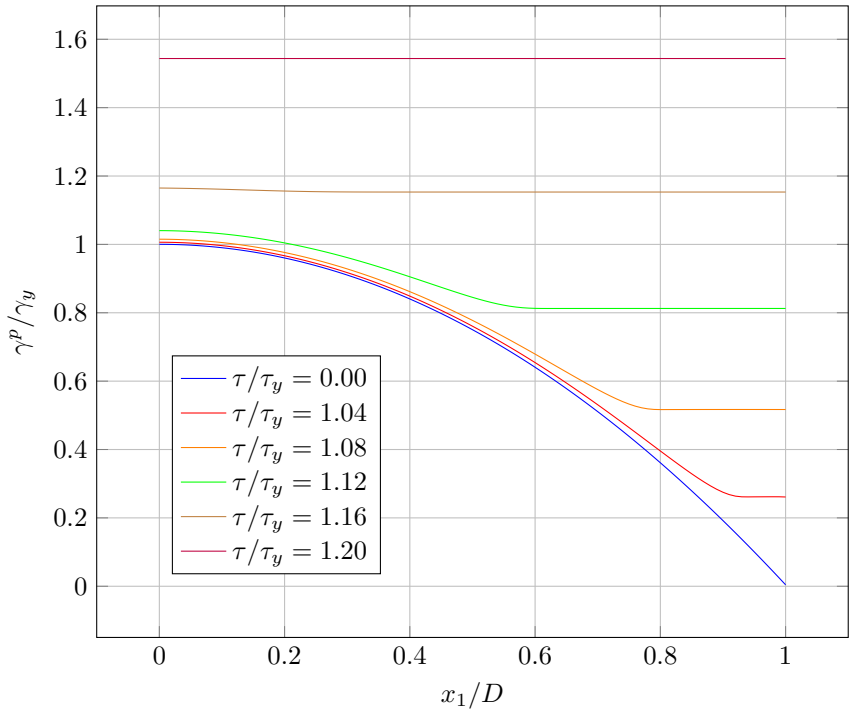

Figure 4.5: Analytical solution: distribution of normalized engineering plastic shear strain for $l/D = 3$, using Huang et al.'s definition of $\eta^p = \eta^{p,A}$.

The effective plastic strain gradient is the same for Huang et al.'s measures $\eta^{p,A} = \eta^{p,B} = \frac{\sqrt{3}}{2}|\frac{\mathrm{d}\varepsilon^p}{\mathrm{d}x_1}|$. The measure introduced here is $\eta^{p,C} = ||\nabla\varepsilon^p|| = |\frac{\mathrm{d}\varepsilon^p}{\mathrm{d}x_1}|$.

4.2.2 Results and discussion

Note first that this example shows *no plastic strain gradient hardening*. The only part of the model with a nonzero plastic strain gradient is in the prescribed field. Here, however, there is no yield until the plastic strain field smooths out, and $\gamma^p > \gamma_y$ for the whole model. Yielding is initiated close to the edge $x_1 = D$, and as strains increase, yielding moves closer and closer to the centre $x_1 = 0$. Strain gradient effects are thus only relevant in *the intersection between yielding and not yielding*. Here, however, the strain gradient is singular. How this should be

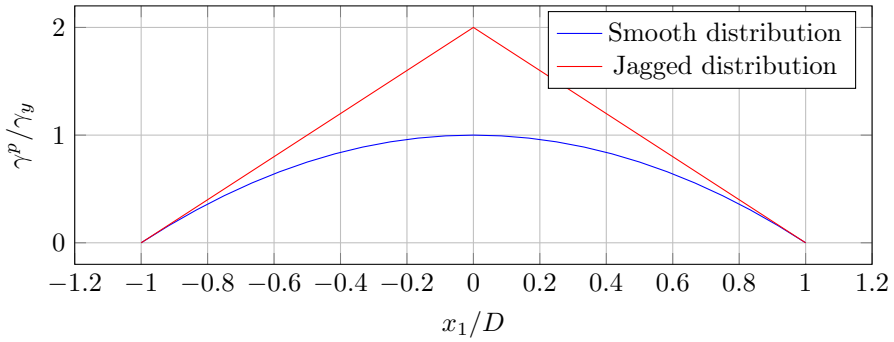

Figure 4.6: Illustration of Niordson and Hutchinson's argument for the smoothness of strain gradient plasticity hardening. The smooth distribution is considered physical, the jagged non-physical. Note that the whole domain has been plotted to illustrate the need of $\frac{\mathrm{d}\gamma^p}{\mathrm{d}x_1}|_{x_1=0}= 0$, as symmetry requires $\gamma^p(x_1) = \gamma^p(-x_1)$. In addition, the strain gradient in the origin, with contribution from $\frac{\partial\gamma^p}{\partial x_1}(x_1 = 0)$, is undefined.

handled is discussed in Appendix A.

Results of the analytical solution are plotted in Figure 4.5. The initial plastic shear distribution is shown for the plot where $\tau = 0$. As the shear stress increases, additional plastic shear is accumulated, hardening the layer. Due to the viscoplastic-like formulation 3.9, plastic flow is present as long as there is elastic flow, which is seen left in the figure, where $x_1 \approx 0$. Increased loading produces increased hardening, and gradient effects smooth out the response. Over time, the less pre-strained region ($x_1 \approx D$) hardens more than the pre-strained center ($x_1 \approx 0$), and for large stresses ($\tau > 1.16\tau_y$), the strain distribution is practically constant, and strain gradient effects vanish.

This problem was not originally chosen by Huang et al. for its demonstration of strain gradient effects on shearing, but to check for defects previous lower-order strain gradient plasticity models have been prone to.

Niordson and Hutchinson [18] used this example to illustrate bad behaviour of a lower order strain gradient theory presented by Bassani [2]. The current strain gradient theory does not involve any stresses work-conjugate to the strain gradient, and is therefore a lower order theory. The ill-behaved strain gradient plasticity theory showed a vertex at the centre, $x_1 = 0$, which is fundamentally different from what we expect from a strain gradient theory. When the hardness depends on the plastic strain gradient in addition to the plastic strain,

the resulting strain distribution is expected to be smoother than the resulting plastic strain distribution without taking strain gradient theory into account. Bassani [2] formulated the material hardening as

$$\dot{\tau}_y = h(\gamma^p, \alpha)\dot{\gamma}^p \tag{4.13a}$$

$$h(\gamma^p, \alpha) = h_0 \left(\frac{\gamma^p}{\gamma_0} + 1 \right)^{N-1} \sqrt{1 + \frac{(l\alpha/\gamma_0)^2}{1 + c(\gamma^p/\gamma_0)^2}}. \tag{4.13b}$$

Here, variables (with units) are, h_0 (MPa) is a reference tangent modulus, $N \approx 0.15$ $(-)$ a non-dimensional parameter, $c = 1$ or $c = 0$ $(-)$ a non-dimensional parameter, γ_0 $(-)$ a reference plastic shear strain and α (m^{-1}) a measure of the strain gradient η^p based on the curvature tensor introduced by Fleck [9]. The incremental hardening formulation makes hardening *path dependent* in the space of the plastic strain and the plastic strain gradient. Two different loading procedures will produce different hardening depending on how the strain is applied. Incrementing first the plastic strain gradient and then the plastic strain (a) will produce the the most hardening, as the term under the root is as large as possible when increasing the plastic strain. In contrast, first incrementing the plastic strain and then increasing the strain gradient (b) produces *no* strain gradient effect at all! Under the current theory of hardening as a function of dislocation density, this makes no sense.

In the current shear problem, the gradient is initially larger close to the edge $x_1 = D$. This leads to a larger incremental hardening for the same increase in effective plastic strain when the strain gradient is higher, and the effect is close to (a). For the centre of the bar, the opposite is the case (b). Plastic strain is incremented first, and there is less increase in hardening for the same increase in plastic strain. Using the current 1-1 correspondence between ε^p, and η^p; and the actual hardening alleviates this problem.

The problem is worsened when $N \to 0$. Niordson and Hutchinson argue that a parabolic strain distribution should show the most hardening at a local maximum of the equivalent plastic strain ε^p, given smooth loading and smooth boundary conditions. The current analytical hardening function satisfies this requirement ($\frac{\mathrm{d}\gamma^p}{\mathrm{d}x_1}|_{x_1=0} = 0$). Niordson and Hutchinson give an extensive discussion of these issues [18].

Huang et al.'s figure 7 [13] uses a wrongly normalized shear stress. The figure gives the impression that the normalized shear stress tau_0 is the actual yield shear stress τ_y. The correct yield shear stress is found calculating the von

Mises equivalent stress from pure shear, yielding

$$\tau_y = \frac{1}{\sqrt{3}}\sigma_y$$

where σ_y is the uniaxial normal yield stress. Huang et al. derive the normalized shear stress from a normalized shear strain

$$\tau_0 = \mu\gamma_0 \quad \text{where} \quad \gamma_0 = \sqrt{3}\frac{\sigma_y}{E}.$$

Inserting for γ_0 and using $\mu = \frac{E}{2(1+\nu)}$ the normalized shear is obtained in terms of the yield stress

$$\tau_0 = \frac{E}{2(1+\nu)} \times \sqrt{3}\frac{\sigma_y}{E} = \frac{\sqrt{3}}{2(1+\nu)}\sigma_y \neq \tau_y.$$

Using correct yield shear stress τ_y and engineering shear yield strain $\gamma_y = \tau_y/\mu$, the plots from Huang et al.'s report may be reproduced. Note that the ratio of engineering plastic shear strain to engineering shear yield strain, is the same as the ratio of effective plastic strain to yield strain $\frac{\gamma^p}{\gamma_y} = \frac{\varepsilon^p}{\varepsilon_y}$. Correctly normalized plots are presented in Figure 4.5.

4.3 Bending of thin beams

Bending of thin beams has previously been used by Stölken and Evans [21] to find the material length scale l for Nickel, using strain gradient theory based on work by Fleck and Hutchinson [8]. This theory accounts for strain gradient effects by augmenting the effective strain with contributions from the strain gradient $\varepsilon_{ij,k}$ and the curvature tensor. Using virtual work or minimal potential energy, equilibrium equations are obtained. The equilibrium equations necessitate higher order strains work-conjugate to the strain gradient components. Huang et al. [13] later applied lower-order strain gradient plasticity theory to the same problem, which is again done in this section.

Figure 4.7 shows the problem with loads and coordinate system. The beam is very thin, making strain gradient effects relevant. Huang et al. assume the beam to be incompressible ($\nu = 0.5$). This is also assumed in the current solution, but through incompressible plastic deformation. The beam is bent about the x_3-axis, and is in a plane strain state, so that the only non-zero strains are ε_{11} and $\varepsilon_{22} = -\varepsilon_{11}$ from incompressibility, where the strain in the beam

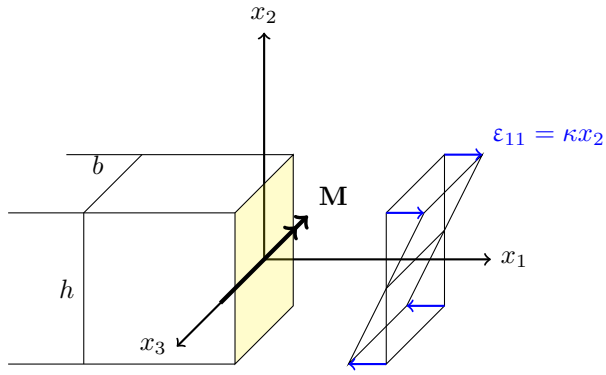

Figure 4.7: Coordinate definition for the thin beam problem. The applied moment gives tension in the top area and compression in the bottom area.

direction is given by the curvature as $\varepsilon_{11} = \kappa x_2$. Incompressibility combined with plane strain gives non-zero stresses σ_{11} and $\sigma_{22} = \frac{1}{2}\sigma_{11}$, and the equivalent stress becomes $\sigma_e = \sqrt{\frac{3}{2}\sigma'_{ij}\sigma'_{ij}} = \frac{\sqrt{3}}{2}|\sigma_{11}|$. The top of the beam is in tension, and the bottom in compression. If we had not constrained the strains in the x_3-direction, the beam cross section area would change significantly, and an analytical solution would have to take non-linear geometric effects into account. The top area, in tension, and the neutral axis would move down, as the bottom area increased in compression. In the examination of thin beam bending, large strains are assumed, so that $\varepsilon^e_{ij} \approx 0$ and $\varepsilon_{ij} \approx \varepsilon^p_{ij}$. This alleviates the need for a viscoplastic-like formulation: when only plastic strains are taken into account, there are no loading-unloading conditions, and the yield surface variant of the material model from Equation 3.5 is used. This gives a simple hardening formulation where the stresses are given explicitly from the equivalent plastic strain, $\sigma_e = \sigma_{flow} = \sigma_y\sqrt{f(\varepsilon^p)^2 + l\eta^p}$.

4.3.1 Analytical solution

These simplifications allow for a time and loading-independent solution of the beam bending problem. Huang et al. plot a non dimensional bending moment $\frac{M}{\sigma_y h^2 b}$[1] vs non dimensional curvature κh. The bending moment on the surface

[1] Huang et al. [13] write $\frac{M}{\sigma_y h^2}$. This is equal to the current expression for a beam of unit width $b = 1$.

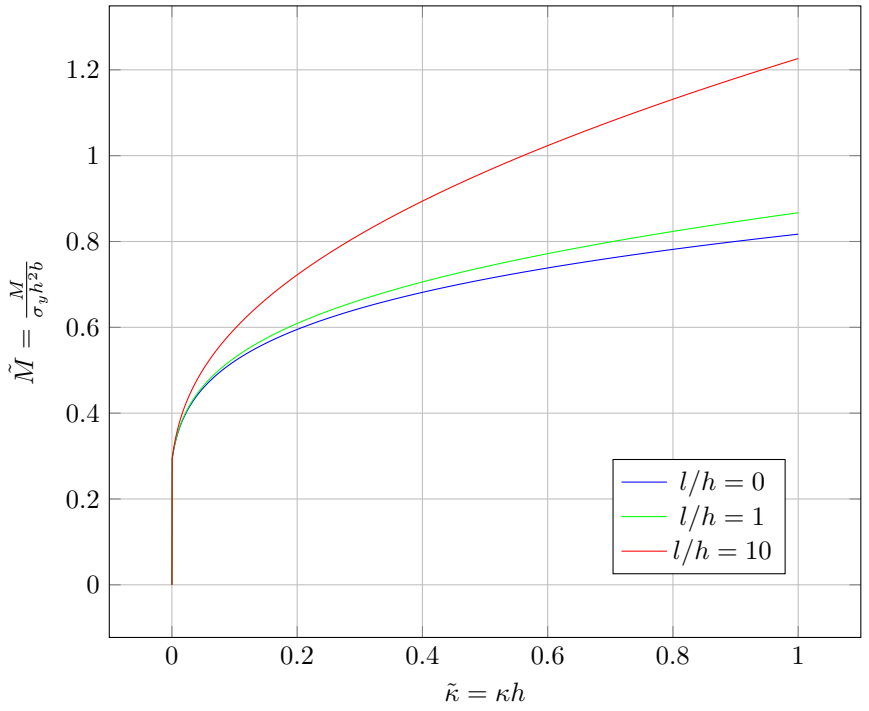

Figure 4.8: Bending of thin beams. Analytical solution, non-dimensional moment versus non-dimensional curvature. $l/h \in [0, 1, 10]$.

with normal $\mathbf{e_1}$ is the integral of stresses in the x_1 direction times its distance to the neutral axis over the area $M = \int_A \sigma_{11} x_2 \, \mathrm{d}A$. Normal stress σ_{11} can be expressed from the flow stress. The flow stress depends on the equivalent plastic strain ε^p and the effective plastic strain gradient η^p, giving the normal stress

$$\sigma_{11} = \frac{2}{\sqrt{3}} \sigma_e \tag{4.14}$$

$$= \frac{2}{\sqrt{3}} \sigma_y \sqrt{f(\varepsilon^p)^2 + l\eta^p}. \tag{4.15}$$

As elastic strains are neglected, the effective plastic strain varies linearly over the area $\varepsilon^p = \frac{2}{\sqrt{3}} \kappa x_2$, thus its only non-zero gradient component is $\frac{\mathrm{d}\varepsilon^p}{\mathrm{d}x_2} = \frac{2}{\sqrt{3}} \kappa$. Inserting for isotropic hardening ($f(\varepsilon^p)$) and plastic strain gradient harden-

ing ($l\eta^p$), we get non-dimensional moment $\tilde{M} = \frac{M}{\sigma_y h^2 b}$ as a function of non-dimensional curvature $\tilde{\kappa} = \kappa h$ as

$$\tilde{M} = \int_{-\frac{1}{2}}^{\frac{1}{2}} \frac{2}{\sqrt{3}} \tilde{x}_2 \sqrt{\left(1 + \frac{2E}{\sqrt{3}\sigma_y} \tilde{\kappa} \tilde{x}_2\right)^{2N} + \frac{l}{h} \left| \frac{\mathrm{d}\varepsilon^p}{\mathrm{d}\tilde{x}_2} \right|} \, \mathrm{d}\tilde{x}_2 \tag{4.16}$$

where $\tilde{x_2} = \frac{x_2}{h}$, for the case of $\eta^p = \eta^{p,C}$. This is formulation is path independent, and response at a given curvature can be calculated directly without incrementation. All rate variables, such as $\dot{\varepsilon}^p$ and $\dot{\sigma}_{11}$, have been eliminated. The result is similar for plane stress[2]. Other definitions of η^p give different factors in front of the partial derivative of the equivalent plastic strain. The resulting expression can be integrated for any choice of curvature κh and material length scale $\frac{l}{h}$.

4.3.2 Results and discussion

Huang et al. chose very large values for the curvature, so that $\kappa h \in [0, 10]$. In this range, the elastic domain is negligible, and it is impossible to separate his plot from the y-axis. Strains of this magnitude, however, are impossible to obtain. The maximum possible physical solution is the limit $\kappa h \to 2$. Beam theory then gives the length change ratio

$$\frac{\Delta l}{l_0} = \kappa x_2.$$

In the bottom of the beam, the length change is

$$\frac{\Delta l}{l_0}_{\,bottom} = \kappa \frac{-h}{2} = -1. \tag{4.17}$$

The logarithmic strain becomes

$$\varepsilon^l_{bottom} = \lim_{\Delta l \to -l_0} \ln \frac{l_0 + \Delta l}{l_0} = -\infty. \tag{4.18}$$

In conclusion, requiring non-negative mass in the bottom of the beam limits the curvature to $\kappa h < 2$.

[2]For plane stress, $\sigma_{11} = \sigma_e$, which gives the non-dimensional moment $\tilde{M} = \int_{-\frac{1}{2}}^{\frac{1}{2}} \tilde{x}_2 \sqrt{\left(1 + \frac{2E}{\sqrt{3}\sigma_y} \tilde{\kappa} \tilde{x}_2\right)^{2N} + \frac{l}{h} \frac{\mathrm{d}\varepsilon^p}{\mathrm{d}\tilde{x}_2}} \, \mathrm{d}\tilde{x}_2$. Changes in cross section area are neglected.

Results are shown in Figure 4.8, and match Huang et al.'s results very well, when using $\eta^p = \eta^{p,A} = \frac{\sqrt{3}}{2}|\frac{\mathrm{d}\varepsilon^p}{\mathrm{d}x_2}|$, given the assumption of $\varepsilon^e_{ij} \approx 0$ and differences in curvature domain.

In the experiments by Stölken and Evans [21], surface strains are in the range of $\varepsilon_{max} \in (0.02, 0.09)$. Kinematics give the relation between curvature and bending strains as $\varepsilon_{max} = 2\frac{h}{R} = 2\kappa h$, so that the non-dimensional curvature κh is in the range of $\kappa h \in (0.04, 0.18)$.

This problem shows that in Huang et al.'s formulation, when the plastic strain gradient increases proportionally to the plastic strain, the effect of the plastic strain gradient dominates the effect of the equivalent plastic strain. This comes from the formulation of the hardening, which (inserted for $N = 0.2$) is

$$\sigma_{flow} = \sigma_y \sqrt{\left(1 + \frac{E\varepsilon^p}{\sigma_Y}\right)^{0.4} + l\eta^p}. \tag{4.19}$$

The hardening term from the plastic strain is raised to a "total" power of 0.2, whereas the hardening term from the plastic strain gradient is raised to a "total" power of 0.5.

Chapter 5

Finite element implementation

This chapter gives the foundation of the numerical strain gradient plasticity implementation used in the finite element simulations.

In each time increment, the effective plastic strain gradient η^p is calculated from the field of equivalent plastic strain $\varepsilon^p(x, y, z)$ from the previous increment. This procedure is described in Section 5.3. Then, an iterative strain increment is calculated using iterative radial rate of return [11]. Iterative radial rate of return is not described in detail in this thesis, and is not a necessary requirement for understanding the strain gradient implementation.

In the following chapter, analytical expressions are presented for 3D analysis. Specialization to 2D is straightforward. Figures are in 1D and 2D for ease.

5.1 Finite element method notation

This section does not seek to teach the finite element method, but to establish the notation used. Comprehensive theory is available in literature. FEM notation in this chapter is taken from lecture notes by Odd Sture Hopperstad and Tore Børvik [12], which describes implementation of non-linear material behaviour using the finite element method. Linear theory and different element types is described in detail by Kolbein Bell [3], and for general non-linear finite element theory not restricted to the material level, see Cook et al.'s textbook [6].

The finite element method translates material continuum equations to a

discrete set of equations. In linear finite element method, the set of equations is linear. Introduction of non-linear effects on the material level, for example plasticity, makes the set of equations non-linear. Following is a summary of the derivation of the finite element method using the principle of virtual work. For a complete derivation, see Hopperstad and Børvik's lecture notes [12], chapter 4.5.

Let the volume of the body be divided into n_e element volumes $V = \sum_1^{n_e} V_e$. Approximate the displacement within an element volume as an interpolation of displacements in the element nodes

$$\mathbf{u}(\mathbf{x}, t) = \mathbf{N}_e(\mathbf{x})\mathbf{v}_e(t) \quad \text{where} \quad \mathbf{x} \in V_e. \tag{5.1}$$

It is noted that the interpolation functions $\mathbf{N}(\mathbf{x})$ depend on space only, whereas the nodal degrees of freedom $\mathbf{v}_e(t)$ depend on time. For simplicity, the space and time parameters are omitted. Here, $\mathbf{x} = \begin{bmatrix} x_1 & x_2 & x_3 \end{bmatrix}^T$ are coordinates in the undeformed configuration, $\mathbf{u} = \begin{bmatrix} u_1 & u_2 & u_3 \end{bmatrix}^T$ is the displacement vector with components in x, y and z-directions. The nodal degrees of freedom $\mathbf{v}_e = \begin{bmatrix} \mathbf{v}_{e,x} & \mathbf{v}_{e,y} & \mathbf{v}_{e,z} \end{bmatrix}$ are displacements in each of the dimensions, in each of the element nodes. The components of $\mathbf{N}_e$ are nodal interpolation functions creating a continuous displacement field from the nodal degrees of freedoms. These are taken as polynomials.

To avoid fourth order tensors, strain and stress tensors are lumped into vectors. The strain vector $\boldsymbol{\varepsilon}$ (in contrast to the strain tensor ε_{ij}) is

$$\boldsymbol{\varepsilon} = \begin{bmatrix} \varepsilon_1 \\ \varepsilon_2 \\ \varepsilon_3 \\ \varepsilon_4 \\ \varepsilon_5 \\ \varepsilon_6 \end{bmatrix} = \begin{bmatrix} \varepsilon_{11} \\ \varepsilon_{22} \\ \varepsilon_{33} \\ \gamma_{23} \\ \gamma_{31} \\ \gamma_{12} \end{bmatrix} = \begin{bmatrix} \varepsilon_{11} \\ \varepsilon_{22} \\ \varepsilon_{33} \\ 2\varepsilon_{23} \\ 2\varepsilon_{31} \\ 2\varepsilon_{12} \end{bmatrix}. \tag{5.2}$$

Abaqus/Explicit indexes in a different order[1]. The stress vector is

$$\boldsymbol{\sigma} = \begin{bmatrix} \sigma_1 \\ \sigma_2 \\ \sigma_3 \\ \sigma_4 \\ \sigma_5 \\ \sigma_6 \end{bmatrix} = \begin{bmatrix} \sigma_{11} \\ \sigma_{22} \\ \sigma_{33} \\ \tau_{23} \\ \tau_{31} \\ \tau_{12} \end{bmatrix}. \tag{5.3}$$

[1] In the Abaqus/Explicit solver, the order of the shear strains is $\gamma_{12}, \gamma_{23}, \gamma_{31}$. Abaqus/Implicit uses the same ordering as presented in this text.

The strains are given from displacements as

$$\varepsilon_{ij} = \frac{1}{2}\left(\frac{\partial u_i}{\partial x_j} + \frac{\partial u_j}{\partial x_i}\right), \tag{5.4}$$

which in vector/matrix notation is

$$\boldsymbol{\varepsilon} = \boldsymbol{\Delta}\mathbf{u} \quad \text{where} \quad \boldsymbol{\Delta} = \begin{bmatrix} \frac{\partial}{\partial x_1} & 0 & 0 \\ 0 & \frac{\partial}{\partial x_2} & 0 \\ 0 & 0 & \frac{\partial}{\partial x_3} \\ 0 & \frac{\partial}{\partial x_3} & \frac{\partial}{\partial x_2} \\ \frac{\partial}{\partial x_3} & 0 & \frac{\partial}{\partial x_1} \\ \frac{\partial}{\partial x_2} & \frac{\partial}{\partial x_1} & 0 \end{bmatrix}. \tag{5.5}$$

Displacements can be expressed in global degrees of freedom $\mathbf{r}$

$$\mathbf{u} = \mathbf{N}\mathbf{r} \quad \text{where} \quad \mathbf{N} = \sum_{e=1}^{n_e} \mathbf{N}_e \mathbf{a}_e \quad \text{and} \quad \mathbf{v}_e = \mathbf{a}_e \mathbf{r}. \tag{5.6}$$

Strains are now given in terms of global degrees of freedom

$$\boldsymbol{\varepsilon} = \boldsymbol{\Delta}\mathbf{N}\mathbf{r} = \mathbf{B}\mathbf{r}. \tag{5.7}$$

Let $\mathbf{b}$ be body forces, S the surface of the body and $\bar{\mathbf{t}}$ surface traction. The principle of virtual work becomes

$$\underbrace{\int_V \delta\boldsymbol{\varepsilon}^T \boldsymbol{\sigma}\, \mathrm{d}V}_{\text{internal virtual work}} = \underbrace{\int_V \delta\mathbf{u}^T \mathbf{b}\, \mathrm{d}V + \int_S \delta\mathbf{u}^T \bar{\mathbf{t}}\, \mathrm{d}S}_{\text{external virtual work}}. \tag{5.8}$$

Virtual strains $\delta\boldsymbol{\varepsilon}$ and displacements $\delta\mathbf{u}$ are expressed in terms of virtual nodal displacements $\delta\mathbf{r}$, and the set of equations become

$$\underbrace{\int_V \mathbf{B}^T \boldsymbol{\sigma}\, \mathrm{d}V}_{\mathbf{R}^{int}} = \underbrace{\int_V \mathbf{N}^T \mathbf{b}\, \mathrm{d}V + \int_S \mathbf{N}^T \bar{\mathbf{t}}\, \mathrm{d}S}_{\mathbf{R}^{ext}}. \tag{5.9}$$

For the case of a linear-elastic material, the stress-strain relation is given by Hooke's law $\boldsymbol{\sigma} = \mathbf{C}\boldsymbol{\varepsilon}$ and prescribed, conservative external loads, this simplifies to [12]

$$\mathbf{K}\mathbf{r} = \mathbf{R}^{ext} \quad \text{where} \quad \mathbf{K} = \int_V \mathbf{B}^T \mathbf{C}\mathbf{B}\, \mathrm{d}V. \tag{5.10}$$

Bell [3] uses a Taylor expansion of the displacement field to produce asymptotic bounds for displacements, stresses, strains and energy. It follows that the error e_α of a value α, which is a linear combination of mth derivatives of u, where u has been interpolated with polynomials of order p is bounded by

$$e_\alpha \in O(h^{p-m+1}), \tag{5.11}$$

where h is the size of the largest element in the mesh. Asymptotic upper-bound notation (O-notation) is defined by Cormen et al. [7] as a set of functions

$$f(n) \in O(g(n)) \iff \exists c, n_0 \in \mathbb{R}^+, \quad \forall n > n_0, \quad 0 \leq f(n) \leq cg(n). \tag{5.12}$$

Here the logic notation $\exists$ denotes "there exists some" and $\forall$ means "for all". Equation 5.12 in plain English becomes "The function $f(n)$ is in the set $O(g(n))$ if and only if there exists some non-negative, real constants c and n_0 such that for all n greater than n_0, $f(n)$ is smaller than or equal to $g(n)$". A simplified way of thinking about upper bound notation is as a rough less, or a measure of growth. For example $h(x) = 100x \log x$ grows slower than $i(x) = x^2$ for large values of x, therefore $h(x) \in O(i(x))$. This is shown by inserting $n = 1$ and $c = 100$ into Equation 5.12. Other choices of values, for example $n = 20$ and $c = 1$, are also possible.

5.2 Plastic strain gradient from integration points

Let $\mathbf{\Delta}^\eta$ be a linear operator containing constants and first order direction derivatives. We can then express the components contributing to the strain gradient as

$$\boldsymbol{\eta} = \mathbf{\Delta}^\eta \boldsymbol{\varepsilon} = \mathbf{\Delta}^\eta \mathbf{\Delta} \mathbf{N} \mathbf{v}. \tag{5.13}$$

In other words, the strain gradient vector depends on second order derivatives of the interpolation functions. Its error from Equation 5.11 is $O(h^{1-2+1}) = O(h^0)$ for full linear polynomials, in Table 5.1; and $O(h^{2-2+1}) = O(h^1)$ for full quadratic elements polynomials, in Table 5.2. In other words, to have an upper bound on the strain gradient, elements need to be interpolated with full polynomials of second order, and inter-element C^1 continuity. Using linear 2D interpolation, the single contribution to the plastic strain gradient would stem from the cross term xy. The strain gradient requires differentiating the displacement field twice. Components of the full 2D interpolated rectangle are shown in Table 5.1, and when differentiating with twice with respect to x or y, both 1, x and y disappear, and the single non-zero component of the strain

Table 5.1: Linear 2D interpolation.

$$\begin{array}{ccc} & 1 & \\ x & & y \\ & xy & \end{array}$$

Table 5.2: Quadratic 2D interpolation.

$$\begin{array}{ccccc} & & 1 & & \\ & x & & y & \\ x^2 & & xy & & y^2 \\ & x^2y & & xy^2 & \\ & & x^2y^2 & & \end{array}$$

gradient comes from the cross term xy, as $\frac{\partial^2 xy}{\partial x \partial y} = 1$. Variations in plastic strains over the x- and y-axes would be incorrectly represented.

C^1 continuous plane and solid elements, however, bring large challenges. For instance, each node would need 3 translational degrees of freedom for $\mathbf{u}$ and 9 for its gradient $\nabla\mathbf{u}$, a second order tensor. In addition, such theory would be unfit for explicit solvers, where lower-order elements are preferred. Higher order elements, in addition, are not often implemented adding degrees of freedom for derivatives of displacements, $\nabla\mathbf{u}$, instead by adding new nodes, which does not guarantee C^1 continuity.

Note that this section has considered the calculation of the *strain gradient* for the case of linear finite element analysis. The argument is also valid for the non-linear case of the *plastic strain gradient*, which is in general more complicated and less certain, and the error bounds will not be tighter than for the linear case.

A less formal argument is that if a value shall converge when using the finite element method, its potential must be continuous. Section 5.3 presents a solution.

5.3 Plastic strain gradient from nodal averaging

A simple way to ensure continuity of an otherwise discontinuous field in the finite element solution, is to require fixed values of the fields in nodes. If the surrounding element all agree on the same nodal field value, the field is continu-

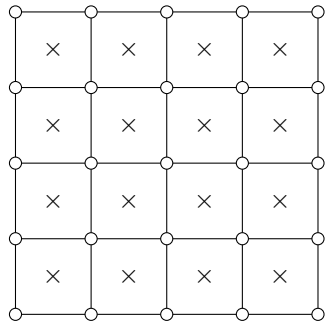

Figure 5.1: Element mesh, reduced integration. Integration points are marked $\times$. Nodes are circles $\circ$.

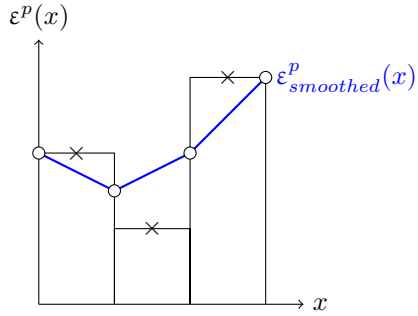

Figure 5.2: Nodal averaging applied to a one-dimensional discontinuous plastic strain field $\varepsilon^p(x)$.

ous. This can be achieved using average values from the surrounding nodes, and is similar to how modern finite element analysis software presents discontinuous fields that are discontinuous as a result of finite element method discretization, namely stress- and strain fields.

Instead of calculating the plastic strain gradient on the basis of a single element, calculate all the element contributions from integration points $\times$ to the plastic strain at corner nodes $\circ$. Node- and integration point positions for a two-dimensional mesh are shown in Figure 5.1 Then, average the contributions to the nodes, and use the averaged values of the plastic strain to compute the plastic strain gradient within an element. The averaged strain field is illustrated

as the blue line in Figure 5.2.

Chapter 6

Verification study

This chapter presents finite element solutions to the reference problems from Chapter 4, and compares the finite element solutions to the analytical solutions. When comparing the bar loaded by gravity and the shear of the infinite layer, some difference is expected. Here, the analytical solutions are based on the viscoplastic-like formulation where $\dot{\varepsilon}^p = \dot{\varepsilon}(\frac{\sigma_e}{\sigma_{flow}})^m$, where $m = 20$, in contrast to the finite element solution, in which $m \to \infty$. In other words, the analytical solutions have no yield surface, and some degree of flow is expected even if the stress is lower than the yield stress. The analytical solution to the bending problem, however, uses a yield surface, but assumes elastic strains to be negligible.

Analytical solutions in Chapter 4 were compared to solutions by Huang et al., who used the effective plastic strain gradient measure $\eta^p = \eta^{p,A}$. The finite element implementation supports $\eta^p = \eta^{p,C}$, and finite element solutions are compared to analytical solutions with the same effective plastic strain gradient measure $\eta^p = \eta^{p,C}$.

6.1 Bar loaded by gravity

The first model for finite element analysis is the bar loaded by uniaxial tension and gravity, first analysed analytically in Section 4.1. Monotonically increasing load over the height of the bar gives a smooth strain response, and there is no "trigger" to numerical instabilities.

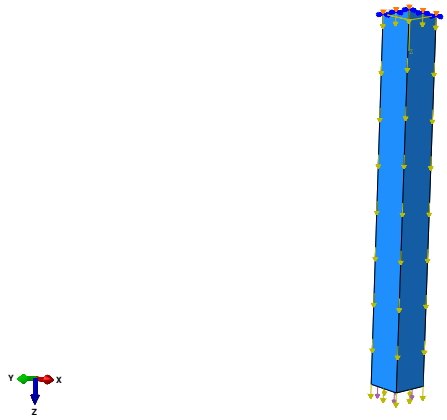

Figure 6.1: Finite element model for the bar loaded by gravity. Note that the finite element model shows x_3 as the height direction, whereas x_1 is used for the height direction for the rest of this section.

6.1.1 Finite element model

Figure 6.1 shows the finite element model used for analysing the bar loaded by gravity. 100 elements was used in the height, and a single element in the thickness direction.

In the analytical model, the bar is pinned at $x = L$. For the finite element model, this is achieved restricting $u_1 = 0$. Movement in sideways directions y and z is constrained requiring symmetry boundary conditions for the side surfaces of the bar. This prevents spurious movement and kinetic energy.

Non-linear geometry is neglected, as it is in the analytical solution. Including non-linear geometry effects gives a slightly softer result, as the plastic strain gradient η^p is calculated from the actual length instead of the initial length.

6.1.2 Results and discussion

Figure 6.2 show that the finite element solution matches the analytical solution very well except for close to the boundary. This is an artefact produced by Abaqus' plot smoothing. The plot has been extracted defining a path in Abaqus from $x = 0$ to $x = L$ in the centre of the bar. The finite element model has produced strain data for the integration point in the centre of each element. When asked for strain values not in the centre of elements, Abaqus calculates a

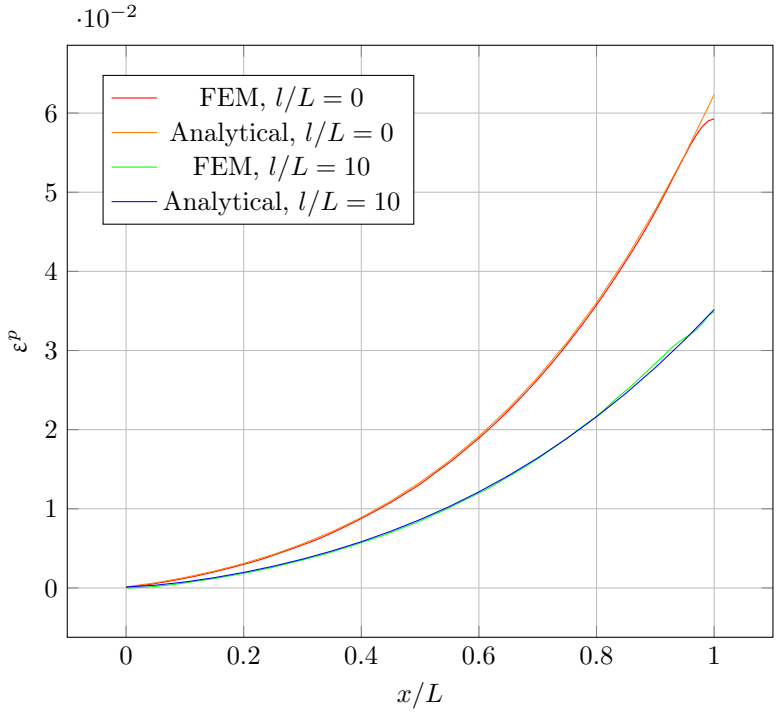

Figure 6.2: Bar loaded by gravity. $\eta^p = \eta^{p,C}$ has been used. The finite element mesh has 100 elements in the x-direction.

weighted average from surrounding integration points. For the top of the bar, there are no bordering elements to smooth with, and the strains are taken from the top element only, giving a dip in the curve.

The finite element implementation supports $\eta^p = \eta^{p,C}$, and the finite element solution in this chapter was compared to an analytical solution using the same measure. Overall results for this model are good, and support the correctness of the finite element implementation.

6.2 Shear of an infinite layer

This section analyses the thin layer in shear first discussed in Section 4.2. The initial distribution of plastic strains is prone to the numerical instability, later discussed in Chapter 7. 50 elements are used over the length D, $D/l = 50$; giving the stability requirement (developed in Section 7.3)

$$\begin{aligned} \frac{l}{l_e} &< 259 \\ l/D &< 259/50 = 5.17, \end{aligned} \tag{6.1}$$

and the problem is analysed with relative material length scale $l/D = 3$, which is within the stability limit.

6.2.1 Finite element model

The shear model is a single row of elements in the x_1-direction. Bending effects are suppressed prescribing $u_1 = 0$ in the whole model, as Mikkelsen did for his shear model [16]. The bending is loaded in the centre $x_1 = 0$ and constrained on the edge $u_2(x_1 = D) = 0$. This produces a pure shear state with constant shear $\sigma_{12}(x_1, x_2) = \tau$.

6.2.2 Results and discussion

The shear model shows more of a difference between the viscoplastic-like formulation and the yield surface formulation. This is visualized in Figure 6.3. Viscoplastic-like behaviour gives more flow in all parts of the model, and smooths out the difference between the part where there is little flow (left, $\sigma_e < \sigma_{flow}$) and the part with substantial flow (right, $\sigma_e \approx \sigma_{flow}$). The strain gradient effect is observed as a tiny dent in the FEM plots in the intersection where the flow starts, where the prescribed shear strain distribution provides some strain gradient hardening. This is a result of the finite element discretization. An ad-absurdum proof that this cannot be the case given a continuous, differentiable equivalent plastic strain. In the following, let x be the first axis, $x = x_1$.

1. Assume that there is a local minimum in the distribution of plastic strain for the given shear example. Denote this the "dent" of the strain field. Assume also that the plastic strain field is continuous and one time differentiable, and that the stress field is constant $\sigma_{ij}(x) = \sigma_{ij}$

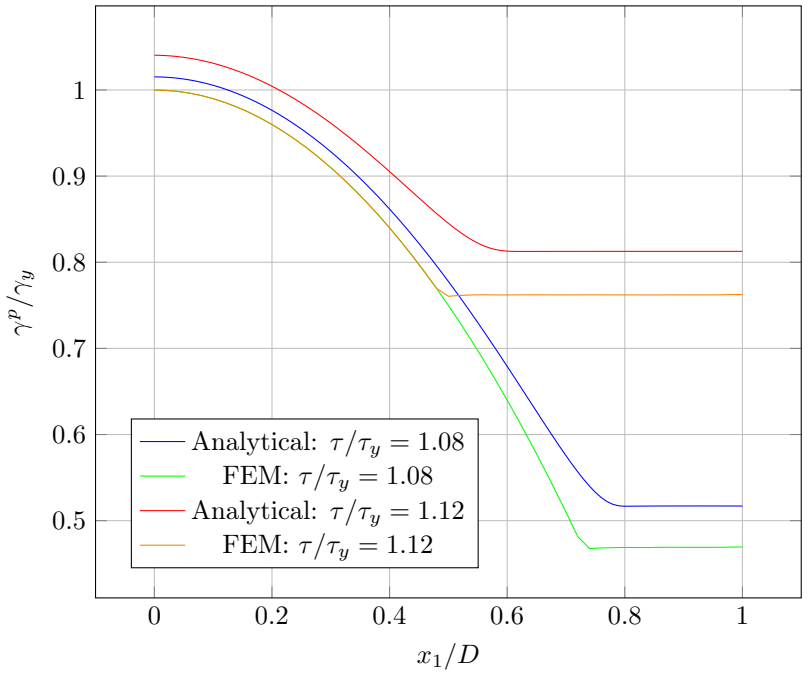

Figure 6.3: Comparison of selected analytical and numerical solutions: distribution of normalized engineering plastic shear strain for $l/D = 3$.

2. Since the plastic strain field is continuous and one time differentiable, there exists a place x_{dent} where the derivative of the plastic strain field is zero $\frac{\partial \varepsilon^p}{\partial x} = 0$

3. Since the plastic strain at the "dent", $\varepsilon^p(x)$, is a local minimum and the strain gradient is zero, it will be less hard $\sigma_{flow}(\varepsilon^p, \frac{\partial \varepsilon^p}{\partial x})$ than all its surroundings

4. When the stress is incremented, the plastic strain increment in the "dent" will therefore always be bigger than its surroundings, given that the stress causes a non-zero plastic strain increment $\Delta\varepsilon^p > 0$, and its strain increment $\Delta\varepsilon^p(x)$ will be larger than the strain increments of all its surroundings

5. "Dents" can therefore never grow in continuous strain gradient implemen-

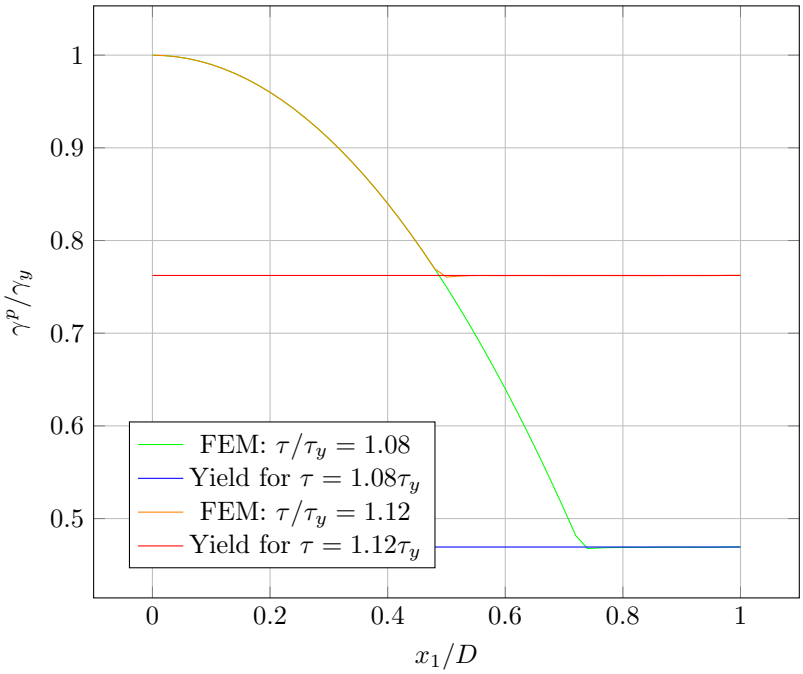

Figure 6.4: FEM solution compared to calculated plastic strain given prescribed stresses.

tations

As $x_1/D \to 1$, plastic strain from the FEM calculation converges to the plastic strains calculated directly from the loading.

γ^p is calculated from the hardening formulation

$$\frac{\tau}{\tau_y} = \frac{\sigma_{flow}}{\sigma_y} = \left(1 + \frac{\varepsilon^p}{\varepsilon^y}\right)^N = \left(1 + \frac{\gamma^p}{\gamma^y}\right)^N, \tag{6.2}$$

which inverted is

$$\frac{\gamma^p}{\gamma_y}(\tau) = \left(\frac{\tau}{\tau_y}\right)^{\frac{1}{N}} - 1. \tag{6.3}$$

For the prescribed shear stresses, the plastic strains become $\gamma^p(\tau = 1.08\ \tau_y) = 0.4693\ \gamma_y$ and $\gamma^p(\tau = 1.12\ \tau_y) = 0.7623\ \gamma_y$. As shown in Figure 6.4, the FEM

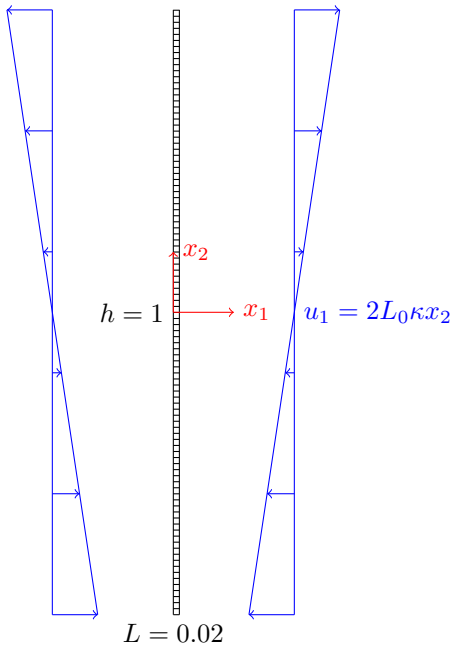

Figure 6.5: FEM mesh for bending model. Curvature is controlled using prescribed displacements. 100 elements are used.

model yields exactly where it should, and there is no yield before reaching the yield surface, as shown further left on the plot.

6.3 Thin beam bending

The thin beam in bending, previously handled in Section 4.3 is now examined using the finite element method. Controlling curvature, and thereby strains, suppresses the tower/canyon effect, which will be introduced in Section 7. Computing the plastic strain gradient from nodal averaging is shown to produce an anomaly in stress/strain distributions close to the boundary of the beam.

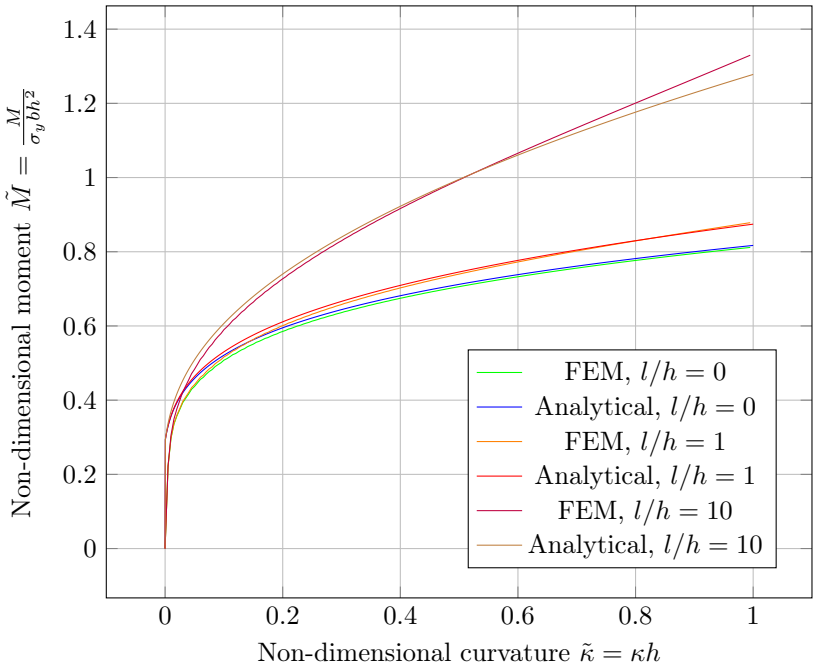

Figure 6.6: Bending of thin beams. Comparison between analytical and finite element solutions.

6.3.1 Finite element model

The finite element model is illustrated in Figure 6.5. A single row of elements is sufficient to produce the desired bending effect, where 2D plane strain elements (CPE4R) are used. The beam is constrained in x_2 in the two bottom elements, and strains in the x_1-direction are prescribed to simulate curvature. A thin beam is chosen so that large curvatures may be reproduced with minimal change in geometry. The beam has dimensions of $(L_1, L_2, L_3) = (L, h, d) = (0.01, 1.00, 1.00)$.

6.3.2 Results and discussion

Analysis results of the bending problem are represented in Figure 6.6. The correspondence is decent, but there are two notable differences.

1. Analytical response is stiffer for small curvatures

Table 6.1: Assumptions for analytical solution vs FEM solution for bending problem

Analytical solution	FEM solution
Elastic strains are neglected	Elastic strains are not neglected
Strain gradient calculated based on initial geometry	Strain gradient calculated based on deformed geometry
Otherwise linear geometry	Otherwise linear geometry

2. FEM response is stiffer for the combination of large curvatures and large material length scale l

These differences can be understood from different assumptions in the analytical solution and the FEM implementation, which are given in Table 6.1.

In the analytical solution, assuming $\varepsilon_{ij} \approx \varepsilon_{ij}^p$ allows for an explicit solution. This causes the analytical responses to immediately rise, with no elastic loading. The FEM solution, in contrast, first experiences elastic loading, shown by the initial linear response, before plastic strains start dominating.

For very large strains, when strain gradient effects are included, the FEM results are stiffer than the analytical results. This is caused by the fact that the strain gradient is calculated based on deformed geometry. It is noted that linear geometric analysis is chosen in this example for the sole purpose of comparing finite element solutions to analytical solutions.

When the curvature induces large strains, they notably deform the cross section. Since the beam is in plane strain, plastic strains in the y-direction are given from plastic strains in the x-direction as $\varepsilon_{22}^p = -\varepsilon_{11}^p$. Abaqus results were calculated using linear geometry and engineering strains. Kinematics give $\varepsilon_{11} = \kappa x_2$, resulting in $\varepsilon_{11} = 0.5$ and $\varepsilon_{22} = -0.5$ in $x_2/h = 0.5$ when $\kappa h = 1$. On other words, strains are completely linear, and are not a source for difference in results between analytical and finite element solutions.

The strain gradient in the finite element implementation, however, is calculated based on deformed geometry. Consequently, the strain gradient contribution in the top of the beam ($x_2 > 0$) is larger than in the bottom of the beam ($x_2 < 0$). This gives larger stresses in the top, and lower stresses in the bottom than if the strain gradient had been calculated based on initial geometry. Figure 6.7 illustrates that the stress distribution is antisymmetric, as expected, when there are no strain gradient effects ($l/h = 0$), and non-symmetric for large strain gradient effects ($l/h = 10$). Smaller strain gradient effects ($l/h = 1$), not shown

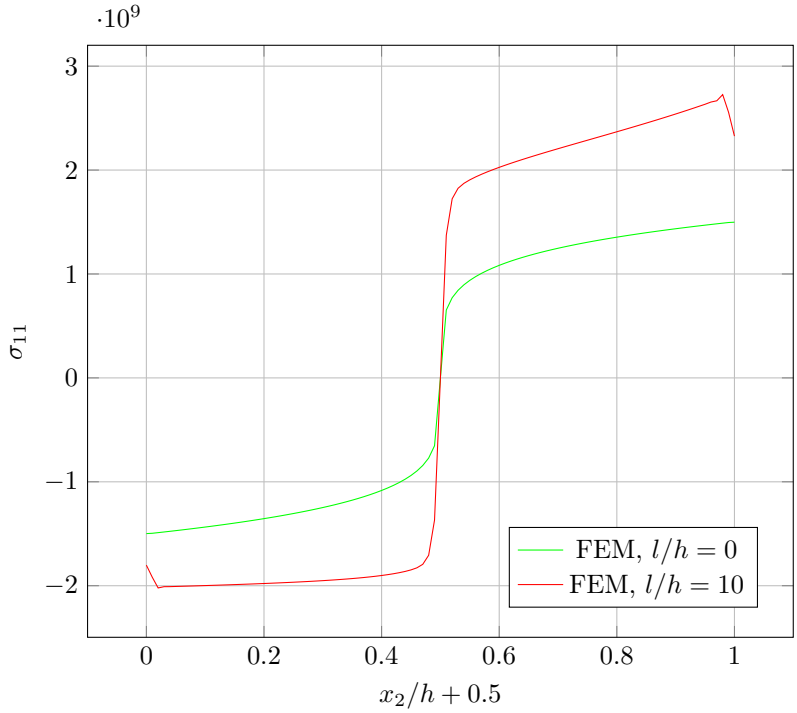

Figure 6.7: Finite element results for the thin beam in bending, when $\tilde{\kappa} = \kappa h = 1$. Difference in symmetry between strain gradient response ($l/h = 10$) and conventional response ($l/h = 0$).

here, shows the same trend. Hence, results will diverge when the curvature is increased further.

The overestimation of the plastic strain gradient in the top of the beam is larger than the underestimation of the strain gradient in the bottom of the beam. This can be understood looking at the calculation of the plastic strain gradient over an element. In the top of the beam ($x_2 = h/2$), the element length is cut in half $l'_{e,top} = (1 + \varepsilon_{22,top}) l_{e,top} = \frac{1}{2} l_{e,top}$. In the bottom of the beam, the element length is increased, but not doubled $l_{e,bot} l = (1 + \varepsilon_{22,bot}) l_{e,bot} = \frac{3}{2} l_{e,bot}$. The increase in strain gradient calculation is $\eta^p_{nonlin}/\eta^p_{lin} = l_e/l'_e$, increasing the calculated strain gradient in the upper part of the beam by a factor of 2, whereas the calculated strain gradient for the lower part of the beam is decreased, and

strain gradient calculated based on deformed geometry is 0.66 times the strain gradient calculated based on initial geometry. In addition, this effect produces axial forces, which are not corrected for. It is concluded that verification of the FEM solution using the analytical solution should be done where non-linear effects are negligible; where $\kappa h \ll 1$, and here the analytical solution corresponds well with the finite element solution.

Finally, the jagged ends of the stress distributions should be explained. The end elements, where $x_2 = -h/2$ and $x_2 = h/2$ gain less strength from the plastic strain gradient due to nodal averaging. The element on the edge where $x_2 = h/2$ is denoted e_1 and its neighbour e_2. e_1 is then the element on the edge, and e_2 the element second closest to the edge. The nodes on the top and bottom ends of the beam only gain plastic strain contribution from lumping of the end element. Therefore, using nodal averaging gives the plastic strain gradient over e_1 as half the correct value. This produces a significant reduction in strain gradient hardening, which is seen on the figure.

The tiny increase in capacity of e_2; the element next to the edge element, sees a slight increase in capacity. Every element has a prescribed total strain from the curvature of the beam. Its split into elastic and plastic strains $\varepsilon_{ij} = \varepsilon^e_{ij} + \varepsilon^p_{ij}$ depends on the material hardening. The elastic strain is derived from the total strain using the stress, as described in Equation 3.1: the higher the stress, the higher the elastic strain. When a large contribution to the material hardening comes from the strain gradient, for a prescribed total strain, a larger portion is elastic. Similarly, if there is little material strain gradient hardening, the portion of elastic strain is smaller. Therefore, e_1 has a larger portion of its total strain plastic then it would have had without the boundary effect. For element e_2, this causes an increased difference in plastic strain, which gives an increased plastic strain gradient, and increased material hardening. With increased material hardening, the stress is more than for an ideal, continuous model, and it is observed as a dent.

Understanding exactly why the finite element solution produces this defect is less important than the implications of the defect. Lower-order strain gradient plasticity theories have an advantage over higher order theories in simpler boundary conditions. However, they introduce possible defects, such as the one documented in the previous paragraph.

Chapter 7

Stability of numerical solutions

Stability challenges were first observed in the shear problem, using nodal averaged values of the equivalent plastic strain. Instabilities are strongly related to the ratio of the material length scale to the element length l/l_e. Large material length scale produces instabilities, and a coarse element mesh smooths out the response.

Section 7.1 introduces the instability phenomenon, before sections 7.2 and 7.3 give a theoretical explanation and a theoretical stability criterion. In Section 7.4, the developed theoretical stability criterion is tested against the instability data from Section 7.1. The reader is encouraged to review the figures in Section 7.1 after the theoretical foundation is in place, this time as an application of the theory, and not as the first time as an introduction to the stability phenomenon.

An alternative way of sampling the plastic strain gradient does not give the stability defects found in this chapter is given in Appendix A.

7.1 Evidence of instability

Instability was first encountered during work on Section 6.2, where an increased non-dimensional material length scale $l/D = 5$ was employed for an element mesh of 100 elements, which is plotted in Figure 7.1. In Figure 7.2, $l/D = 4$, and instabilities are slower to appear. All other parameters of the model are left unchanged.

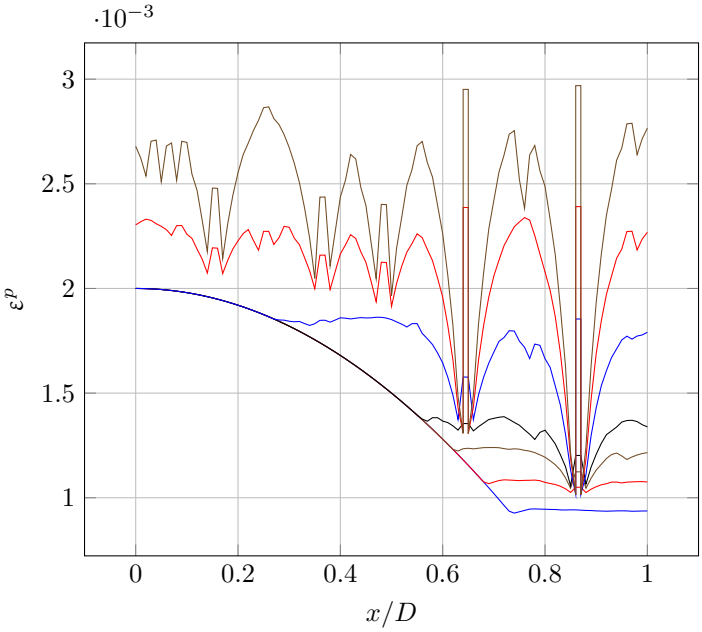

Figure 7.1: Instability evolution for the infinite shear layer. 100 elements are used, $l/D = 5$ and shear strains are incremented up to $\tau = 1.2\tau_y$, as in the verification in Section 6.2. Instabilities emerge at $\varepsilon^p = 0.0010 \approx \frac{1}{2}\varepsilon_y$ at $\tau = 1.09\tau_y$. Same colours for different plots is of no significance. Increasing stresses give increasing strains.

The defects across the layer are similar in shape. Denote local maximum at the centre a **tower**. On both sides of the tower, the local minima are **canyons**. Canyons are a more serious version of the defect encountered in Subsection 6.2.2, and the proof that the local minima of plastic strain are non-physical applies here.

Higher material length scale to element length l/l_e causes the instability to emerge earlier, and for $l/D \approx 8$, instabilities emerge at $\varepsilon^p = 0$. For $l/D = 4$, instabilities emerge at $\varepsilon^p \approx 1.1\varepsilon_y$, and $l/D = 2$ gives a stable response for stresses $\tau \leq 1.2\tau_y$.

The same test was conducted for a *randomly* pre-strained field, where instabilities for $l/D = 4$ were observed at $\varepsilon^p \approx \varepsilon_y$.

Instabilities can also be produced in the gravity example. Whereas in the shear example, the volume of the elements is left unchanged, as in the bending

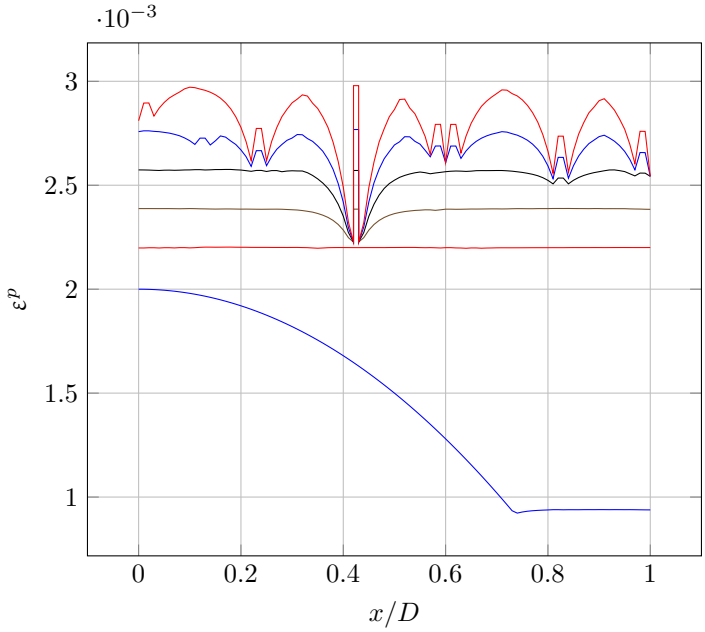

Figure 7.2: Instability evolution for the infinite shear layer. 100 elements are used, $l/D = 4$ and shear strains are incremented up to $\tau = 1.20\tau_y$, as in the verification in Section 6.2. Instabilities emerge at $\varepsilon^p \approx 1.10\varepsilon_y$, when loaded by $\tau = 1.16\tau_y$. Same colours for different plots is of no significance. Increasing stresses give increasing strains.

example, normal stresses cause volume change. The original gravity model, as investigated in Section 6.1, shows no instability. The reason is twofold.

1. The applied gravity load produces a monotonically increasing stress field, giving a monotonically increasing strain field

2. The model is in tension

The tower/canyon defect occurs as a larger value of plastic strain, the tower; surrounded by smaller values of plastic strain, the canyons. A monotonically increasing strain field never sets up these preconditions[1].

[1] Unless strain increments are very large.

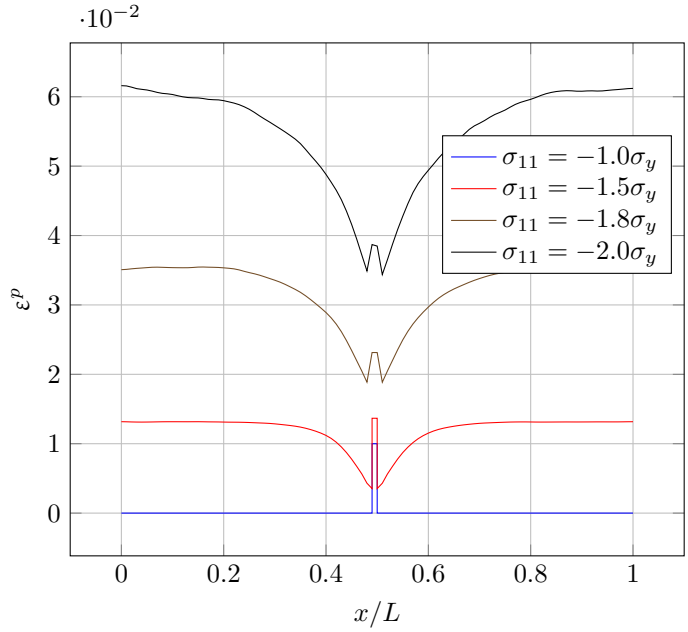

Figure 7.3: Instability of bar under constant compression, $l/L = 3$.

Tension produces the same effect as observed in the finite element analysis of the thin beam in bending: the elements *increase* in volume, reducing the strain gradient.

The following modifications are made to the bar gravity model to demonstrate instabilities:

- The gravity load is removed to allow for a non-monotonically increasing stress field
- The end tension is changed to compression and doubled in magnitude; $\sigma_{bottom} = -2\sigma_y$ (compression)
- A predefined plastic strain field is introduced to start the instabilities

Figure 7.3 shows the response for the modified bar gravity model. Compression, in contrast to shear, causes causes normal strains, which change element lengths. Large compression reduces the element length significantly, and amplifies strain

gradient effects. Compression also, however, gives a somewhat stabilizing effect. The largest strain gradient amplification is in elements where isotropic hardening dominates. Strain gradient hardening in elements where the strain gradient dominates is amplified less because of smaller normal strains.

It is also observed that in contrast to the shear example, both the local minima of equivalent plastic strains (later denoted canyons) and the central local maximum of equivalent plastic strain (later denoted tower) are flowing plastically. This does not mean that inhomogeneities are smoothed out; the parts of the bar with the most plastic strain ($x \approx 0$ and $x \approx L$) flow more than the central part experiencing instability ($x \approx L/2$), which does not catch up. This gives a good foundation for why Niordson and Hutchinson would choose a shear example for their stability criticism of lower order strain gradient plasticity theories [18].

In contrast to the shear example, no new instabilities arise across the bar. Testing with the predefined field of the shear example did not give rise to instabilities for the bar.

The beam bending problem is incremented by prescribing displacements; total strains $\varepsilon_{ij} = \varepsilon^e_{ij} + \varepsilon^p_{ij}$ are given. When the total strain is given, there is little room for the plastic strain to destabilize. Bad behaviour is still observed in a thin layer close to the boundary, as discussed in Subsection 6.3.2.

For both instability examples presented, kinetic energy is very small compared to the strain energy, $E_k < E_s \times 10^{-3}$, thus dynamic effects are negligible.

Following is a summary of the phenomena observed in this section.

- The cause of the instability is that an element may harden more from *not* flowing plastically than flowing
- The rise in hardening of the element where there is no equivalent plastic strain increment, $\dot{\varepsilon}^p = 0$, is more than the rise in hardening of surrounding elements, where there is a positive equivalent plastic strain increment $\dot{\varepsilon}^p > 0$
- For the current strain gradient plasticity model, strain gradient hardening becomes more important relative to the equivalent plastic strain hardening as strains increase. This is generally the case, as the hardening modulus $h(\varepsilon^p) = \frac{\mathrm{d}\sigma_{flow}}{\mathrm{d}\varepsilon^p}$ generally decreases as plastic strains increase
- In uniform stress $\sigma_e(x, y, z)$, there should be no local minima or maxima of the equivalent plastic strain field $\varepsilon^p(x, y, z)$. Inaccuracy in effective plastic strain gradient η^p calculation may allow local minima or maxima to develop

- For very large material length scales and a given element mesh, instability occurs before there is *any* increase in plastic strain
- Otherwise, instabilities may occur further "down the road", as strain gradient hardening becomes more important relative to isotropic hardening. Plastic strain gradient hardening increases proportional to the root of the strain gradient. For the chosen power law, where $N = 0.2$, plastic strain hardening increases proportional to the rise of plastic strain raised to a power of 0.2, which is less than 0.5
- Instabilities may be prevented by enforcing a monotonically increasing plastic strain. If the "natural" increase in plastic strain is enforced, such as in the bar in tension from Section 4.1, instabilities may be suppressed.
- The stability phenomenon may be described analytically by comparing contributions to hardening from equivalent plastic strain ε^p to hardening contributions from the effective plastic strain gradient η^p
- Very large strains may cause significant changes to the plastic strain gradient. Compressing elements decreases the element length, and the gradient increases. If an element is in tension, the length increases, and the gradient decreases

7.2 The tower/canyon defect

In the previous section, the defects witnessed in the shear of an infinite layer model were denoted towers and canyons. Why these defects arise is explained in this section.

Figure 7.4 demonstrates the plastic strain distribution for a fully developed tower/canyon defect. This plot is partially smoothed, as the ones outputted by Abaqus[2]. A non-smoothed example is given in Figure 7.5. Uniform equivalent stress $\frac{\partial \sigma_e}{\partial x_i} = 0$ and zero normal strains $\varepsilon_{11} = \varepsilon_{22} = \varepsilon_{33} = 0$ are relevant properties of the infinite shear layer model, which are not fulfilled for neither the

[2] In reality, the strain distribution is jagged, because of the use of lower order elements, and the strains are most accurate in integration points within the element. However, when plotting strain data over a path, Abaqus outputs strain data in nodes. If the strains in the surrounding elements are similar, an average value is taken. Otherwise, both values of the strain are outputted for the same coordinate. The strain discontinuity around the tower element is large, giving vertical lines in the equivalent plastic strain distribution in Figure 7.4 around the "tower".

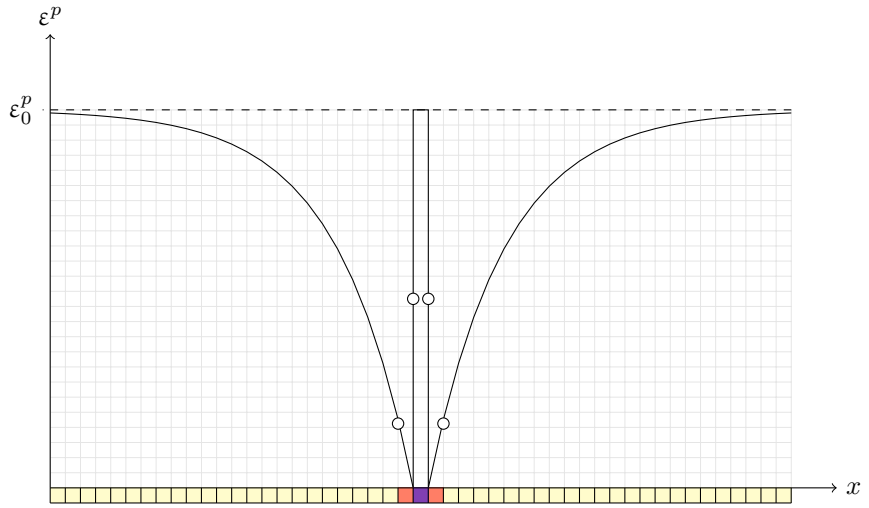

Figure 7.4: The tower/canyon effect illustrated for a one-dimensional model with length coordinate x, constant equivalent stress $\sigma_e = \sigma_0$ from pure shear, therefore zero normal strains $\varepsilon_{11} = \varepsilon_{22} = \varepsilon_{33} = 0$. Element mesh is yellow. The tower element is purple, canyon elements are orange. Nodal averaged values of the equivalent plastic strain ε^p are circles ○. Fundamental for this stability criterion is that a constant stress field may produce a non-constant strain field, even when strain boundary conditions encourage a constant strain field.

uniaxial stress model in Section 4.1 nor the bending model in Section 4.3. With a monotonically increasing equivalent stress, the tower/canyon defect would be avoided, as discussed in Section 7.1. Zero normal strains prevent change of element size, which affects the strain gradient effect: compression increases the strain gradient, whereas tension decreases the strain gradient effect.

The largest witnessed plastic strain is $\varepsilon^p = \varepsilon_0^p$, the dashed line in Figure 7.4. The tower has two equal nodal averaged equivalent plastic strain values, thus no strain gradient effect $\eta_t^p = 0$. The plastic strain of the tower must therefore be $\varepsilon_t^p = \varepsilon_0^p$. The canyon, on the other hand, has zero equivalent plastic strain in its integration point $\varepsilon_c^p = 0$, and large variation of plastic strain between its nodal averaged values, and therefore a large effective plastic strain gradient $\eta^p > 0$.

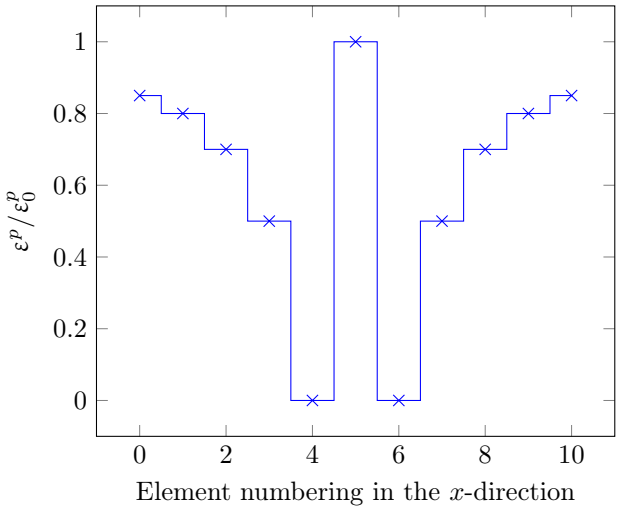

Figure 7.5: Actual non-smoothed strain distribution to illustrate the tower/canyon effect. Element 5 is the tower element, and elements 4 and 6 are canyon elements. Strain data lumped from integration points, marked $\times$, to the whole element. Magnitudes are chosen arbitrarily to illustrate the tower/canyon effect. The tower has a large strain in the integration point $\varepsilon_t^p = \varepsilon_0^p$, whereas the canyons have no plastic strain $\varepsilon_c^p = 0$. Elements far from the tower have equivalent plastic strain $\varepsilon^p \approx \varepsilon_0^p$.

7.3 Stability criterion

This section develops a stable material length scale based on the tower/canyon defect documented in Section 7.2.

Assume a uniform equivalent stress σ_e, which should develop a uniform equivalent plastic strain ε^p, therefore zero strain gradient $\eta^p = 0$. Assume further a fully developed tower/canyon defect: the tower has a large equivalent plastic strain $\varepsilon_t^p = \varepsilon_0^p$, and the canyon has no equivalent plastic strain $\varepsilon_c^p = 0$. The case is assumed to be one-dimensional, with variation in the x-direction, giving the expression for the effective plastic strain gradient used in the finite element implementation as $\eta^p = \eta^{p,C} = \left|\frac{\partial \varepsilon^p}{\partial x}\right|$.

Denote normalized hardening for the tower $f_t = \frac{\sigma_{flow}}{\sigma_y}$ and normalized hardening for the canyon $f_c = \frac{\sigma_{flow}}{\sigma_y}$, where uniform equivalent stress and plastic yield implies constant flow stress $\sigma_{flow} = \sigma_e$. A stable response is guaranteed

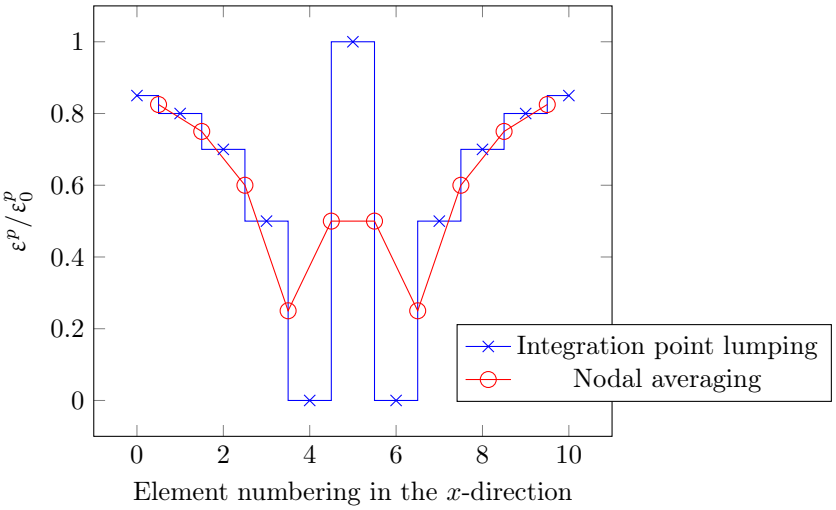

Figure 7.6: Comparison of strain field based on lumping of integration point data to the element (integration point equivalent plastic strain values marked $\times$, as in Figure 7.5) and strain field based on linear interpolation between nodal average values (nodal averaged values marked $\circ$).

when a prescribed tower/canyon distribution smooths out. For the tower/-canyon defect to smooth out, the canyons must be filled. This happens when tower hardening is larger than the canyon hardening, giving the stability criterion

$$f_t > f_c. \tag{7.1}$$

For strain gradient calculation, nodal averaging is used. Strain fields based on integration point lumping and nodal averaging are visualized in Figure 7.6. The nodal averaged value of the equivalent plastic strain between the canyon and the tower is $\varepsilon^p_{tc} = \frac{\varepsilon^p_0+0}{2} = \frac{1}{2}\varepsilon^p_0$. The canyon element has two neighbour element, the tower element and another element with small plastic strain. The nodal averaged value of the canyon element and its non-tower neighbour is therefore small, but non-negative, $\varepsilon^p_{cc} > 0$.

This gives the effective plastic strain gradient of the tower calculated based on its nodal values $\eta^p_t = |\frac{\varepsilon^p_{tc}-\varepsilon^p_{tc}}{\Delta x}| = 0$, and a bound for the effective plastic strain gradient of the canyon $\eta^p_c = |\frac{\varepsilon^p_{tc}-\varepsilon^p_{cc}}{\Delta x}| < |\frac{\frac{1}{2}\varepsilon^p_0-0}{\Delta x}| = \frac{\varepsilon^p_0}{2\Delta x}$, as the equivalent plastic strain is positive $\varepsilon^p_0 > 0$ and the length difference is assumed positive $\Delta x > 0$.

Inserting the equivalent plastic strain and the effective plastic strain gradient into the material hardening formulation gives

$$f_t = \left(1 + \frac{\varepsilon_0^p}{\varepsilon_y}\right)^N \tag{7.2a}$$

$$f_c < \sqrt{1 + l\frac{1}{2}\frac{\varepsilon_0^p}{\Delta x}}. \tag{7.2b}$$

Inserting equations 7.2 into the inequality of Equation 7.1 gives the inequality

$$\left(1 + \frac{\varepsilon_0^p}{\varepsilon_y}\right)^N > \sqrt{1 + l\frac{1}{2}\frac{\varepsilon_0^p}{\Delta x}}. \tag{7.3}$$

Equation 7.2 *does not imply* Equation 7.3! On the other hand, Equation 7.3 implies Equation 7.2. Equation 7.2 is a tighter bound than the actual stability limit. Stability conditions derived from the tighter bound are valid, even though they give more restrictive conditions than the exact limit. Requiring Equation 7.3 for all elements gives the global bound on the smallest element with element length $\Delta x = l_e$, and solving for the material length scale gives the stability requirement

$$l < l_c \quad \text{where} \quad \frac{l_c}{l_e} = \frac{2}{\varepsilon_0^p}\left[\left(1 + \frac{\varepsilon_0^p}{\varepsilon_y}\right)^{2N} - 1\right], \tag{7.4}$$

and l_c is denoted the critical material length scale[3]. Note that this stability criterion is too tight, with two causes:

1. The problem is assumed stable when it can *recover* from instability. Simulations show that certain preconditions, certain randomness is required for this to be the case[4], and the requirement is in general too tight

2. Inaccuracy based on the inequality of Equation 7.2b

Concluding, the stability criterion *guarantees* stability; it is conservative.

[3] As the material length scale is given in real life applications, a more physical stability limit would be the critical element length. However, when modelling strain gradient effects, modifying the material length scale l is a simpler way of accounting for length scale changes than changing the entire model. Therefore, the stability limit is imposed on the material length scale.

[4] The discussion of the bar problem in Section 7.1 provides evidence that randomness or certain preconditions may be necessary to initiate the instability.

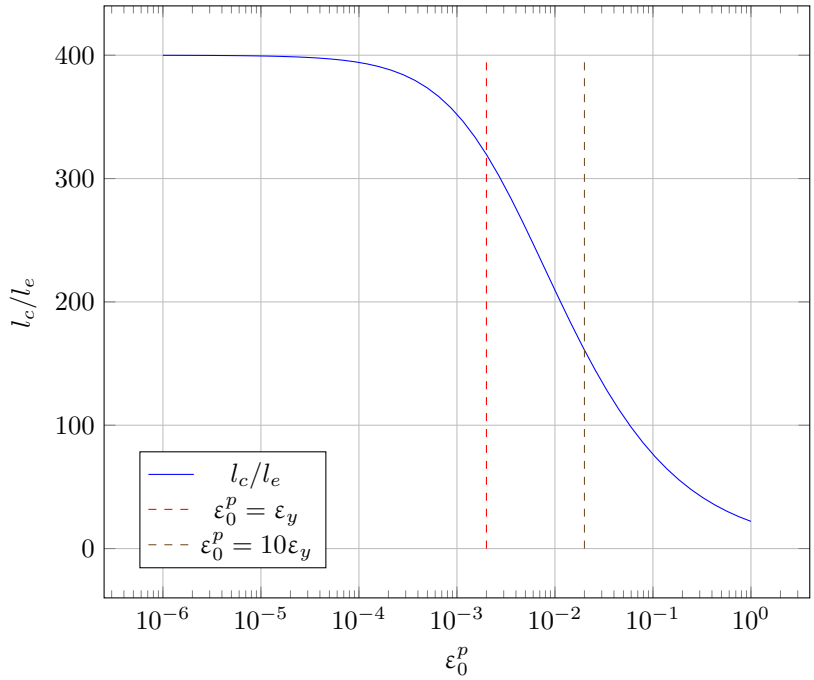

Figure 7.7: Stable material length scale as a function of plastic strain increment. Material parameters are as in previous problems $\varepsilon_y = 0.002$ and $N = 0.2$. For $\varepsilon_0^p \ll \varepsilon_y = 2 \times 10^{-3}$, $l_c/l_e \approx 400$. Note the logarithmic x-axis. The dashed red line marks $\varepsilon_0^p = \varepsilon_y$.

7.4 Stability criterion verification

This section will apply the stability criterion developed in Section 7.3 to the finite element model that produced the strongest instability to check its validity.

The stability criterion in Equation 7.4 depends on the plastic strain that gives equilibrium with external stresses without any strain gradient hardening ε_0^p. Figure 7.7 plots this limit for the material parameters used throughout this thesis ($\varepsilon_y = 0.002$, $N = 0.2$).

The stability criterion is then applied to the unstable shear responses in figures 7.1 and 7.2. In the first case, yielding occurs at $\varepsilon_0^p = 0.5\varepsilon_y$. The critical material length becomes $l_c/l_e = 352$, and for a 100 element mesh, $l_c/D = 3.52$.

The prescribed material length scale is over this limit $l/D = 5$. As expected, the criterion is conservative, and instability occurs after passing the stability limit.

In the second case, $\varepsilon_0^p = 1.1\varepsilon_y$, giving $l_c/l_e = 314$ and $l_c/D = 3.14$[5] Response for $l/D = 4$, which exceeds the stability limit, is known to produce instabilities, and the stability criterion is conservative.

[5]No relation to famous number of approximately equal magnitude.

Chapter 8

Case study

In this chapter, the developed strain gradient plasticity implementation is applied to selected problems: cylindrical particle strengthening and cylindrical material void growth. Huang et al. also studied void growth [13], but applied stresses radially. In this thesis, end displacements are prescribed. If the model had consisted of a single material, and not have a void or particle, the result would be uniaxial tension. Results from this chapter are thus not directly comparable to results by Huang et al., where tension is radial.

The developed strain gradient plasticity implementation differs from traditional plasticity theory in its length scale. For traditional plasticity, scaling the length up and down yields zero difference, which is not the case for strain gradient plasticity theories. Length scaling in the implemented strain gradient plasticity theory can be done in two ways. First, the intuitive way, is to scale the size of the model, and keep the material parameters constant. This approach makes the most sense physically: if small-scale phenomena are to be modelled, small models are used. l is a material parameter, and cannot just be changed: size effects are because of changes in size of the physical problem or model. The material parameters include the characteristic length scale l, and when l changes relative to model size, previously l/L, l/D or l/h, strain gradient effects are scaled.

The other way of observing size effects is modifying the characteristic length scale l directly, which is the method used in this chapter. Assuming l to be a single micron $l = 1\,\mu\text{m}$[1], the size of the model can be calculated. For the

[1] Huang et al. [13] found l to be "on the order of microns", $l \in [1\,\mu\text{m}, 10\,\mu\text{m}]$.

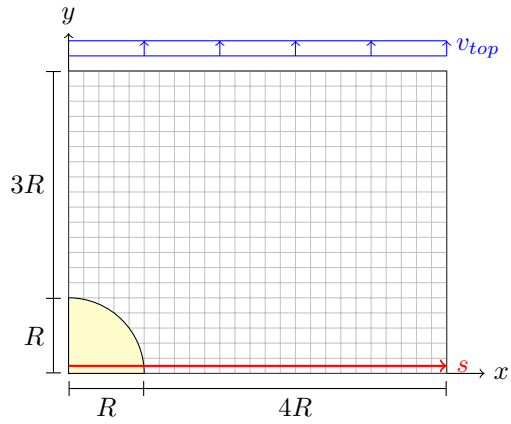

Figure 8.1: Finite element model used for analysis of particle (yellow) strengthening and void growth. Mesh is approximate, see output from Abaqus for accurate mesh close to the particle/void. Element size $l_e \approx R/5$. In the finite element model, $R = 5$ and $l_e \approx 1$. $s \in [0, 25]$ is the length coordinate on the red path, along which stresses and strains are later plotted.

particle strengthening in Section 8.1 and the void growth in Section 8.2, the initial particle radius or the initial void radius from $R = 5\,\mu\text{m}$ ($l/R = 0.2$) to $R = 0.1\,\mu\text{m}$ ($l/R = 10$). In other words—the larger material length scale with respect to model size, the smaller the model.

8.1 Particle strengthening

Figure 8.1 shows the finite element model used for the case of particle strengthening. The particle is purely elastic steel,

$$E_{particle} = 210\,\text{GPa}$$
$$\nu_{particle} = 0.3$$

whereas the matrix is strain gradient sensitive aluminium alloy,

$$\begin{aligned} E_{matrix} &= 70\,\text{GPa} \\ \sigma_y &= 420\,\text{MPa} \\ \nu_{matrix} &= 0.3 \\ N &= 0.2, \end{aligned}$$

which gives the yield strain $\varepsilon_y = (420\,\text{MPa})/(70\,000\,\text{MPa}) = 0.006$, larger than the material used in analytical solutions in Chapter 4 and by Huang et al.

The particle is modelled as a cylinder, and occupies a fraction

$$\frac{\pi R^2/4}{4R \times 5R} = 3.92\ \%$$

of the volume. Displacement in y-direction of the top edge v_{top} is prescribed. Bottom and right edges are pinned, $v_{bottom} = u_{left} = 0$. The right edge is allowed to move freely.

8.1.1 Unconditionally stable results

The top displacement is now prescribed, and incremented in the range of $v_{top} \in [0, R/5]$. Without strain gradient effects, the largest equivalent plastic strains observed are $\varepsilon_0^p = 0.073$, which inserted into the stability limit, Equation 7.4, gives the the critical material length scale $l_c/l_e = 49.5$. Increasing the material length scale smooths out the equivalent plastic strain distribution, and running the analysis with $l/l_e = 50$, the maximum equivalent plastic strain is $\varepsilon_0^p = 0.067$, for which the critical material time scale is $l_c/l_e = 51.24$. Choosing the element length as in Figure 8.1, the relative critical material length scale becomes

$$\begin{aligned} \frac{l_c}{R} &= \frac{l_c}{l_e} \times \frac{l_e}{R} \\ &= 51.24 \times 0.2 = 10.25, \end{aligned}$$

and choosing $l/R < 10.25$ will never produce the tower/canyon defect for the given element mesh. As expected, no instabilities are observed when $l/R \leq 10$.

Figure 8.2 gives the equivalent plastic strain field without strain gradient effects, and Figure 8.3 shows the equivalent plastic strain field with large strain gradient effects. Introducing strain gradient effects reduces the maximum equivalent plastic strain and smooths the equivalent plastic strain field, as is expected [16]. The plot also helps understand how the strain gradient effect increases the particle-matrix interaction. The simulation without strain gradient

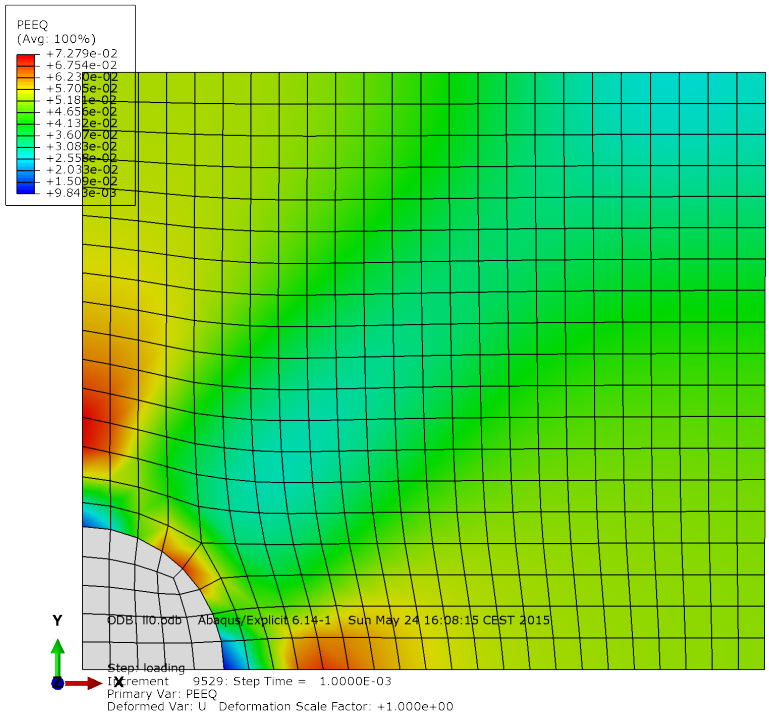

Figure 8.2: Particle strengthening. Equivalent plastic strain field. $l/R = 0$.

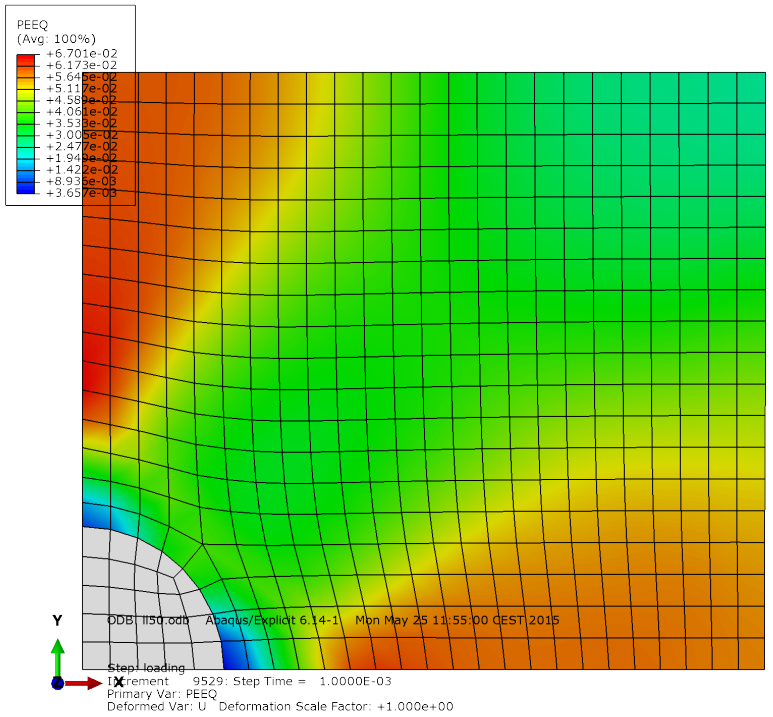

Figure 8.3: Particle strengthening. Equivalent plastic strain field. $l/R = 10$.

Table 8.1: True stress increase of particle model depending on length scale where the particles occupy 3.92 % of the total volume

l/R	Force increase (%)
0.0	0.000
0.2	0.067
2.0	0.600
5.0	1.438
10.0	2.873

effects shows a local maximum of equivalent plastic strain around coordinates $(X, Y) = (0, 1.6R)$. Including strain gradient effects increases the hardening of this region additionally, causing a redistribution of load to softer regions.

Figure 8.4 shows the true strain-true stress curve for different length scales. Increases in force applied to the top boundary from decreases in length scale are presented in Table 8.1. Plastic strain distribution over the coordinate s (the bottom row of elements parallel to the x-axis) is plotted in Figure 8.5, and shows smoothing of the plastic strain distribution. The stiffening provided by strain gradient effects gives better interaction between the particle and the matrix, and particle normal stresses increase notably (Figure 8.6).

The strain gradient contribution to the hardening of the model is small, which is expected when the particle occupies a small fraction of the total volume. Decreasing the particle radius R (or equivalently, increasing material length scale l) gives additional hardening, which is expected.

8.1.2 Beyond unconditional stability

Even smaller length scales have been examined for instabilities. This model is dominated by tension, stabilizing the model, for which an argument is given in Section 7.1. However, the argument from Section 7.1 is based on a one-dimensional model. Two-dimensional models are not expected to yield the same defects.

Non-smoothed results for a sub-micron length scale are shown in Figure 8.7. This is far past the stability limit, yet no tower/canyon defects are observed. The tower/canyon defect is based on a two-dimensional derivation. Contributions to the canyon stiffness from the strain gradient is lower in a three-dimensional unstable field. More elements with lower equivalent plastic strains contribute to

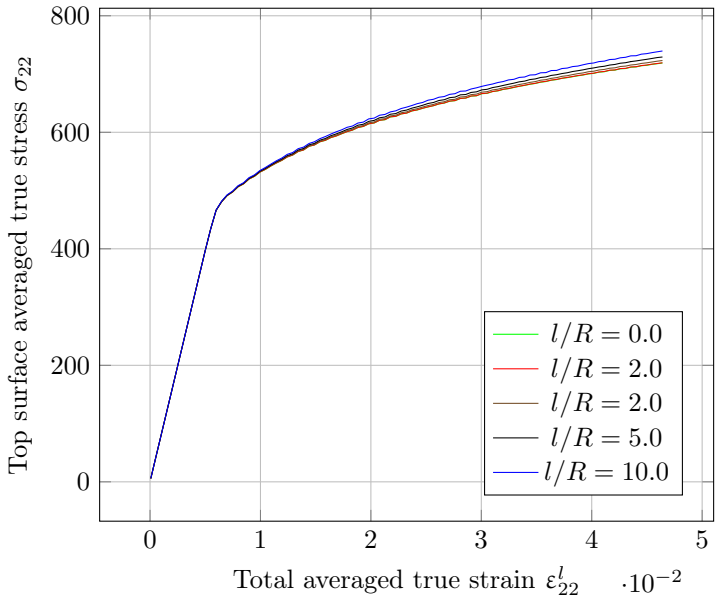

Figure 8.4: Particle. True stress-true strain curve. $l/R \in [0, 10]$.

an overall lower equivalent plastic strain in nodal points, canyon elements receive significantly less hardening than in the one-dimensional case. This is explained by the fact that they get their strain gradient stiffness from the neighbouring tower, and nodal strains surrounding the tower are now averaged from more neighbouring elements. Random- or unstable preconditions for the instability as was required for instability the uniaxial bar in compression are neither present.

True stress-strain curve on the top surface[2] for $l/R = 100$ is given in Figure 8.8. Further hardening is observed, as is expected. Kinetic energy is negligible compared to strain energy, $E_k < 10^{-3}E_s$. The observed jaggedness of the curve is due to explicit time integration. Increasing the strain gradient hardening contribution causes jaggedness to increase hardening, even though the tower/-canyon defect never develops. Using smaller increments helps avoids this. The

[2] The bottom is more interesting with respect to necking stress. Elements in the bottom of the beam are, however, more distorted, and the resulting averaged stress would be less accurate unless it took element distortion into account. For analysis of strain gradient effects, stresses from the top surface suffice.

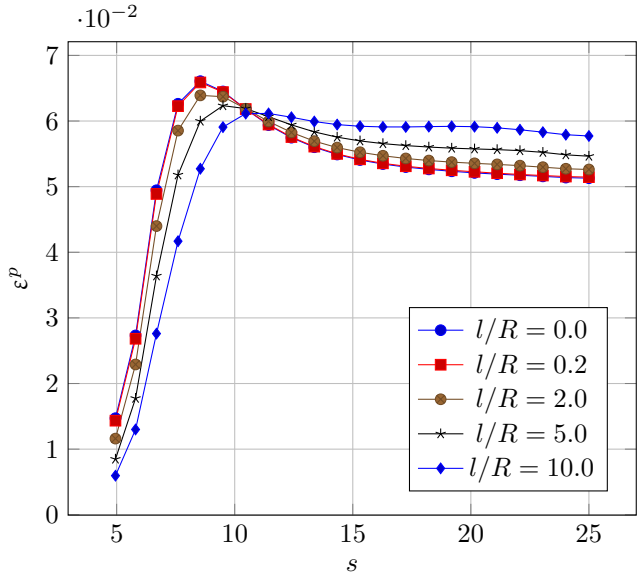

Figure 8.5: Particle strengthening. Plastic strain over the matrix with varying length scale l.

case is similar for the analytical solutions (Chapter 4). The tower/canyon stability criterion is too conservative in this regard, as it considers *recovery* of defects, and not their emergence, which is step-size dependent.

The purpose of this subsection is to illustrate potential consequences of crossing the stability limit. It does, however, also illustrate the increased particle-matrix interaction. Compare the equivalent plastic strain distribution of Figure 8.7 ($l/R = 100$) to figures 8.3 ($l/R = 10$) and 8.2 ($l/R = 0$). Increasing the strain gradient contribution pushes the plastic strains up from the particle, and the result is a high-stress region connecting the particle to the top surface.

Pushing the length scale even further, a two-dimensional occurrence of the tower/canyon defect is found. Observe in Figure 8.9 elements in the top-right corner of the model with virtually no plastic strain. These are analogous to canyons. Due to significant strain gradient hardening, they do not flow as the surrounding elements.

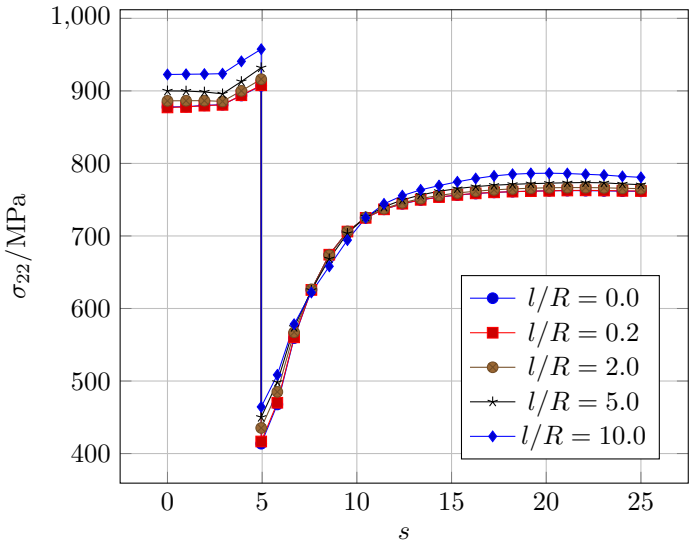

Figure 8.6: Particle strengthening. Normal stress over the matrix with varying length scale l.

8.2 Void growth

A central part of fracture mechanics is void growth. Experiments have shown that void growth is size-dependent; the smaller the void, the slower the void growth. Applying strain gradient plasticity theories to void growth has given good results for voids of order microns. Sub-micron length scales exhibit even more hardening than predicted by strain gradient theories, and is outside the scope of the strain gradient theory this thesis is based on work done by Huang et al. [13].

Void growth is simulated using the same model as for the particle strengthening model, where the void is modelled as a particle with negligible stiffness

$$E_{void} = 0.1\,\text{MPa}$$
$$\nu_{void} = 0.3,$$

and the geometry is the same as in Section 8.1, so that the void covers what used to be the particle.

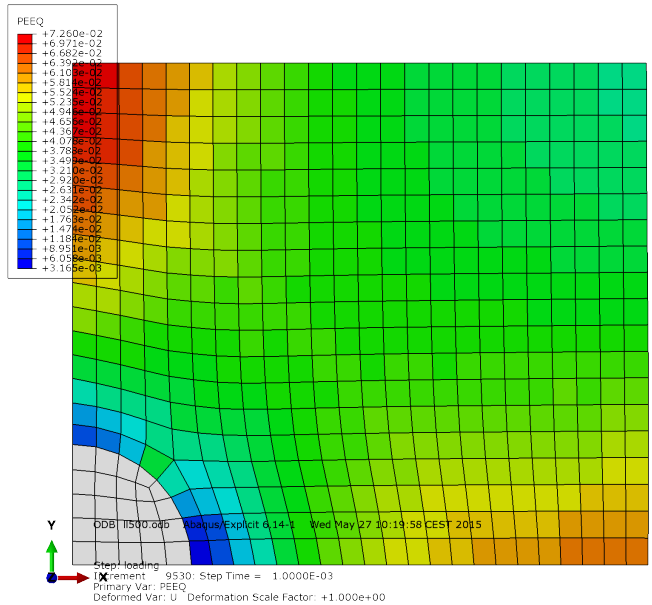

Figure 8.7: Particle strengthening. Non-smoothed equivalent plastic strain field. $l/R = 100$.

Simulating void growth with reasonable accuracy within limits of unconditional stability is not feasible with the current theory and model. Prescribing the top displacements as in the particle model in the range $v_{top} \in [0, R/5]$ yields a maximum plastic strain $\varepsilon_0^p = 0.242$ when $l/R = 0$ and 0.185 when $l/R = 10$. Inserting the smallest strain (non-conservative) into the stability limit of Equation 7.3 gives a critical relative material length $l_c/l_e = 32$. With the current mesh $R = 5l_e$, and

$$\begin{aligned} \frac{l_c}{R} &= \frac{l_c}{l_e} * \frac{l_e}{R} \\ &= 32 * \frac{1}{5} = 6.5. \end{aligned}$$

In addition, void growth is more interesting with significant changes in void volume. For the above model, volumes increased with $\varepsilon_V = 15.8\%$ ($l/R = 0$) or

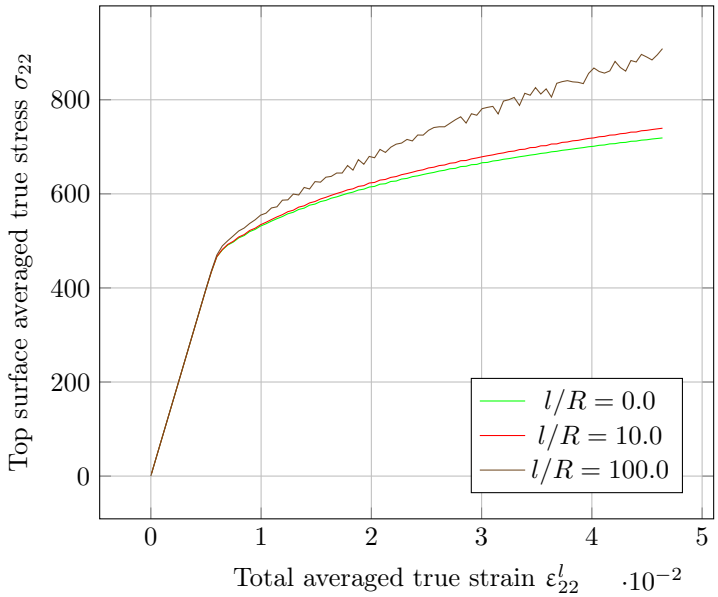

Figure 8.8: Particle strengthening. True stress-true strain curve. $l/R \in [0, 100]$.

$\varepsilon_V = 11.4\%$ ($l/R = 10$), and effects of larger changes in volume size are subject for investigation.

Figure 8.10 shows void growth as a function of average true strain in the displaced direction ε^l_{22}. Plastic, non-volumetric deformation dominates the matrix, giving the volume fraction f is approximately linearly dependent on the relative volume change

$$\begin{aligned} f &= \frac{V_{void}}{V_{tot}} = \frac{V_{void}}{V_{void} + V_{matrix}} \\ &\approx \frac{V_{void}}{V_{matrix}} = \frac{V_{void,0}}{V_{matrix}} \frac{V_{void}}{V_{void,0}} = \frac{\pi R^2/4}{4R \times 5R - \pi R^2/4} \frac{V_{void}}{V_{void,0}}. \end{aligned}$$

Given prescribed displacements, the strain gradient implementation predicts smaller relative void growth for smaller voids, which is consistent with physical observations and expectations for strain gradient theories.

Prescribed displacements are however only one side of the case. Small scale analysis $l/R = 2$ also produces significantly larger stresses. This is shown in

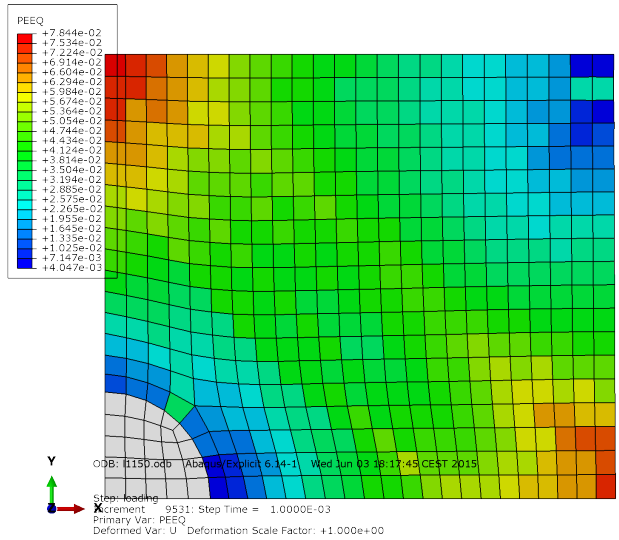

Figure 8.9: Particle strengthening. Equivalent plastic strain field. $l/R = 230$.

Figure 8.11. The effect of larger stresses per volume growth and larger volume growth per prescribed displacement leads to necking for the large scale model ($l/R = 0$) long before the small scale model ($l/R = 2$), and combining the data from figures 8.10 and 8.11, Figure 8.12 is obtained.

Maximum equivalent strains (for $l/R = 2.0$) are $\varepsilon_0^p = 1.137$, giving a stability limit of $l_c/l_e = 12.6$. Severely distorted element lengths give the minimum element to void radius ratio $l_e/R = 0.0544$, and relative critical length $l_c/R = 0.685$. This severe distortion is localized, and decreases monotonically in all directions away from the localization. No instability defects were observed.

When using large strains in the void model, some remarks must be made. First, the void volume is calculated under the assumption that the void stays ellipse-shaped, so that the change of volume can be described form the horizontal displacement of the left part of the void, and the vertical displacement of the top of the void. The assumption is accurate up to $V_{void}/V_{void,0} \approx 2$. For larger displacements, the edge of the void becomes straighter, and the ellipse-assumption over-estimates the volume change. Second, elements close to the left side of the volume are severely distorted, reducing their performance [3].

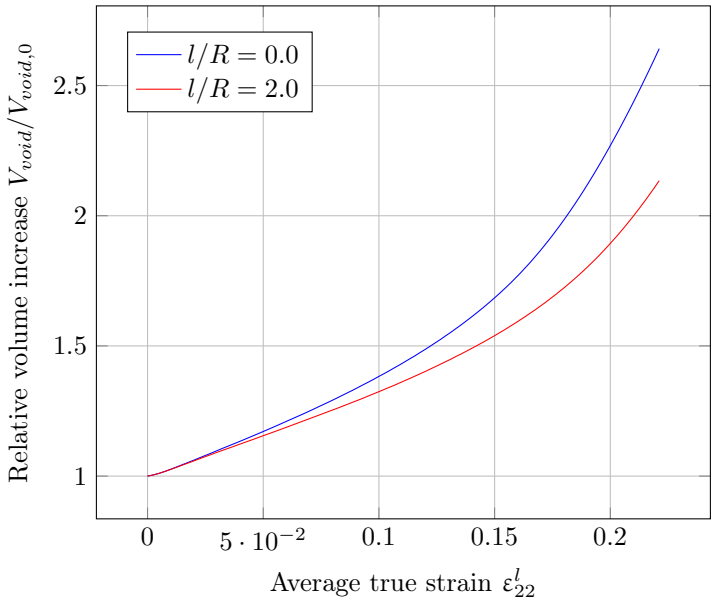

Figure 8.10: Void growth. Relative void volume increase vs. average logarithmic strain.

Figure 8.13 shows the large scale model ($l/R = 0$) with large element distortion. The small scale model ($l/R = 2$) shows less distortion for the same prescribed displacements, shown in Figure 8.14. Note also the increased stress values right of the particle, $(X, Y) \approx (0, 1.1R)$, and higher overall stresses.

Void growth shows significantly larger increase in hardening than particle strengthening. Under particle strengthening, perfect compatibility between the particle and the matrix results in small strains around the particle, seen in equivalent plastic strain plots. This is not the case with void growth. The void boundary is strained the most and has the largest strain gradients.

It is later shown that nodal averaging underestimates the strain gradient for the boundary elements. Comparing void growth when using nodal averaging to use of higher-order theories or by use of the method outlined in Appendix A would be interesting.

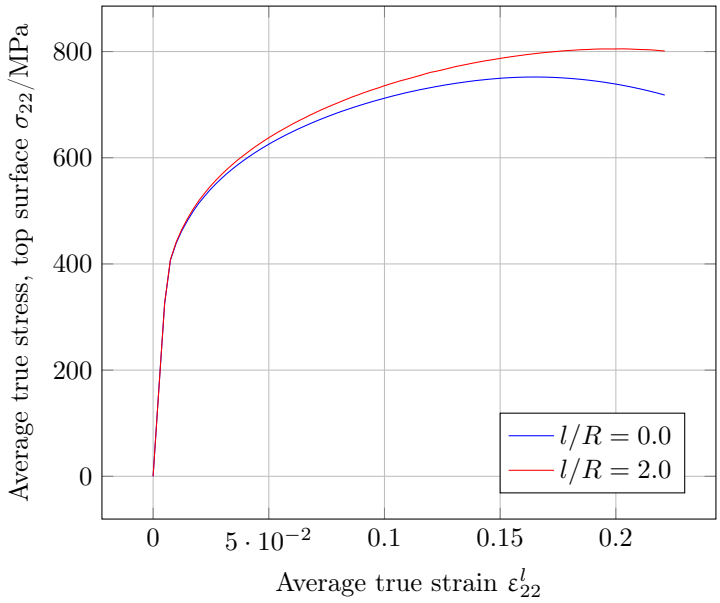

Figure 8.11: Void growth. Top surface average true strain vs. average logarithmic strain.

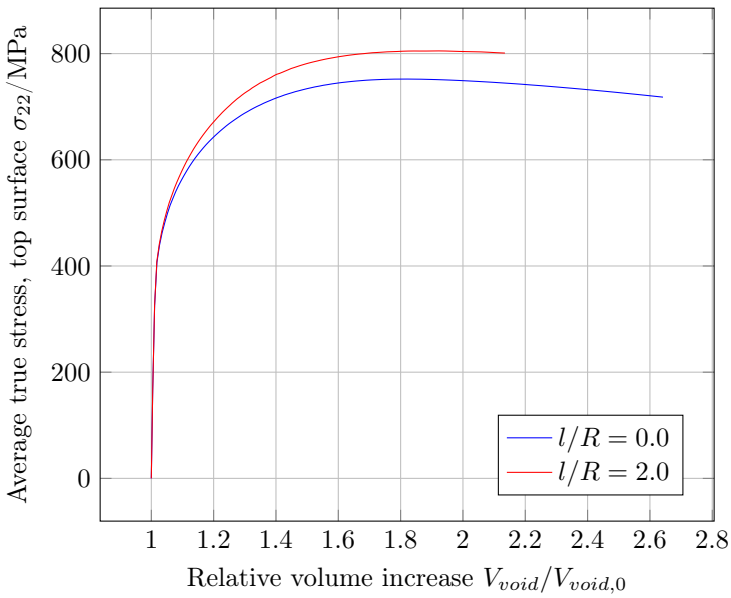

Figure 8.12: Void growth. Top surface average true strain vs. relative void volume increase.

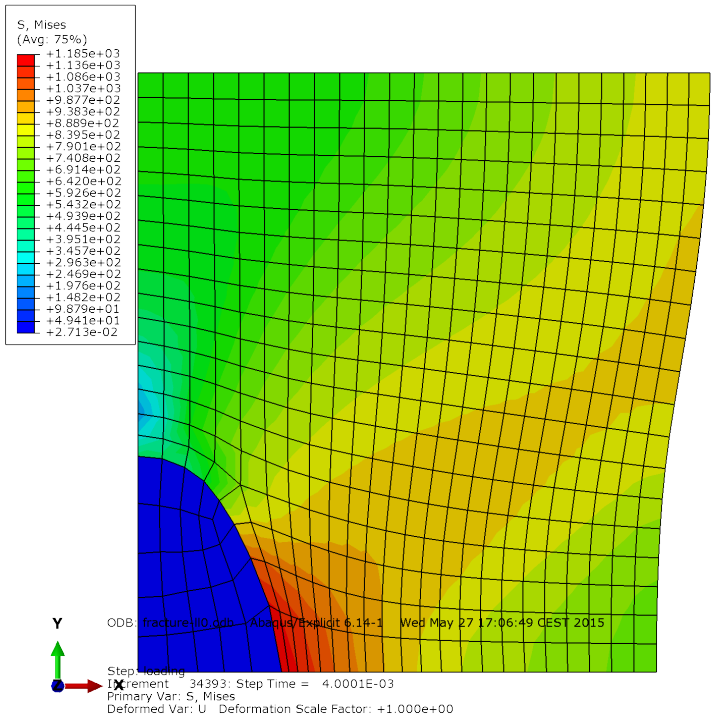

Figure 8.13: Von mises-stress distribution when $\varepsilon^l = 0.18$. $l/R = 0$.

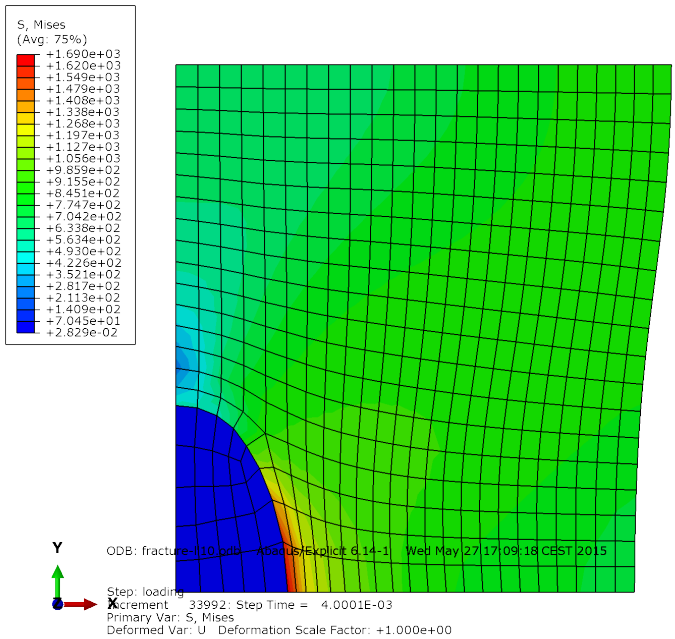

Figure 8.14: Von mises-stress distribution when $\varepsilon^l = 0.18$. $l/R = 2$.

Chapter 9

Discussion

This chapter discusses major topics of interest and relevant trends observed throughout the previous chapters, and connects them to the following appendices.

9.1 Effective plastic strain gradient measure

In this thesis, three measures of the effective plastic strain gradient have been discussed, with definitions given in Section 3.2, in summary

$$\eta^{p,A} = \sqrt{\frac{1}{4}\eta^{p,A}_{ijk}\eta^{p,A}_{ijk}} \quad \text{where} \quad \eta^{p,A}_{ijk} = \varepsilon^{p}_{ki,j} + \varepsilon^{p}_{jk,i} - \varepsilon^{p}_{ij,k},$$
$$\eta^{p,B} = \sqrt{(\boldsymbol{\varepsilon}^p \times \nabla) : (\boldsymbol{\varepsilon}^p \times \nabla)} = \|\boldsymbol{\varepsilon}^p \times \nabla\|, \quad \text{and}$$
$$\eta^{p,C} = \sqrt{\frac{\partial \varepsilon^p}{\partial x_i}\frac{\partial \varepsilon^p}{\partial x_i}} = \|\nabla \varepsilon^p\|.$$

For the problems analysed analytically and later with the finite element implementation for verification, the measures of the effective strain gradient are compared in Table 9.1.

The table shows that for the models tested, the new measure depends linearly on one of the alternative measures, $\eta^{p,C} = 2/\sqrt{3}\eta^{p,B}$, and the difference between the two previous measures $\eta^{p,A}$ and $\eta^{p,B}$ is small: their respective difference is less than 10% for all models. Problems examined in this thesis therefore do not give any evidence that the simple new measure $\eta^{p,C}$ is an over-simplification.

Table 9.1: Comparison of measures of the effective plastic strain gradient η^p

	Gravity, of unit $\left\lvert\frac{\partial \varepsilon^p}{\partial x_1}\right\rvert$	Shear, of unit $\left\lvert\frac{\partial \varepsilon^p}{\partial x_1}\right\rvert$	Bending, of unit $\left\lvert\frac{\partial \varepsilon^p}{\partial x_2}\right\rvert$
$\eta^{p,A}$	$\sqrt{5/8} \approx 0.79$	$\sqrt{3}/2 \approx 0.87$	$\sqrt{3}/2 \approx 0.87$
$\eta^{p,B}$	$\sqrt{3}/2 \approx 0.87$	$\sqrt{3}/2 \approx 0.87$	$\sqrt{3}/2 \approx 0.87$
$\eta^{p,C}$	1	1	1

Comparison of strain gradient measures has only been done for one-dimensional case. In all cases, the relative size of the plastic strain components ε^p_{ij} have been the same. For the bar in gravity, $\varepsilon^p_{22} = \varepsilon^p_{33} = -\frac{1}{2}\varepsilon^p_{11}$. Shearing of the infinite layer has only plastic shear strains $\varepsilon^p_{12} = \varepsilon^p_{21}$. In the incompressible beam in bending, for the plane strain state, $\varepsilon^p_{11} = -\varepsilon^p_{22}$. In all cases, the plastic strain decomposition is uniform, it is coordinate independent. The new, simple measure $\eta^{p,C}$ is able to represent such cases well, but will diverge from the above cases when the plastic strain components change with respect to each other, as may be the case in two- or three-dimensional models.

9.2 Strain gradient from integration points

Computing the strain gradient based on strain data from a single element requires inter-element continuous plastic strain. This requirement is not fulfilled for the vast majority of elements in finite element implementations, and is not suitable for explicit analysis. Strain gradient implementations based on element integration points when the inter-element plastic strain produces results that do not converge to the correct solution, because of under-estimation of the plastic strain gradient.

9.3 Strain gradient from nodal averaging

Calculating the plastic strain gradient based on nodal averaged values of the plastic strain has been shown to produce correct results in simple models that have previously been solved using analytical solutions, and case studies have the expected trend: given non-uniform plastic strain, decreasing the length scale increases hardening.

Nodal averaging introduces error in strain gradient computation near boundaries. Plastic strain at noes between the boundary element and inner element is approximated using plastic strains at integration points from boundary elements and inner elements. In contrast, nodes on the boundary will have contributions solely from the boundary element. This estimates the strain gradient as half the exact value for a linear strain field. Consequences of this include the jagged response on top and bottom edges of the beam discussed in Section 6.3.2.

The tower/canyon defect documented in Chapter 7 has been an issue primarily in the shear problem. This problem was proposed by Niordson and Hutchinson [18], as an argument against lower order strain gradient theories. Huang et al. [13] argue that the material model used in this thesis is not prone to the documented class of issues. Other issues with Huang et al.'s model have been found for the shear problem, documented in Appendix B.

The most unwanted property of the tower/canyon defect, is that the defect worsens as the element size decreases: it may destroy mesh convergence. Direct evidence of the tower/canyon defect is observed in the shear problem. Other models also show undesired behaviour when strain gradient effects become very large. This means that when going beyond unconditional stability, results must be checked for defects. For the simple problems analysed in this thesis, checking for defects is feasible. For large, complicated three-dimensional models, it is not.

The author has not been able to find direct evidence of the tower/canyon defect in literature. Niordson and Hutchinson [18], however, discuss the lower-order theory postulated by Bassani [2], and give general issues with with lower order strain gradient theories. Niordson and Hutchinson's implementation is explicit, forward Euler-based. The hardening formulation, however, is quite different than what is used in this thesis, and instabilities may naturally take a different form. This thesis discusses Bassani's formulation in the Section 4.2.2.

Most interesting in Niordson and Hutchinson's paper is when the defect arises. From their Figure 6, a combination of a 40×40 mesh, $l/D = 0.5$ and $\varepsilon_0^p/\varepsilon_y = 12$ gives non-monotonic decrease in regions that should be decreasing monotonically. Blatantly inserting Niordson and Bassani's yield strain $\varepsilon_y = 0.01$ and maximum strain $\varepsilon_0^p = 0.12$ into the stability criterion developed for Huang's power hardening model[1] (Equation 7.4), gives the relative critical length scale

$$\frac{l_c}{D} = 0.75,$$

[1] ε_0^p and ε_y are taken from Niordson and Hutchingson's paper. $N = 0.2$ is assumed. Further issues with Bassani's model are discussed in Subsection 4.3.2, and the author finds no reasons his model should be more stable than Huang et al.'s model.

which is not much different from $l/D = 0.5$, considering vastly different hardening formulations.

Niordson and Hutchinson found that a combination of three factors produces instability,

1. Small scale: large l/D
2. Fine element mesh: small l_e/D
3. Large deformation U: large maximum plastic strain ε_0^p.

These are the exact three conditions that have been documented in Chapter 7 to give rise to instabilities. All three contribute to the possibility of large strain gradient hardening compared to isotropic hardening. Niordson and Hutchinson analysed the same problem using higher order strain gradient plasticity [17], which did not show instabilities.

Evidence suggests that the tower/canyon defect arises only for lower-order strain gradient theories which use nodal averaging for strain gradient computation. An alternative to nodal averaging is given in Appendix A.

9.4 Strain gradient from nodal contributions

Using nodal averaging (Chapter 7) or finite differences (Appendix B) for strain gradient computation is prone to the tower/canyon defect, and unconditional stability depends on small strain gradient hardening relative to isotropic hardening. A solution to these problems is proposed in Appendix A, denoted *nodal contributions*. Preliminary studies of nodal contributions shows promise. Strain gradient computation from nodal contributions is not prone to the tower/canyon defect. Linear strain fields produces exact strain gradient computation, including near boundaries.

9.5 Limit of application for lower-order theories

The fundamental advantage of lower-order strain gradient plasticity theories is their simplicity. Only the hardening formulation has to be modified, and changes with respect to traditional non-gradient-sensitive plasticity are small. The degrees of freedom are nodal displacements, and isotropic hardening is calculated from the spacial derivatives of the displacement field. For continuous displacement fields, strains converge linearly. Traditional finite element method

gives no obvious way of calculating the strain gradient. Using integration point data is insufficient, and does not converge at all for lower-order C^0 continuous elements. The plastic strain gradient must then be calculated based on not only the local element, but also the surrounding elements.

Elastic-plastic strain decomposition is computed locally; on the basis of a single element. A given strain increment is decomposed into elastic and plastic parts so that it hits the yield surface. In this process, by the very nature of the solution, strain gradient effects from the current increment cannot be taken into effect. The traditional "solution" to this problem [18, 22] is to use the strain gradient from the previous increment. Computation of strain gradient hardening based on the previous time step is a viable option when strain gradient hardening small compared to hardening from isotropic hardening. When strain gradient hardening dominates, this attempt to hit the yield surface may miss completely, as the radius of the yield surface (in the space of principal stresses) depends strongly on the strain gradient and weakly on the plastic strain. This argument also applies to the procedure proposed in Appendix A. In other words: strain gradient hardening does not depend on a single element, but also its neighbours. It is a non-local measure. Non-local effects in the finite element method are taken into account by introducing unknowns, or as they are better known, degrees of freedom.

9.6 Higher order theories

Current lower-order strain gradient plasticity theories [18, 22] find the plastic strain gradient as a derived measure using data from previous time steps. Attempting to avoid this is difficult. The way to impose a continuous plastic strain field, is by adding the nodal plastic strain as a degree of freedom. This is how higher-order strain gradient plasticity theories are implemented in the finite element method [16, 17]. The global stiffness matrix is now sensitive to changes in plastic strain gradient, and the yield surface is hit exactly in each time step.

Appendix C illustrates that the the mathematical solution to lower-order strain gradient plasticity problems is ambiguous: several material configurations may be valid solutions to the same problem. Lower order theories produce a singular problem. In higher-order theories, additional boundary conditions make the problem non-singular.

9.7 Further work

This thesis has extensively examined computation of the plastic strain gradient based on nodal averaging of plastic strains, especially with regard to stability. The new proposed measure, nodal contributions, has not been implemented for use in finite element simulations. Several tasks and questions naturally arise.

1. A finite element implementation of strain gradient plasticity based on nodal contributions

2. Comparison of nodal averaging results and nodal contributions results under stable conditions. Is the conservative material hardening significant? Confirm that the conservativeness of nodal contributions converges with mesh size. Compare nodal contributions to nodal averaging near boundaries, such as the beam in bending, the particle and the void

3. Comparison of nodal averaging results and nodal contributions results under unstable conditions, beyond the stability limit. Does nodal contributions solve the tower/canyon defect?

4. Is a finite element strain gradient plasticity implementation based on nodal contributions prone to the issues discussed in Section 9.5? How large is then the (incremental or total) strain gradient hardening compared to isotropic hardening? Are strain increments computed approximately correctly, or do they miss the yield surface completely?

Chapter 10

Conclusions

No evidence has been found to imply that the new, simple effective plastic strain gradient measure $\eta^p = \eta^{p,C}$ is insufficient at representing strain gradient effects. Its behaviour in two and three dimensions, however has not been examined.

Strain gradient computation based on element integration points is not viable for use with the vast majority of elements, as these are in general do not predict continuous plastic strain fields.

Nodally averaging the plastic strain from surrounding element integration points is a way of enforcing a continuous strain field. Nodal strain gradient computation is shown to converge to the exact solution for simple problems. For case studies of particle strengthening and void growth, expected trends are observed: increasing strength with decreasing particle/void size. However, it may develop instability in the plastic strain field, denoted the tower/canyon defect. This instability develops for a combination of (a) large plastic strains, (b) small model length scale (equivalently, large material length scale) and (c) fine element mesh. Niordson and Hutchinson's results [18] show similar trends for a different lower-order strain gradient theory with nodal averaging. A conservative stability criterion based on the tower/canyon defect has been developed, and staying within its limits, no instabilities have been observed. Of the tested models; uniform, pure shear is most prone to development of instabilities. Nodal averaging gives wrong strain gradient estimations close to model boundaries.

An alternative to nodal averaging, denoted *nodal gradient contributions*, has been proposed. The plastic strain gradient is computed in each *node* based on surrounding element integration point strains. Elemental plastic strain gradient is then taken as the minimum possible strain gradient from interpolation of

surrounding nodal strain gradients. Nodal gradient contributions is not prone to the tower/canyon defect, and measures the plastic strain gradient exactly near boundaries for linear plastic strain fields.

When strain gradient hardening dominates equivalent plastic strain hardening, higher order strain gradient plasticity theories are necessary for reasonable strain incrementation. Increasing the plastic strain to reach the yield surface, as done in lower-order theories, when strain gradient hardening dominates, is questionable at best. In addition, the mathematical solution to the examined lower-order strain gradient theory is shown to be singular. Mathematical solution of the examined lower-order strain gradient theory partial differential equation leaves unresolved constants, which are normally determined by boundary conditions.

Appendix A

Nodal gradient contributions

This appendix gives an alternative to nodal averaging of the plastic strain field for plastic strain gradient computation. The alternative procedure has been put in an appendix to differentiate it from the thoroughly tested nodal averaging procedure.

Nodal gradient contributions is computing the gradient in nodes, and choosing elemental gradients based on quality of nodal gradients and minimum principles. This is in contrast to the conventional notion of *nodal averaging*, by which is meant lumping strain contributions to nodes, and then finding the elemental strain gradient from nodal values of the plastic strain, as explained in Section 5.3. It is shown that the suggested alternative procedure is not prone to the tower/canyon defect in one-dimensional models.

A.1 Issues with nodal averaging

Nodal averaging find nodal values of the plastic strain by means of smoothing. The nodal plastic strain is computed based on plastic strains in surrounding element integration points. In essence, nodal averaging starts out by *removing* information.

The first issue of the information removal is along the boundaries of the model. In centre nodes, contributions are made from integration points with spacial offsets in all directions, and the resulting estimate is quite accurate. On boundaries, this estimate is *bad*. Only integration points *within* the boundary are used for the lumping. For a linear strain field, this leads to an underesti-

mation the strain gradient by a factor of 0.5. When strain gradient hardening dominates, the error in hardening is vast, as encountered in the bending problem.

The second issue of the information removal is masking of jaggedness in the strain field. This leads to that towers receive no strain gradient hardening, and grow uncontrollably, as canyons receive strain gradient hardening, and are not filled. Niordson and Hutchinson [18] called for a solution to just this problem of lower order theories. The following passages from their 2003 paper on lower order plasticity theories are relevant:

> The evolution of the effective plastic strain profile is rather insensitive to mesh refinement for the conventional material with $l/D = 0$. By contrast, the peak value of effective plastic strain increases significantly upon mesh refinement when $l/D = 0.25$, and even more so when $l/D = 0.5$. Furthermore, for the most highly refined mesh for $l/D = 0.5$, it is evident that the plastic strain profile becomes increasingly non-smooth with increasing deformation. As the vertex develops, the numerical method has increasing difficulty rendering an accurate solution. If one were interested in following the development much further than that shown, a method specialized to cope with vertex-like behavior would have to be developed, but that is not our objective.

This chapter proposes a solution. It is noted that whereas Niordson and Hutchinson attributed the non-physical behaviour to the towers, this chapter counteracts the instability by removing the preconditions for canyons.

In conclusion, nodal averaging under-estimates boundary strain gradients by a factor of approximately 0.5 and may prevent plastic flow in elements that must have zero strain gradient somewhere within the element.

A.2 Nodal contributions principles

The following argument is made for a single dimension x for simplicity. A derivative $f'(x)$ of a function $f(x)$ is measured well in the middle of two known values. This fact is well known in the field of finite element analysis, and the numerical foundation of the accuracy of reduced integration. Strains are computed based on derivatives ($f'(x)$) of displacements ($f(x)$). Accurate values of displacements are found in nodes, hence good approximations of strains are

found in the middle of two nodes: in the gauss point[1]. In conclusion: for regular meshes of not-severely-distorted elements, nodes are good places to sample the strain gradient. Now, let us handle the issues postulated in the previous section.

For elements on boundaries we now have optionality. Several nodes on the element have estimated nodal values of the strain gradient, but their quality differs. Typical bad-quality nodal gradient computations are on boundaries of the model. What do these have in common? Boundary nodes base their estimations of the strain gradient on few integration point samples. The number of integration points used for the nodal strain gradient computation, denoted n_i, is taken as a quality measure of the nodal strain gradient.

Large strain gradient hardening has been shown to yield unstable results for lower-order strain gradient theories. This implies that the strain gradient should not be overestimated. A conservative measure of the strain gradient is therefore adopted. It is later shown that the conservative measure of the plastic strain gradient is not prone a range of one-dimensional defects.

A.3 Nodal contributions procedure

This section gives the nodal gradient procedure for computation of the elemental strain gradient. For simplicity, the effective plastic strain gradient measure $\eta^p = \eta^{p,C} = ||\nabla \varepsilon^p||$ is adopted.

Nodal contribution computation is the process of computing the plastic strain gradients in nodes. Nodal values of the plastic strain gradient are first computed based on surrounding integration points. A robust way of doing this is fitting a linear strain field

$$\varepsilon^p = a_0 + a_1 x_1 + a_2 x_2 + a_3 x_3 \tag{A.1}$$

to surrounding integration points using least-squares. Its gradient becomes

$$\eta^p = ||\nabla \varepsilon^p|| = \left\| a_1 \quad a_2 \quad a_3 \right\| = \sqrt{a_1^2 + a_2^2 + a_3^2}. \tag{A.2}$$

In directions s where no information is found, assume no change

$$\frac{\partial \varepsilon^p}{\partial x_s} = 0. \tag{A.3}$$

[1] For simple, constant strain elements, the gauss point used for reduced integration is in the centre of the element. Only constant strain elements are discussed here.

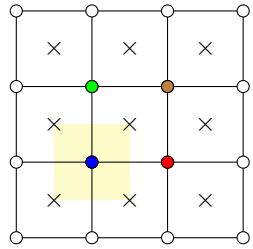

Figure A.1: Nodal gradient $\eta_i^{p,n}$ for the blue node (coordinate (1,1)) is computed on the basis of surrounding integration points (touching the yellow background). Equivalently, nodal values for the red, brown and green nodes are computed based on their neighbour elements, respectively. Integration points are crosses $\times$. Nodes are circles $\circ$.

An example of this is the bending problem. The mesh is one-dimensional in x_2. Therefore, assume $\frac{\partial \varepsilon^p}{\partial x_1} = \frac{\partial \varepsilon^p}{\partial x_3} = 0$. Where nodal gradients sample strains for a small two-dimensional problem is shown in Figure A.1.

An alternative is defining a virtual element with nodes in integration points. The plastic strain gradient can then be computed from the elemental **B**-matrix applied to plastic strain values.

Nodal gradient contribution filtering is the solution to the varying quality of the different nodal gradients. The number of integration points contributing to a nodal gradient estimation n_i is adopted as the quality measure of the nodal gradient. Then, simply base the elemental nodal gradient on high-quality nodal gradient computations. For any element, find the nodal contribution with the highest n_i, denoted n_{max}. In the elemental strain gradient computation, use only nodal contributions where $n_i = n_{max}$.

The previously examined beam in bending is a case of linear strain distribution. Its boundary behaviour is now taken as an example of nodal gradient contribution filtering. The mesh is one-dimensional. In the one-dimensional case, nodal gradient contribution filtering reduces to a simple principle: always use nodal gradient computed from two integration points. Nodes are divided into two classes. Central nodes are in contact with two elements. Boundary nodes are in contact with a single element. Thus, central nodal gradient contributions are the only contributions taken to elemental strain gradients. These represent the linear strain field exactly.

Now take a two-dimensional example. Computed values of n_i for a small

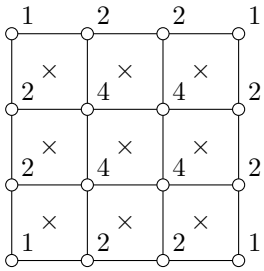

Figure A.2: Illustration of number of element integration points contributing to a nodal gradient. Integration points are crosses ×. Nodes are circles ○.

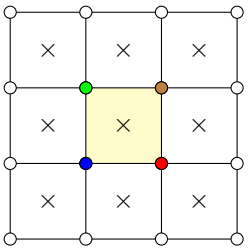

Figure A.3: Element gradient $\eta_i^{p,e}$ for the yellow (central) element in computed based on nodal contributions (blue, green, red and brown. Integration points are crosses ×. Nodes are circles ○.

2D mesh is given in Figure A.2. Figure A.3 shows that the central element will receive contributions from all surrounding nodal points, as they are all of "quality" 4. Element on boundaries will also stick to central nodal gradient values, as these are of higher quality ($4 > 2, 4 > 1$). Nodal strain gradient values sampled on the boundary are never used, and a linear strain field is represented exactly. Boundary behaviour is comparable to that of skew differences, though not of second order accuracy.

Nodal gradient contribution combination is the combination of nodal strain gradients to an elemental strain gradient. To differentiate the nodes n_1, n_2, n_3, ..., denote each nodal contribution η_i^{p,n_j}, so that j gives the node n_j and i the gradient component $\frac{\partial \varepsilon^p}{\partial x_i}$. The elemental strain gradient is $\eta_i^{p,e}$, again with i as gradient component. An intuitive procedure is to simply pick the smallest equivalent nodal strain gradient. Simply picking the lowest equivalent strain

value, however, ignores that fact that the gradient may change sign (1D) or direction (2D, 3D) inside the element, and single canyons will not be smoothed out. A different possibility, that favours accuracy over conservativeness, is taking the elemental strain gradient as the *average* nodal strain gradient. This procedure is also prone to the tower/canyon defect: towers receive no hardening, but canyons harden significantly.

A more robust procedure is given. For each possible index i of the strain gradient, collect nodal values into a vector such that

$$\mathbf{v}_i = \begin{bmatrix} v_i^{n_1} & v_i^{n_2} & v_i^{n_3} & \dots \end{bmatrix} \quad \text{where} \quad v_i^{n_j} = \eta_i^{p,n_j}. \tag{A.4}$$

Now, use the "smallest" value of the vector in the elemental strain gradient

$$\eta_i^{p,e} = \text{fieldmin}(\mathbf{v}_i), \tag{A.5}$$

where

$$\text{fieldmin}(\mathbf{v}) = \begin{cases} \min \mathbf{v} & \text{if } \forall v_i \in \mathbf{v}, v_i > 0 \\ \max \mathbf{v} & \text{if } \forall v_i \in \mathbf{v}, v_i < 0 \\ 0 & \text{otherwise.} \end{cases} \tag{A.6}$$

Or, equivalently, pick the value v_0 of smallest possible magnitude $|v_0|$ bounded by the smallest and largest elements in $\mathbf{v}$, $v_{min} \leq v_0 \leq v_{max}$.

Some example applications are

$$\begin{aligned} \text{fieldmin} \begin{bmatrix} 4 & 8 & 3 & 12 \end{bmatrix} &= 3, \\ \text{fieldmin} \begin{bmatrix} -4 & -8 & -12 \end{bmatrix} &= -4, \quad \text{and} \\ \text{fieldmin} \begin{bmatrix} 4 & 8 & 3 & -12 \end{bmatrix} &= 0. \end{aligned}$$

A reference implementation of fieldmin in the programming language Haskell is listed below.

```
fieldminR y [] = y
fieldminR y (x:xs)
  | y > 0 && x > 0 = fieldminR (min x y) xs
  | y < 0 && x < 0 = fieldminR (max x y) xs
  | otherwise      = 0

fieldmin (x:xs) = fieldminR x xs
```

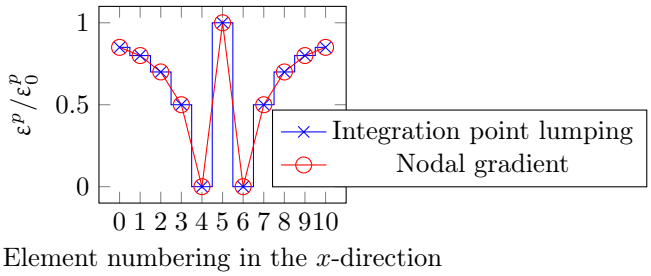

Figure A.4: Tower/canyon defect. Step 1.

A.4 Analytical verification

In this section, the procedure is verified analytically for one-dimensional strain fields. Four problems are examined. First the previously documented tower/-canyon defect. Then lone towers and lone canyons. Representation of a linear plastic strain field near boundaries is next shown to be exact, before finally, handling of a singular strain gradient is explored.

A.4.1 Tower/canyon defect

A forward Euler scheme is used: strain and strain gradient values from the previous time increment are used for the next. First, the previously encountered tower/canyon defect, illustrated in Figure A.4. Let, as in previous stability examination, pure shear cause uniform equivalent stress $\sigma_e(x) = \sigma_e$. The model is flowing plastically, such that in the absence of strain gradient effects, $\sigma_e = \sigma_{flow} = \sigma_y f(\varepsilon_0^p)$.

Element numbering is given in Figure A.4, and nodes nodes are indexed doubly: node 56 connects element 5, e_5; and element 6, e_6. Element lengths are l_e. As the model is one-directional in the x-direction, the directional index i is dropped. Relevant nodal plastic strain gradient values are $\eta^{p,56} = -\frac{\varepsilon_0^p}{l_e}$ and $\eta^{p,67} = \frac{\varepsilon_0^p}{2l_e}$.

The canyon elemental plastic strain gradient is

$$\eta^{p,6} = \text{fieldmin}\left[\eta^{p,56}, \eta^{p,67}\right] = \text{fieldmin}\left[-\frac{\varepsilon_0^p}{l_e}, \frac{\varepsilon_0^p}{2l_e}\right] = 0.$$

This causes both canyons to flow up, illustrated in Figure A.5.

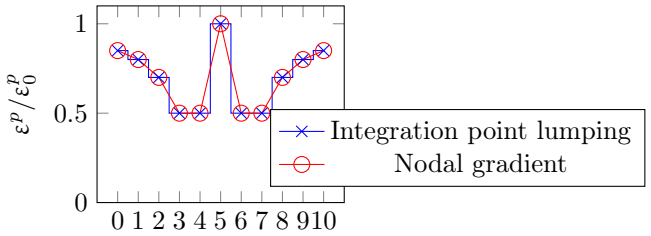

Figure A.5: Tower/canyon defect. Step 2.

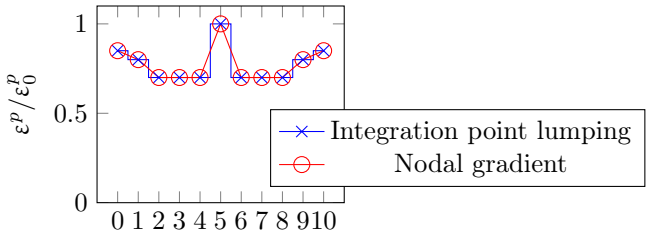

Figure A.6: Tower/canyon defect. Step 3.

Now, neither e_6 or e_7 gets gradient contributions, and flow up with their symmetric counterparts, shown in Figure A.6. This trend continues until the strain field is completely smooth.

A.4.2 Single tower

Consider a prescribed strain of a single tower with plastic strain $\varepsilon^p = \varepsilon_0^p$, and loading in pure shear as in the previous example. Prescribed strains are shown in Figure A.7. As all non-tower elements are connected to nodes with zero plastic strain gradient $\eta^{p,n} = 0$, and all will flow equally until the plastic strain distribution is uniform of $\varepsilon^p(x) = \varepsilon_0^p$.

A.4.3 Single canyon

Again, consider the previously used stress state, but the initial plastic strain distribution, as shown in Figure A.8. The tower element e_5 has nodal contri-

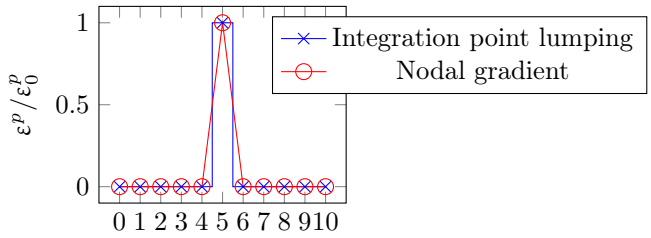

Figure A.7: Strain distribution, single tower.

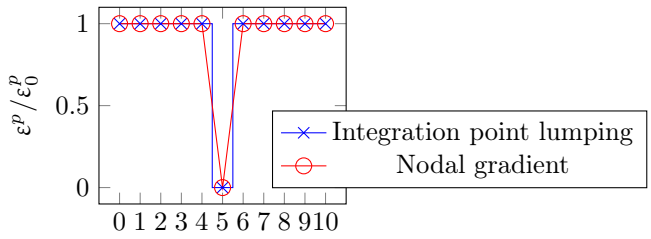

Figure A.8: Strain distribution, single canyon.

butions from nodal plastic strain gradients $\eta^{p,45} = \frac{-\varepsilon_0^p}{l_e}$ and $\eta^{p,56} = \frac{\varepsilon_0^p}{l_e}$. As the nodal contributions have different signs, the gradient must be zero somewhere in the element, which is given when inserting into the fieldmin function

$$\eta^{p,5} = \text{fieldmin}_n \left\{ \frac{-\varepsilon_0^p}{l_e}, \frac{\varepsilon_0^p}{l_e} \right\} = 0.$$

The canyon must have a zero-valued gradient somewhere between its nodes. It gets no strain gradient hardening contribution, and fills up.

A.4.4 Boundary conditions

The thin beam in bending has been shown to give a jagged response near its boundaries. For a prescribed linear plastic strain, the plastic strain gradient is constant. Computed plastic strain gradient from nodal contributions then computes the plastic strain gradient exactly, as shown in Figure A.9. Close

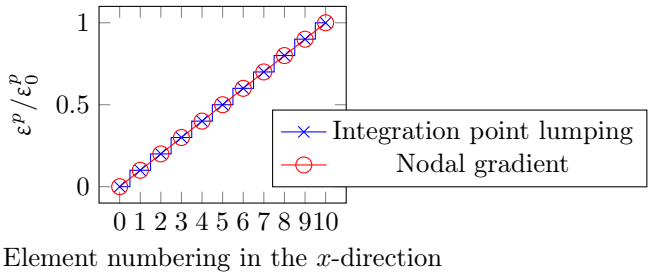

Figure A.9: Linear plastic strain distribution from prescribed curvature.

to boundaries, using nodal contributions through fieldmin, the sampled plastic strain gradient will be similar to that of skew differences: when an element is on a boundary, its nodal gradient will simply be taken from the node in contact with one or more other elements. This is better than the case for nodal averaging, where the strain gradient computation was smoothed off close to the boundary, resulting in non-physical jaggedness in the stress distribution.

A.4.5 Handling of singular strain gradients

The shear problem showcases an important issue to handle in lower-order strain gradient theories. Traditional scale-independent plasticity theories may naturally yield non-differentiable equivalent plastic strain fields $\varepsilon^p(x, y, z)$. Strain gradient computation based on nodal averaging of the equivalent plastic strain does not take this into account, and a value of the plastic strain gradient is simply picked without further consideration of smoothing effects. This issue arises in the shear example, where the plastic strain gradient is singular in the intersection between yielding and no yielding. Possible choices of tangent by nodal averaging for the element containing the singularity are shown in Figure A.10.

Nodal gradient contributions, on the other hand, by use of the fieldmin function, chooses the smallest possible value of the equivalent plastic strain, illustrated in Figure A.11. The element containing the singular plastic strain gradient is denoted the singular element. The singular element will always chose the nodal gradient contribution from its *right* node, where the strain gradient is smaller. This prevents the defect proved non-physical in Subsection 6.2.2 from arising. Whether the right node has a non-zero strain gradient contribution depends on the location of the integration point in the model.

Denote the singular element s, its neighbour n and the node separating the

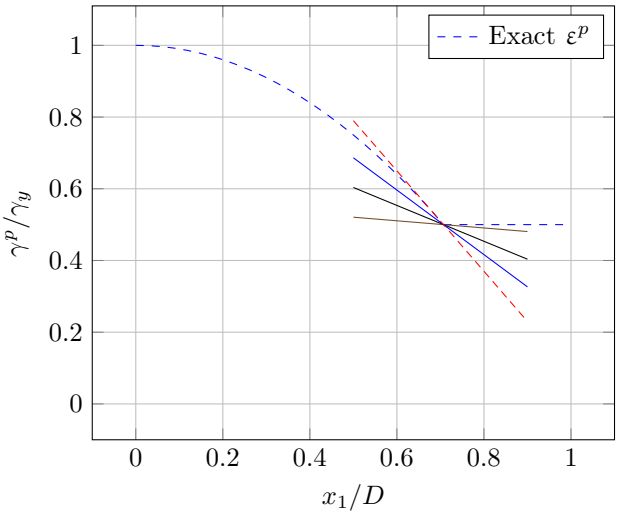

Figure A.10: Illustration of possible choices of plastic strain gradient from nodal averaging. All tangents are possible choices.

two elements sn. The problem is again one-dimensional, and we can therefore drop the directional index i. Assume that the integration point is not in yield, therefore the strain in the singular element is larger than in its neighbour

$$\varepsilon_s^p > \varepsilon_n^p$$

The singular element gradient contribution from its right node sn is its smallest strain gradient contribution, and will be chosen by the fieldmin function

$$\eta^{p,s} = \eta^{p,sn} = \frac{\varepsilon^{p,s} - \varepsilon^{p,n}}{l_e} < 0.$$

Given a non-zero strain gradient contribution from the right node, strain gradient hardening will kick in, and the element will have a lower plastic strain increment $\Delta\varepsilon^p$ than the neighbouring elements. Should the defect of Subsection 6.2.2 arise, the nodal strain gradient from its right node will switch sign

$$\eta^{p,sn} = \frac{\varepsilon^{p,s} - \varepsilon^{p,n}}{l_e} > 0$$

and by use of the fieldmin function, as nodal contributions from left and right nodes have different signs, there is no strain gradient, and the defect vanishes.

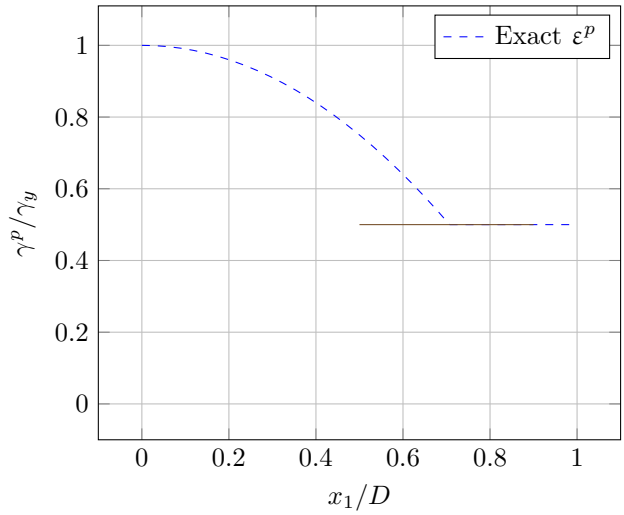

Figure A.11: Illustration of possible choices of plastic strain gradient from nodal contributions through fieldmin. Only a single tangent is a valid choice of equivalent plastic strain gradient.

A.5 On conservative strain gradient estimation

Whereas nodal contributions yield exact hardening for linear strain fields, hardening for non-linear strain fields is underestimated. When strain fields are non-linear, the strain gradient is non-uniform, and the value of the strain gradient is taken from the smallest nodal value.

Using nodal averaging, results are destabilized with decreasing mesh size. This is not the case for nodal contributions. On the other hand, the strain gradient under-estimation diminishes as the mesh size goes to 0.

This conservative approach to element hardening is not necessary when using higher-order theories, which are not prone to instabilities.

A.6 Concluding discussion

It has been observed that computing the plastic strain gradient at nodes, followed by using the minimum value of the strain gradient over elements produces stable results in one-dimensional cases where nodal averaging caused instability.

Boundaries are naturally represented correctly, and require no special care.

The measure is conservative for initially jagged strain fields that cause instabilities when using nodal averaging, and represents linear strain distributions exactly. For non-linear strain distributions, the strain gradient measure is conservative.

The strain gradient computation procedure has, however, has not been implemented, and correctness of behaviour when applied to three-dimensional problems remains to be tested.

Appendix B

Stability of analytical solutions

This appendix documents stability issues encountered using Huang et al.'s yield surface-less formulation, with the strain gradient calculated using finite differences for central points and skew differences for border points.

The purpose of this appendix is not to criticise Huang et al.'s formulation. On the contrary, it is to show that the tower/canyon defect is neither specific to the analytical solution nor the nodal average-based finite element solution.

B.1 Tower/canyon defect

Figure B.1 shows that finite differences are prone to the tower/canyon defect. Skew differences are not shown. The tower/canyon defect can emerge when canyons harden more than towers. Comparing the figure showing strain field assumed by finite differences here with the strain field assumed by nodal averaging in Figure 7.6, finite differences should be *more* prone to the tower/canyon defect than using nodal averaging.

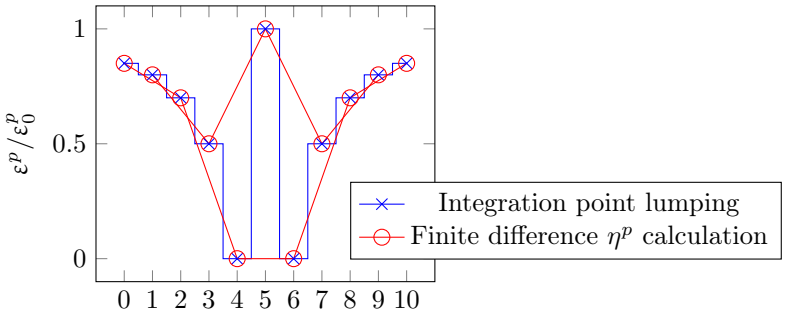

Figure B.1: Finite difference strain gradient approximation for the tower/canyon defect. Crosses are integration point data for equivalent plastic strains, circles strain distribution assumed by finite difference formulae.

B.2 Negative plastic strain increments

Attempting to reproduce the tower/canyon defect using Huang et al.'s viscoplastic-like flow formulation, another issue was encountered. Equation 3.9 repeated as

$$\dot{\varepsilon}^p = \dot{\varepsilon}\left(\frac{\sigma_e}{\sigma_{flow}}\right)^m$$

with equivalent plastic strain isolated as

$$\dot{\varepsilon}^p = \frac{\left(\frac{\sigma_e}{\sigma_{flow}}\right)^m}{1-\left(\frac{\sigma_e}{\sigma_{flow}}\right)^m}\dot{\varepsilon}^e.$$

In contrast to conventional plasticity, strain gradient plasticity allows the material capacity to decrease, $\dot{\sigma}_{flow} < 0$, as $\dot{\sigma}_{flow} = \frac{\partial \sigma_{flow}}{\partial \varepsilon^p}\dot{\varepsilon}^p + \frac{\partial \sigma_{flow}}{\partial \eta^p}\dot{\eta}^p$, and $\dot{\eta}^p$ can be negative. If the capacity drops such that $\sigma_e < \sigma_{flow}$, the plastic strain increment becomes negative $\dot{\varepsilon}^p < 0$, and results are useless. Figure B.2 shows results where the strain increments have turned negative. The issue of negative plastic flow is counteracted by using the suggested non-negative flow rule of Equation 3.11, repeated

$$\dot{\varepsilon}^p = \dot{\varepsilon}^e\left(\frac{\sigma_e}{\sigma_{flow}}\right)^m.$$

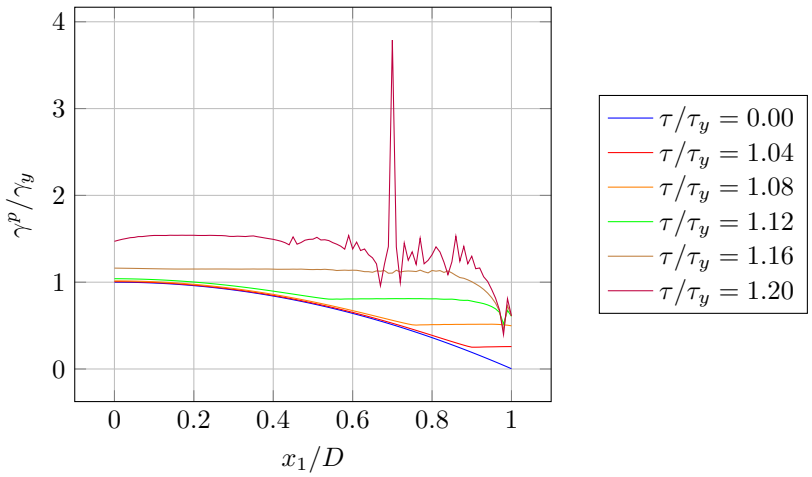

Figure B.2: Distribution of normalized engineering plastic shear strain for $l/D = 10$. Negative equivalent plastic strain increments $\Delta\varepsilon^p < 0$ arise.

B.3 Evidence of instabilities

The analytical solution to the shearing of the infinite layer was found using explicit stress incrementation. The layer was discretized into 100 elements ($\Delta x = 0.01D$), and loading incremented in 2400 increments ($\Delta\tau = 0.0005\tau_y$, $\tau \leq 1.2\tau_y$). Increasing the relative material length scale from $l/D = 3$ to $l/D = 10$ produces unstable results presented in Figure B.2.

Imposing the positive plastic strain rate (Equation 3.11), the equivalent plastic strain distribution $\varepsilon^p(x)$ is smooth, shown in Figure B.3. For the lower curves, strain gradient effects come into play. Further cranking up the strain gradient effect, ($l/D = 100$, Figure B.4), a vertex arises in the symmetry plane, before jaggedness takes over.

Increasing l further produces different effects similar to the ones discussed in Appendix C. The tower/canyon defect is instead imposed by decreasing the element length $l_e = \Delta x = dx = 0.004$. Decreasing the element length requires decreasing of the stress increment $\Delta\tau = 0.0001\tau_y$, as the solution procedure is explicit. Large strains also contribute to the tower/canyon defect, and larger stresses are used ($\tau < 2.4\tau_y$). The result is shown in Figure B.5.

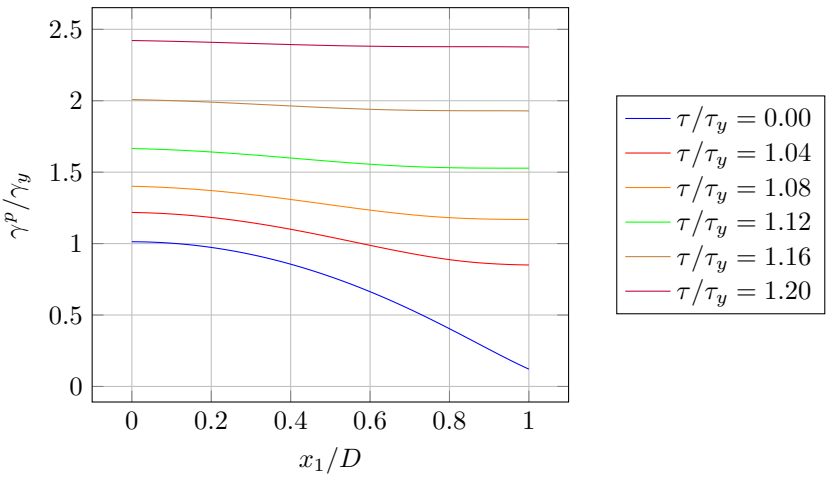

Figure B.3: Distribution of normalized engineering plastic shear strain for $l/D = 10$. Equivalent plastic strain is positive.

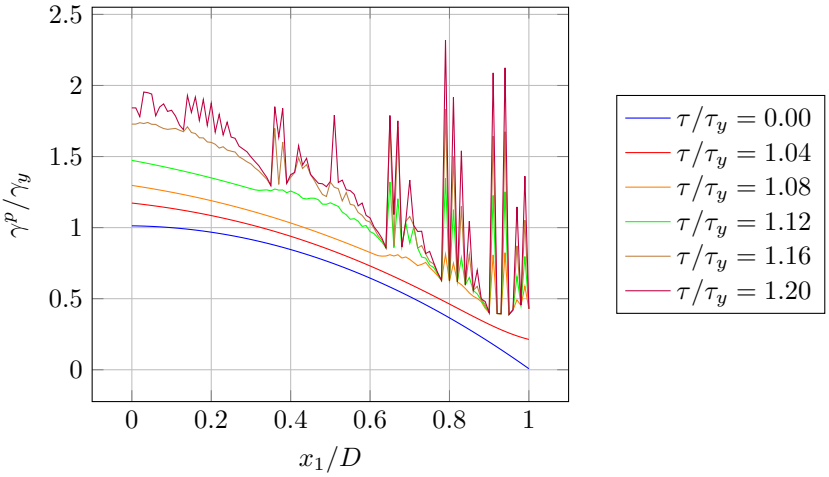

Figure B.4: Distribution of normalized engineering plastic shear strain for $l/D = 100$. Equivalent plastic strain is positive.

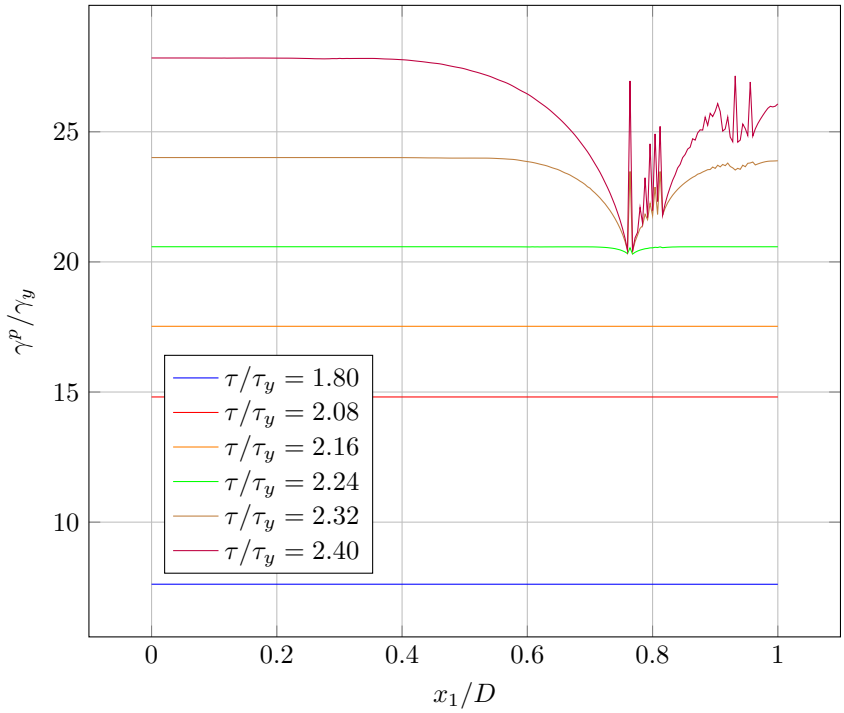

Figure B.5: Distribution of normalized engineering plastic shear strain for $l/D = 10$. Tower/canyon defect observed.

Appendix C

Ambiguity of lower-order theories

This appendix documents a concrete difference between lower-order and higher order plasticity theories: the ambiguity of solutions to lower-order plasticity problems. Niordson and Hutchinson [18] pointed out both specific problems (vertices and instability) and a rather vague, more general criticism on the nature of lower-order plasticity theory formulations. This appendix aims to separate the general criticism from implementation-specific details, such as questionable hardening formulation (see Section 4.2.2) and jagged strain solution (analogous to the tower/canyon defect).

C.1 Introduction

Most space in Niordson and Hutchinson's paper [18] is allocated to numerical study. They conclude, however, on a more general note, and the following passages are highly relevant for this chapter (numbering added).

> (1) Although the two problems investigated here are fairly simple, it is unlikely that they are exceptional as far as the behavior they reveal. The unusual behavior is a consequence of the mathematical formulation of the lower order gradient theories. [...] (2) However, the strain gradients introduced into the tangent moduli result in terms in the total (or integrated) quantities appearing in these

> equations are more more highly differentiated than any that appear in conventional theory.

Niordson and Hutchinson first (1) comment on the general nature of lower-order strain gradient theories. In essence, exact solutions to lower-order strain gradient plasticity can differ from exact solutions to higher-order plasticity problems. The difference, will be shown to lie in boundary conditions—ironically brought forward as an advantage of lower-order theories.

They then (2) attribute the unusual behaviour to what in this thesis was denoted path dependence in the space of the equivalent plastic strain ε^p and the effective plastic strain gradient η^p (or α, as in the lower-order formulation discussed by Niordson and Hutchinson). The underlying issue of lower-order theories was left untouched.

The fundamental problem of lower-order strain gradient theories is that they may be ambiguous in the exact, mathematical solution to a problem[1]. In case of ambiguity, which solution is chosen depends on how the load is applied. For the problem of the sheared infinite bar, the expected solution is that the equivalent plastic strain distribution evens out as stresses increase. It will be shown that it is not guaranteed that the equivalent plastic strain distribution smooths out, and that other configurations satisfy the lower-order theory material equations.

C.2 Ambiguity of lower-order theories

The shear model has two valuable properties that make theoretical analysis feasible:

1. Only non-zero shear strains $\varepsilon_{12} = \varepsilon_{21}$
2. Constant flow stress σ_{flow}.

Only shear strains present implies zero volumetric change, and the geometry is linear. The constant flow stress makes analytical solution possible. The hardening formulation is repeated from Equation 3.5,

$$\sigma_{flow} = \sigma_y \sqrt{f(\varepsilon^p)^2 + l\eta^p} \quad \text{where} \quad f(\varepsilon^p) = \left(1 + \frac{E\varepsilon^p}{\sigma_y}\right)^N .$$

[1] This appendix illustrates that ambiguity arises in formulations similar to that proposed by Huang et al. General proof that this problem applies to all lower-order theories is not given, but no reason that this is not the case is neither found. It is proposed that lower-order theories must be treated critically unless there is proper ground to believe that they are not prone to ambiguous solutions.

Using the simple effective strain gradient measure $\eta^p = \eta^{p,C}$, hardening exponent $N = 0.5$ and assuming non-negative plastic strain derivative $\frac{\mathrm{d}\varepsilon^p}{\mathrm{d}x} \geq 0$, this simplifies to

$$1 + \frac{\varepsilon^p}{\varepsilon_y} + l\frac{\mathrm{d}\varepsilon^p}{\mathrm{d}x} = \left(\frac{\sigma_{flow}}{\sigma_y}\right)^2,$$

after some reordering,

$$\frac{\mathrm{d}\varepsilon^p}{\mathrm{d}x} + \frac{1}{l\varepsilon_y}\varepsilon^p = \frac{1}{l}\left[\left(\frac{\sigma_{flow}}{\sigma_y}\right)^2 - 1,\right]$$

and a differential equation solvable through use of integrating factor emerges

$$\frac{\mathrm{d}y(x)}{\mathrm{d}x} + py(x) = q,$$

where $y(x) = \varepsilon^p(x)$, $p = \frac{1}{l\varepsilon_y}$ and $q = [(\sigma_{flow}/\sigma_y)^2 - 1]/l$. The integrating factor when p is constant is

$$v(x) = \int p(x)\,\mathrm{d}x = px$$

giving the solution

$$\begin{aligned} y(x) &= e^{-v(x)} \int e^{v(x)} q(x) \\ &= e^{-px}\left(\frac{q}{p}e^{px} + C\right) \quad \text{where } C \text{ is a constant.} \end{aligned}$$

Back-substitute the original variables to obtain the solution

$$\varepsilon^p(x) = \varepsilon_y\left[\left(\frac{\sigma_{flow}}{\sigma_y}\right)^2 - 1\right] + Ce^{-x/(l\varepsilon_y)}.$$

What is the value of the constant? Lower-order theory gives no direction on what to pick. In mathematics, the constants in differential equations are defined through boundary conditions. Higher order theory provides these. Lower-order theory does not.

To get rid of absolute values, the strain derivative was assumed non-negative $\frac{\mathrm{d}\varepsilon^p}{\mathrm{d}x} \leq 0$. This restricts the constant to non-positive values $C \leq 0$. The right side of a tower/canyon defect is a concrete visualization of this shape, if $N = 0.5$. Assuming $\frac{\mathrm{d}\varepsilon^p}{\mathrm{d}x} \leq 0$ yields the strain field left of a tower/canyon defect.

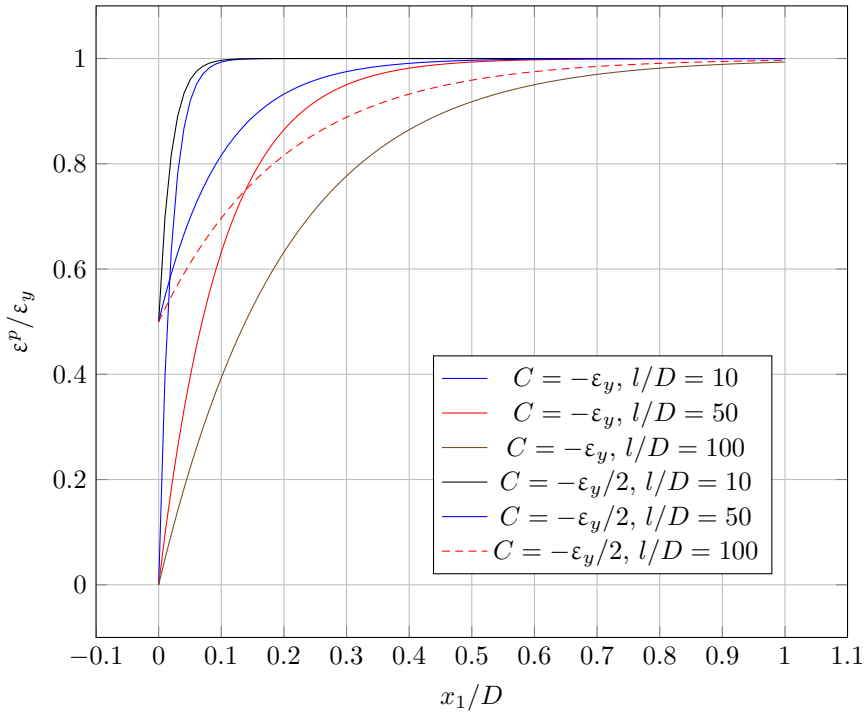

Figure C.1: Mathematical solutions to shear problem, given $\sigma_{flow}/\sigma_y = 2$ and $N = 0.5$.

Different curves predicted by the mathematical solution to the shear problem are plotted in Figure C.1. Increasing the material length scale increases the strain gradient contribution to hardening. Thus, for equilibrium to be obtained, larger l allows the gradient $\frac{\mathrm{d}\varepsilon^p}{\mathrm{d}x}$ to be lower for the same total hardening.

The correct, absolute-value sensitive solution resembles a superpositioning of two solutions of the differential equation, where the strain derivative $\frac{\mathrm{d}\varepsilon^p}{\mathrm{d}x}$ is assumed to be positive and negative, respectively. This yields a solution sensitive to prescribed strain on both boundaries, and the plastic strain field is

$$\varepsilon^p(x) = \varepsilon_y \left[\left(\frac{\sigma_{flow}}{\sigma_y} \right)^2 - 1 \right] + C_1 e^{-x/(l\varepsilon_y)} + C_2 e^{-(1-x)/(l\varepsilon_y)}.$$

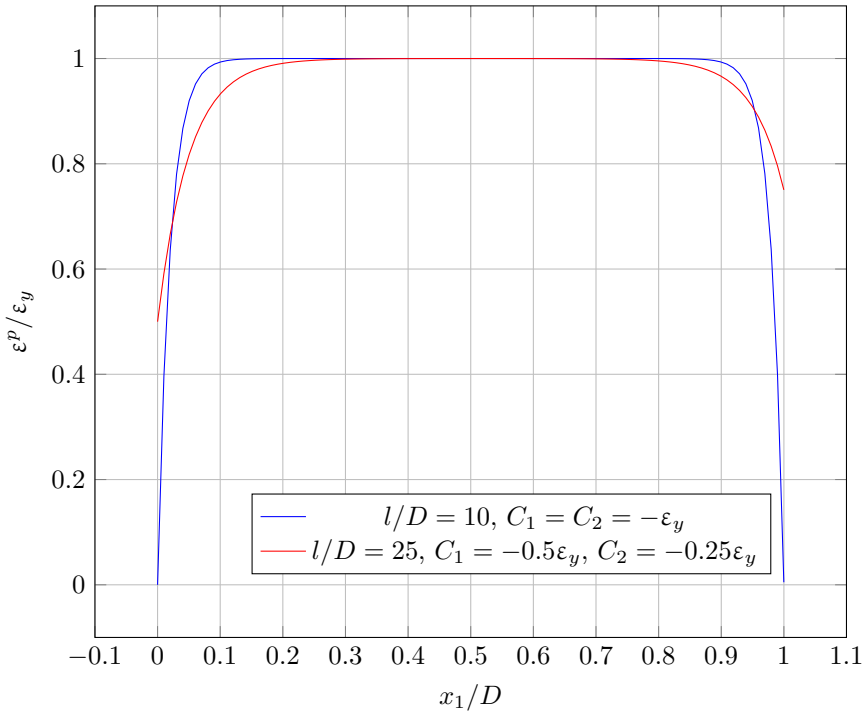

Figure C.2: Mathematical solutions to shear problem, given $\sigma_{flow}/\sigma_y = 2$ and $N = 0.5$. Superposition of sensitivity to positive and negative plastic strain derivatives.

Superpositioning of solutions is reasonable as strains are near-constant in the centre region. For larger material length scales, if the two not-near-constant curves meet, the above solution is invalid and individual cannot be combined.

Both constants must be non-positive to satisfy initial assumptions, $C_1 \leq 0$ and $C_2 \leq 0$. Again, the first term that depends on the flow stress gives the response without strain gradient effects. The second term controls the plastic strain on the left boundary, $\varepsilon_y - \varepsilon^p(x/D = 0) = -C_1$, and the third term the right boundary $\varepsilon_y - \varepsilon^p(x/D = 1) = -C_2$. Figure C.2 plots this solution for different values of C_1, C_2 and l. $C_1 = C_2 = -\varepsilon_y$ is equivalent to the prescribed boundary conditions $\varepsilon^p(0) = \varepsilon^p(D) = 0$, which may be obtained by prescribing boundary conditions in higher-order theories, as done by Niordson and Hutchinson [17].

C.3 Boundary conditions

In conclusion, lower-order theories do not have a one-to-one correspondence between problems and solutions. An analogy to traditional finite element method is useful for illustration. Traditional finite element bases material response on strains. For a well-defined response, strains must be derived from a continuous field (displacements). On boundaries, displacements or stresses must be prescribed. Strain gradient plasticity theories derive material response from strains and the strain gradient. A one-to-one correspondence between problem and solution therefore requires calculating the strain gradient from a continuous field (strains). On boundaries, strains or the quantity work-conjugate to strain gradients must be defined. Higher-order strain gradient theories denote the quantity work-conjugate to strain gradients higher-order stresses.

A final question arises. How does lower-order strain gradient plasticity theories handle this ambiguity? Nodal averaging under-estimates the strain gradient over boundaries and is biased towards $\frac{\mathrm{d}\varepsilon^p}{\mathrm{d}n} = 0$, where n is the direction normal to the boundary. For cases of linear strain, this produces undesired behaviour. Nodal contributions and finite differences take the gradient from the one computed based on the two closest integration points. This is a much more accurate estimation of the strain gradient, but still not exact. Efforts have been made to reproduce responses where $C_1 \neq 0$ or $C_2 \neq 0$ in the analytical shear example, where finite- and skew differences are used. Different initial strain fields $\varepsilon^p(x)|_{t=0}$ and different length scales l/D where attempted. Figure C.3 shows results where non-zero strain gradient over boundaries were encountered. The slope is significantly less steep because of different values of N. In exact, mathematical solutions (figures C.1 and C.2), $N = 0.5$. In iterated, Forward Euler-based solutions (Figure C.3), $N = 0.2$. When N is large, plastic strain hardening is large. Lower values of N give larger relative strain gradient hardening, and a less steep curve still gives a large contribution to total hardening. Out of 109 total runs actively prescribing initial strains attempting to produce non-zero boundary strain gradients, 8 showed trends similar to Figure C.3. The rest produced uniform plastic strains.

Why were solutions with non-zero strain gradient over boundaries hard to produce?

1. The solution procedure is iterative
2. Finite differences underestimates exponential functions

First, an exponential strain field similar to those of Figure C.1 was prescribed. The iterative solution procedure for each step calculates the strain gradient

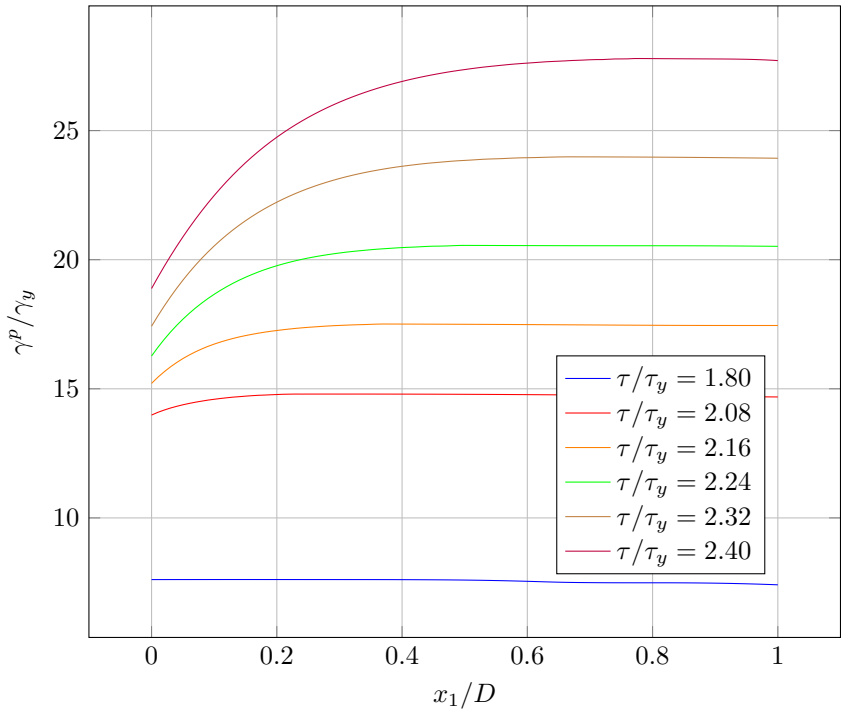

Figure C.3: Distribution of normalized engineering plastic shear strain for $l/D = 10$, $N = 0.2$. Rare occurrence of non-zero boundary strain gradient.

based on two points (finite difference) or three points (skew difference). Take the end point with lower equivalent plastic strain. If the strain distribution had been quadratic, the strain gradient would have been estimated exactly. Fitting three points from an exponential curve to a parabola, however, underestimates the derivative at the edge. Underestimation of the strain gradient underestimates total hardening, and flow follows.

The possibility of multiple solutions to lower-order strain gradient plasticity problems is not unique to Huang et al.'s theory. Volokh and Hutchinson [23] previously showed the same ambiguity for Bassani's lower order theory [2].

Bibliography

[1] M. F. Ashby. The deformation of plastically non-homogeneous materials. *Philosophical Magazine*, 21(170):399–424, 1970.

[2] J.L. Bassani. Incompatibility and a simple gradient theory of plasticity. *Journal of the Mechanics and Physics of Solids*, 49(9):1983–1996, 2001.

[3] Kolbein Bell. *An engineering approach to finite element analysis of linear structural mechanics problems*. Akademika Publishing, 2013.

[4] J.F.W. Bishop and R. Hill. A theory of the plastic distortion of a polycrystalline aggregate under combined stresses. *The London, Edinburgh, and Dublin Philosophical Magazine and Journal of Science*, 42(327):414–427, 1951.

[5] P. Cermelli and M.E. Gurtin. On the characterization of geometrically necessary dislocations in finite plasticity. *Journal of the Mechanics and Physics of Solids*, 49(7):1539–1568, 2001.

[6] Robert D. Cook, David S. Malkus, Michael E. Plesha, and Robert J. Witt. *Concepts and Applications of Finite Element Analysis*. John Wiley & Sons, 2007.

[7] Thomas H. Cormen, Clifford Stein, Ronald L. Rivest, and Charles E. Leiserson. *Introduction to Algorithms*. McGraw-Hill Higher Education, 2nd edition, 2001.

[8] N. A. Fleck and J. W. Hutchinson. *Strain Gradient Plasticity*, volume 33 of *Advances in Applied Mechanics*. 1997.

[9] N. A. Fleck, G. M. Muller, M. F. Ashby, and J. W. Hutchinson. Strain gradient plasticity: Theory and experiment. *Acta Metallurgica Et Materialia*, 42(2):475–487, 1994.

[10] Dominique François, André Pineau, and André Zaoui. *Mechanical Behavior of Materials. Volume 1: Micro- and Macroscopic Constitutive Behaviour*. Springer, 2012.

[11] O. S. Hopperstad, T. Børvik, T. Berstad, A. H. Clausen, and A. Benallal. A hypoelastic-viscoplastic constitutive model in LS-DYNA for dynamic strain aging—the McCormick model. 1992.

[12] Odd Sture Hopperstad and Tore Børvik. *Lecture notes. Material Mechanics*, volume 1. 2013.

[13] Y. Huang, S. Qu, K. C. Hwang, M. Li, and H. Gao. A conventional theory of mechanism-based strain gradient plasticity. *International Journal of Plasticity*, 2004.

[14] Derek Hull and D. J. Bacon. *Introduction to Dislocation, Fifth Edition*. Butterworth-Heinemann, 2011.

[15] U.F. Kocks. The relation between polycrystal deformation and single-crystal deformation. *Metallurgical and Materials Transactions*, 1(5):1121–1143, 1970.

[16] Lars Pilgaard Mikkelsen. Implementing a gradient dependent plasticity model in ABAQUS. 2007.

[17] C.F. Niordson and J.W. Hutchinson. Non-uniform plastic deformation of micron scale objects. *International Journal for Numerical Methods in Engineering*, 56(7):961–975, 2003.

[18] C.F. Niordson and J.W. Hutchinson. On lower order strain gradient plasticity theories. *European Journal of Mechanics, A/Solids*, 22(6):771–778, 2003.

[19] J.F. Nye. Some geometrical relations in dislocated crystals. *Acta Metallurgica*, 1(2):153–162, 1953.

[20] P. Steinmann. Views on multiplicative elastoplasticity and the continuum theory of dislocations. *International Journal of Engineering Science*, 34(15):1717–1735, 1996.

[21] J.S. Stölken and A.G. Evans. A microbend test method for measuring the plasticity length scale. *Acta Materialia*, 46(14):5109–5115, 1998.

[22] Y.S. Suh, S. Song, and M.S. Park. Length-scale-dependent strengthening of particle-reinforced metal matrix composites with strain gradient plasticity. *Journal of Mechanical Science and Technology*, 27(4):1071–1079, 2013.

[23] K. Y. Volokh and J. W. Hutchinson. Are lower order gradient theories of plasticity really lower order? *J. Appl. Mech*, 56:862–975, 2002.